The Geological Society of America
Special Paper 507
2014

Tectonics and topographic evolution of Namche Barwa and the easternmost Lhasa block, Tibet

Peter K. Zeitler
Anne S. Meltzer
Lucy Brown
Department of Earth and Environmental Sciences, Lehigh University, Bethlehem, Pennsylvania 18015, USA

William S.F. Kidd
Chul Lim*
Department of Earth and Atmospheric Sciences†, University at Albany, Albany, New York 12222, USA

Eva Enkelmann
Department of Geology, University of Cincinnati, Cincinnati, Ohio 45221, USA

ABSTRACT

In the easternmost Himalaya and southeastern Tibet, the Namche Barwa–Gyala Peri massif and adjacent Lhasa block host some of the Earth's most active geologic processes and extreme topography. Synthesis of U-Th/He and Ar-Ar thermochronology, anatectic history, seismicity, and structural geology shows the important role that surface processes have played in this region in both local and orogen-scale crustal dynamics. Basement rocks of the massif underwent an episode of metamorphism, partial melting, and focused deformation that began ca. 10 Ma and likely remains active due to thermally mediated feedbacks between these processes and erosion. Strong differential rock uplift at Namche Barwa established the immense Namche Barwa knickzone on the Yarlung Tsangpo River, which has been stabilized through coupling between erosion driven by high stream power and localized deformation. This knickzone has maintained a high secondary base level of ~3000 m for the upper Yarlung Tsangpo watershed and so has shielded a large region of southeastern Tibet from excavation by the river, which in turn could alter the morphology and so the dynamics of the eastern Himalayan orogenic wedge. The landscape evolution of the southeast Lhasa block involved slow regional unroofing or incision in the Neogene, a significant pulse of ~5 km of rapid exhumation from ca. 10 to 5 Ma, and since then a great reduction in exhumation started once the Namche Barwa knickzone on the Yarlung Tsangpo was established. The low-relief high-elevation surface in the area is a relatively young feature, developed after the rapid 10–5 Ma exhumation pulse.

*Current affiliation: School of Earth and Environmental Sciences, Seoul National University, Seoul, South Korea.
†Now the Department of Atmospheric and Environmental Sciences

Zeitler, P.K., Meltzer, A.S., Brown, L., Kidd, W.S.F., Lim, C., and Enkelmann, E., 2014, Tectonics and topographic evolution of Namche Barwa and the easternmost Lhasa block, Tibet, *in* Nie, J., Horton, B.K., and Hoke, G.D., eds., Toward an Improved Understanding of Uplift Mechanisms and the Elevation History of the Tibetan Plateau: Geological Society of America Special Paper 507, p. 23–58, doi:10.1130/2014.2507(02).

INTRODUCTION: DYNAMICS NEAR AN INDENTOR CORNER

Large topographic gradients and relief influence the strain, thermal state, and petrologic evolution of the lithosphere in active orogens, and the development of feedbacks between surface and solid Earth processes is inevitable (Avouac and Burov, 1996; Beaumont et al., 2001; Koons et al., 2002). Southeastern Tibet (Fig. 1) is an excellent location to study such feedbacks because it hosts a dramatic transition in hypsometry. Here the relatively low relief topography commonly associated with the high plateau of Tibet gives way to the rugged, deep canyons of the Three Rivers region and the extreme relief associated with the Yarlung Tsangpo River as it exits the plateau through its Big Bend gorge (Fig. 2). This morphological transition parallels a geodynamic transition from the relatively stable plateau to the complex tectonics of the lithospheric indentor corner, which manifests itself, at least in the crust, as the eastern Himalayan syntaxis (Koons, 1995; Koons et al., 2013; Sol et al., 2007; Li et al., 2008). Regionally, deep incision of the eastern plateau margin is underway, leading to significant shortcuts of the mass flux through the orogen (Hallet and Molnar, 2001). More locally, the Namche Barwa massif is a locus of rapid rock uplift (Burg et al., 1997) that may in part owe its origin to focused erosion by the Yarlung Tsangpo (Zeitler et al., 2001a; Finnegan et al., 2008). It has been proposed this small local feature (~60 × 60 km) has outsized geodynamic impact because it stabilized the river's large knickpoint, preventing incision along the Yarlung Tsangpo gorge from propagating upstream and dissecting the rear of the eastern Himalaya and the southeastern Tibetan Plateau (Zeitler et al., 2001a). Dramatic landscape dynamics may also have been involved; some have speculated that capture of an ancestral Yarlung Tsangpo by the Brahmaputra system is an expected consequence of the geodynamics of the eastern syntaxis (e.g., Seeber and Gornitz, 1983; Koons, 1995; Brookfield, 1998) that may have happened recently (Clark et al., 2004; He and Chen, 2006).

While southeastern Tibet is interesting given the large magnitude and high rate of the processes operating there, the region offers the opportunity to address broader questions about length scales and feedbacks in orogeny and the orogenic record. These questions center on such issues as the role of surface processes in geodynamics, the origin and pace of sediment sourcing for the foreland, the broader applicability of the tectonic-aneurysm model (Zeitler et al., 2001a, 2001b; Koons et al., 2013), the preservability and net impact in the geologic record of synorogenic feedbacks between the surface and solid Earth, and the potential in

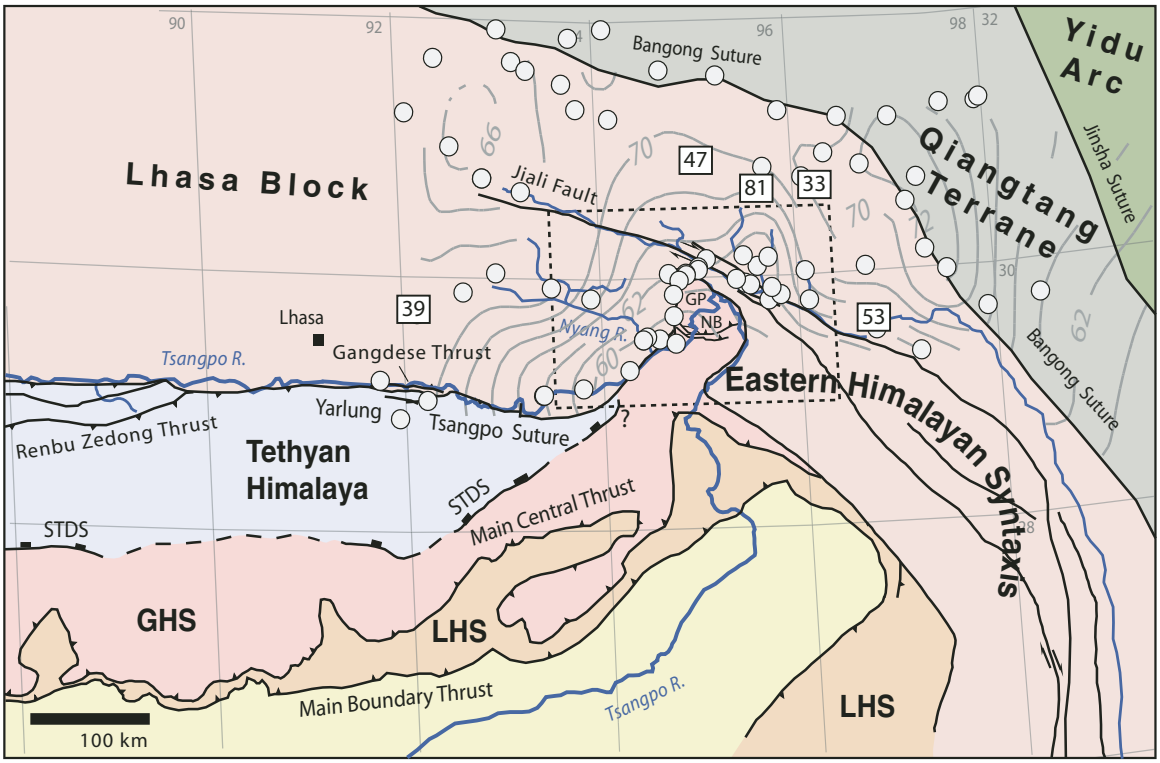

Figure 1. General location map modified from Pan et al. (2004) and Yin and Harrison (2000), showing main tectonic elements and geography of southeastern Tibet. GHS—Greater Himalayan Sequence; LHS—Lesser Himalayan Sequence; STDS—South Tibetan detachment system. Circles show locations of stations in seismic array discussed in text. White boxes with numbers are zircon U-Th/He ages not shown in Figure 15. Dashed box shows the location of Figures 2, 10, and 15. GP and NB—locations of Gyala Peri and Namche Barwa peaks. Gray contours show depth to Moho below sea level (contour interval 2 km) (after Zurek, 2008).

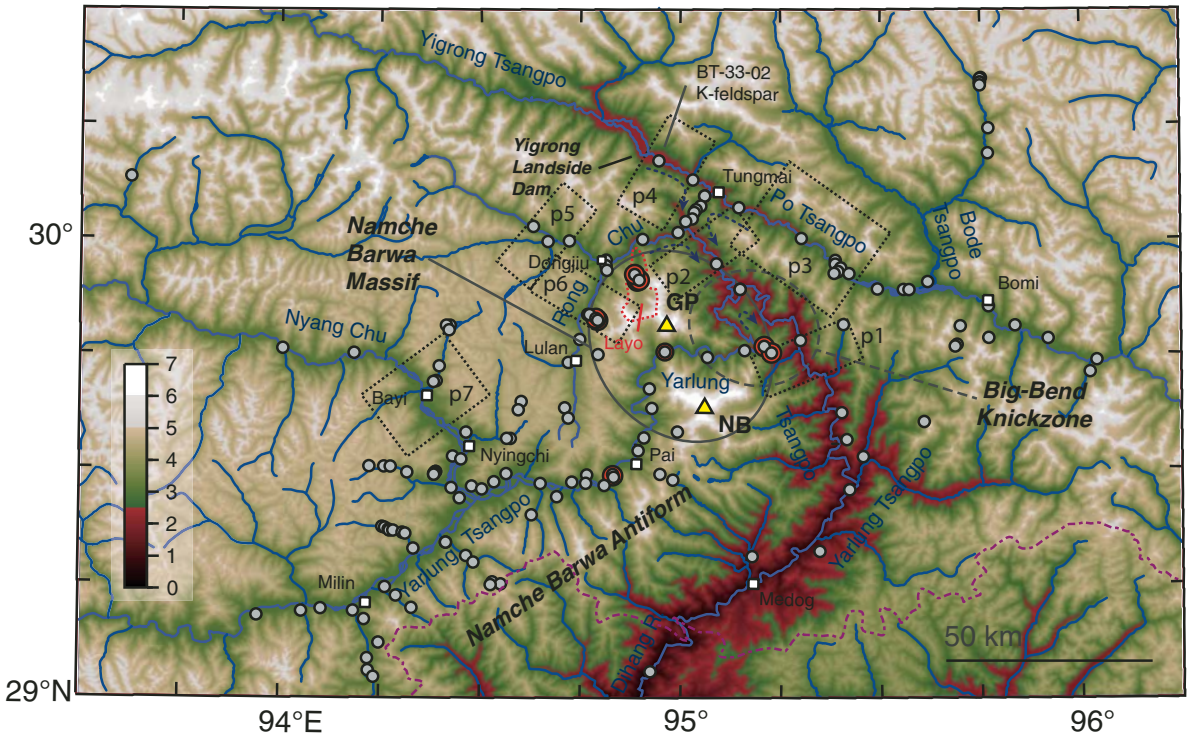

Figure 2. Digital elevation model showing general topography of the southeastern Lhasa block and its complex, convergent drainage pattern into the Big Bend knickzone. Some elements discussed in the text are also shown. Dashed boxes show approximate locations of topographic swath profiles displayed in Figure 20. GP and NB—Gyala Peri and Namche Barwa peaks. Gray dots show locations and distribution of cooling-age samples discussed in text; orange dots show locations of samples used for U-Pb dating. Dashed purple line is international border between China and India.

such active regions for hazards such as outburst flooding, landslides, and earthquakes.

Here we report and synthesize observations from thermochronology, geochronology, seismicity, and structural geology that bear on the Neogene and Quaternary tectonics and topographic evolution of the easternmost Himalaya in southeastern Tibet. These data were collected as part of a larger multidisciplinary project (Geodynamics of Indentor Corners) that in collaboration with the Chengdu Institute of Geology and Mineral Resources (Chengdu, China) examined the origin and dynamics of a broader region of southeastern Tibet, and included studies of surface processes (Finnegan et al., 2008; Montgomery et al., 2004; Korup and Montgomery, 2008), petrology and metamorphic geochronology (Booth et al., 2004, 2009), seismology and geodetics (Sol et al., 2007; Zurek, 2008), geodynamics (Koons et al., 2002, 2013), and detrital thermochronology (Stewart et al., 2008; Enkelmann et al., 2011).

GEOLOGICAL CONTEXT AND PREVIOUS WORK

Geography and Nomenclature

Given the amount of work that has been done in southeasternmost Tibet and the complicated linguistic and cultural history of the region, a variety of names for features and localities can be found in the literature. In the interests of clarity we define a number of the informal terms we use in this paper. By southeastern Tibet we mean that portion of the Yarlung Tsangpo watershed located east of Lhasa and south of the Bangong suture, and by southeastern Lhasa block we mean rocks of that terrane located between Lhasa and Bomi (Figs. 1 and 2). For the segment of the easternmost Himalaya that terminates within the eastern syntaxis, we differentiate between the Namche Barwa antiform to the southwest and its along-strike, geologically more active continuation to the northeast of the Nam-la thrust, which we refer to as the Namche Barwa massif (Figs. 2 and 3). This massif encompasses the peaks Gyala Peri and Namche Barwa as well as the large Big Bend knickzone on the Yarlung Tsangpo (Fig. 2). The antiform has sometimes been referred to as the Namche Barwa syntaxis, but we believe that it is more appropriate to apply this term to the much larger, ~500-km-scale Eastern Himalayan syntaxis that frames the eastern margin of the Himalayan-Tibetan orogeny (Fig. 1). Generally we use river names that have been used recently, but following the early usage by Kingdon-Ward (1926), we use “Po Tsangpo” for the entire stretch of the river that extends from east of Bomi to Tungmai in the west, and then past Parlung to its confluence with the Yarlung Tsangpo within the Namche Barwa massif (see also Cox, 2001). Note that a number of papers refer to the Bomi-Tungmai

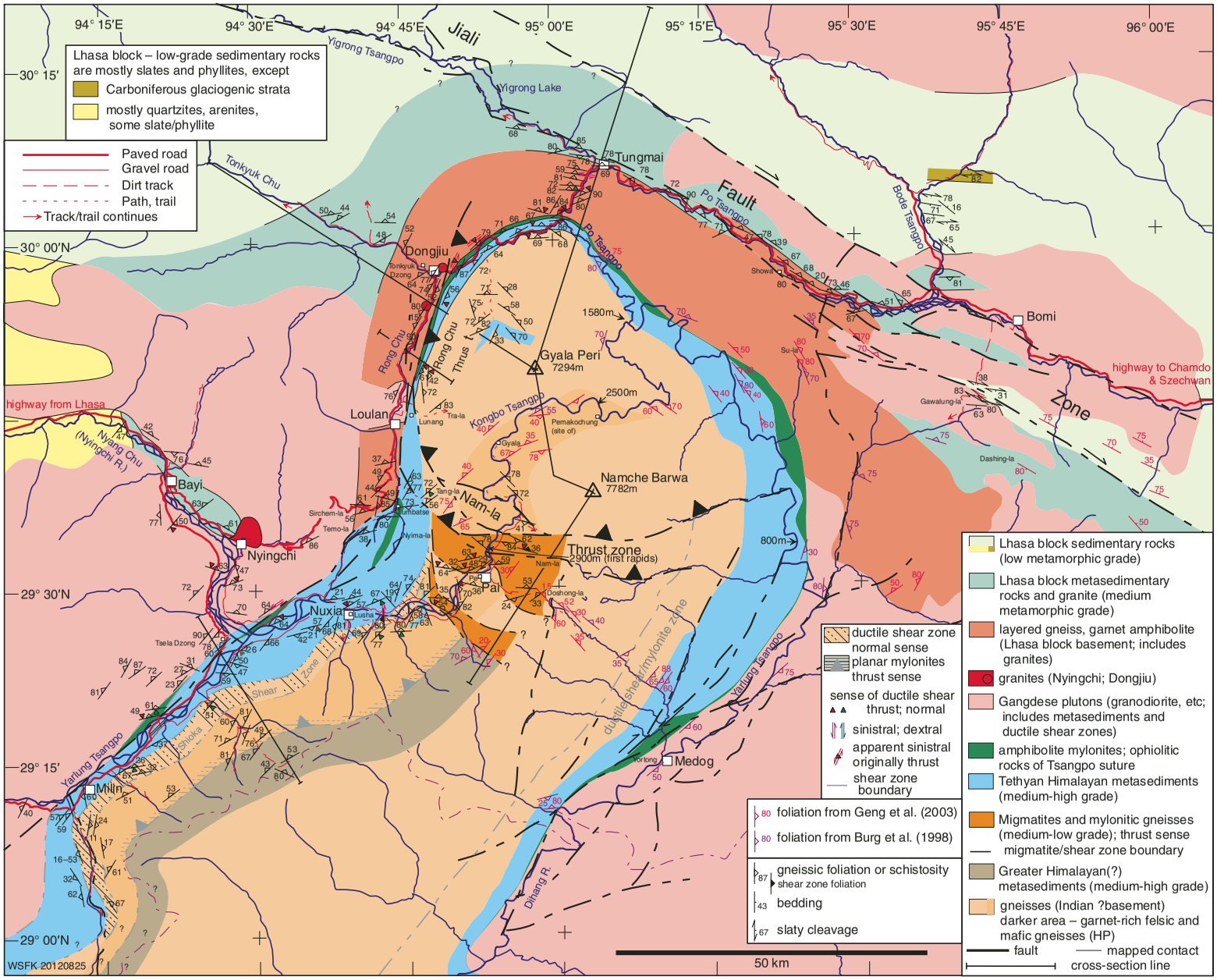

Figure 3. Geological map of the Namche Barwa antiform and surrounding region, based on our observations in the field, supplemented by information from Geng et al. (2003) and Burg et al. (1998) and interpretation of Landsat Thematic Mapper (TM) satellite images. Base map constructed from TM satellite image mosaic in Universal Transverse Mercator (UTM) zone 46 projection; the image mosaic for the same area is shown in Figure 5. Locations of cross sections of Figures 7 and 8 shown. HP—high pressure. More structural information, including lineation, and brittle structure orientations not shown here are included on larger scale versions of this map found in Figure DR1 (see footnote 1).

reach as the Parlung Tsangpo and limit the name Po Tsangpo to the very short reach extending from Tungmai to the Yarlung Tsangpo confluence.

Overview of Geodynamic Setting

At both their eastern and western ends, the Himalaya terminate in large syntaxes defined by progressive changes in the strike of geologic units and structures. These syntaxes represent an upper crustal manifestation of processes associated with the boundaries of the indenting Indian lithospheric plate and continent (Zeitler et al., 2001a). Although the nature of the northwestern and northeastern plate margins are somewhat different, both margins share several features, including a tight structural reentrant defined by the main frontal thrust, very large orogen-crossing rivers that feed into these reentrants (Indus and Yarlung Tsangpo), and the presence of an active antiformal metamorphic massif located on the inner limb of the syntaxis (Nanga Parbat and Namche Barwa).

These metamorphic massifs, at Nanga Parbat in the west and Namche Barwa–Gyala Peri in the east, represent the geologic termini of the Himalaya. Located within very steep glacially and fluvially dissected terrain, both massifs contain prominent high peaks that together with throughcutting river gorges define more than 7 km of relief. Studies first at Nanga Parbat and more recently at Namche Barwa have shown that these massifs have been loci of very high erosional exhumation rates of 5 mm/yr or more for at least several million years. As such they are major contributors to the sediment load and geochemical signatures of the Indus and Tsangpo Rivers, even though they amount to only a few percent of these rivers' watersheds (Singh and France-Lanord, 2002; Garzanti et al., 2004; Stewart et al., 2008; Enkelmann et al., 2011).

Regional Tectonic Evolution

Southeastern Tibet was assembled by the consecutive collision of several terranes in the Mesozoic, one of which, the Lhasa block (Yin and Harrison, 2000; Zhu et al., 2011), underlies much of the area we sampled. The Indus-Tsangpo suture is the terrane boundary between the Lhasa block and the Indian plate rocks that make up the Himalaya (Yin and Harrison, 2000), although significant younger structures have overprinted this zone (Yin et al., 1994; Quidelleur et al., 1997; Ding et al., 2001; Zhang et al., 2004; see following). During the Mesozoic and early Cenozoic, an Andean arc developed along the southern Lhasa block, leading to the diachronous emplacement of voluminous granitoids into the Lhasa block basement along with eruption of the Linzizong volcanic rocks; these granitoids make up the Gangdese batholith and related units located to the east (e.g., Wen et al., 2008; Booth et al., 2004; Chiu et al., 2009). Other phases of intrusive magmatic activity also occurred, including emplacement of large plutons during the Permian and adakites during the Neogene (Zhu et al., 2010; Chung et al., 2003). The timing for initiation of collision between India and Eurasia in the central and eastern Himalaya is well constrained as ca. 51–52 Ma (Zhu et al., 2005; Najman et al., 2010).

In southeastern Tibet these fundamental orogenic components have been bent into the arcuate topographic and structural trends that define the eastern Himalayan syntaxis (Fig. 1), the crustal manifestation of the region's location astride the Indian plate's eastern indentor corner. Spatially the region displays a transition from convergent and arc-normal extensional tectonics in the west to strike-slip faulting in the Three Rivers region, and this pattern holds for both older rocks and the modern deformation field, as shown by GPS and seismological results (Gan et al., 2007; Sol et al., 2007). Temporally, as expected for an indentor corner, the region has a complex structural evolution, with a variety of active young structures superimposed on older convergent-margin features.

Crustal Structure

Within the northwestern portion of the eastern syntaxis, the Indus-Tsangpo suture and the Himalaya terminate in the north-plunging Namche Barwa antiform, which transitions along strike to the Namche Barwa metamorphic massif (Fig. 3; Burg et al., 1997, 1998). In the Namche Barwa massif, Indian basement rocks (Xu et al., 2010) have been exhumed from beneath the overthrust Lhasa block. Immediately adjacent to the massif, Lhasa block basement rocks are exposed, not Gangdese plutons, suggesting the possibility of some more regional upwarping in addition to the large amounts of rock uplift within the fault-bounded antiform. Within ~10 km of the northern end of the Namche Barwa massif, the right-lateral Jiali fault zone strikes northwest to southeast across the region through rocks of the Lhasa block (Armijo et al., 1989; Lee et al., 2003).

Uplift of the antiform and massif has deflected the trace of the Indus-Tsangpo ophiolitic suture and the adjoining belt of Tethyan Himalayan metasedimentary rocks, which wraps around this structure. On the northwestern, northern, and northeastern margins of the massif, the suture and the Tethyan belt are variably overprinted by active, steep faults. The steep western boundaries of the antiform and massif have accommodated vertical motions and, in the view of several groups, sinistral strike-slip faulting (Burg et al., 1998; Ding et al., 2001; Geng et al., 2006) accommodated northward growth of the antiform (Burg et al., 1998; Seward and Burg, 2008). To the immediate south and southwest of the massif, along the axis of the antiform, the Nam-la thrust system separates the active metamorphic Namche Barwa massif from crystalline basement rocks of the main Himalaya sequences within the antiform (Craw et al., 2005; Kidd et al., 2006). We discuss these relationships in more detail in the following.

Regionally, receiver-function data show a broad 10–15 km upwarp of the Moho approximately centered on the Namche Barwa antiform, with crustal thicknesses decreasing from ~70 to 55 km across the southeastern Lhasa block (Fig. 1; Zurek, 2008). Shear-wave splitting results show an arcuate strain pattern in Lhasa block rocks surrounding the Namche Barwa antiform

that is consistent with the strain observed in geological units as well as that derived from observations of GPS velocities, suggesting a complex strain field (Sol et al., 2007). Results from receiver-function common conversion point stacks (Zurek, 2008) show that a high-velocity, high-impedance, lower crustal layer seen along the southern margin of much of the Lhasa block, interpreted to be eclogite (Kind et al., 2002; Schulte-Pelkum et al., 2005; Hetényi et al., 2007; Nábelek et al., 2009), terminates west of the antiform.

Metamorphism and Magmatism

The Namche Barwa–Gyala Peri metamorphic massif exposes high-pressure, complex polymetamorphic Indian plate gneisses (Figs. 3 and 4). Peak conditions exceeded 800 °C and 14 kbar and involved considerable melting (Liu and Zhong, 1997; Xu et al., 2010; Guilmette et al., 2011; Su et al., 2012). These rocks also underwent a late Neogene, probably ongoing episode of partial melting and rapid rock uplift marked by a sharp decompression path (Burg et al., 1998; Ding et al., 2001; Booth et al., 2004, 2009; see following). Most of the young anatectites appear to be sourced from decompression melting of protolith along with some fluid-present melting (Booth et al., 2004). The lower pressure granulite overprint appears to be limited to the northernmost portions of the Namche Barwa antiform, adjacent to higher pressure rocks that also appear to be affected by this recent metamorphic episode (Liu and Zhong, 1997; Booth et al., 2009). For current river-level exposures, total exhumation associated with the recent lower pressure metamorphism has been at least 20 km, although the higher pressure rocks may have been exhumed from depths of as much as 50 km. Hot springs are common near and in the Namche Barwa massif and serve as evidence that rapid rock uplift has steepened the geotherm; Craw et al. (2005) reported fluid-inclusion data that support local geothermal gradients in excess of 50 °C/km over the upper 2.5–6 km of the crust.

Immediately outside the Namche Barwa antiform and massif, the dominant igneous rock types emplaced into the Nyingchi Complex basement of the Lhasa block are granitoids associated with the Mesozoic–early Cenozoic Gangdese batholith and later crustal melts (Guo et al., 2012). Along the Jiali fault zone, small volumes of pegmatite crosscut the ductile foliation in the gneisses and give ages of ca. 21 Ma (Booth et al., 2004). A small adakitic granitoid west of the antiform was emplaced ca. 26 Ma (Chung et al., 2003).

Metamorphic Timing and Exhumation-Rate Constraints

The pressure-temperature (*P-T*) history of rocks in the antiform is complex. While there is a range of views over the extent of early Cenozoic metamorphic events (e.g., Ding et al., 2001; Zhang et al., 2012), there has emerged a consensus that the high-pressure gneisses underwent episodes of metamorphism ca. 24

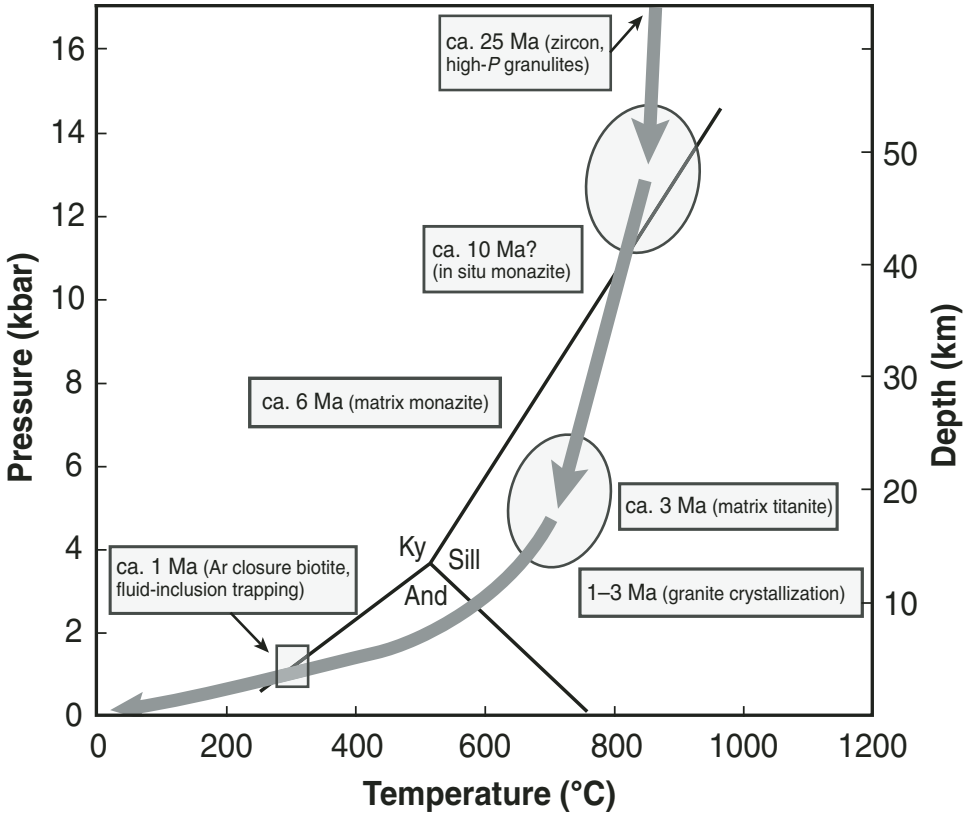

Figure 4. Schematic pressure (*P*)-temperature-time evolution for the Namche Barwa massif, synthesized from Booth et al. (2009) and additional data reported and summarized by Su et al. (2012). The polyphase metamorphic evolution of Namche Barwa basement has culminated in an episode of decompression, anatexis, and fluid infiltration that probably continues at present. Ky—kyanite; Sill—sillimanite; And—andalusite.

and 18 Ma, the 24 Ma zircon ages corresponding to metamorphic conditions of slightly >800 °C and 14–18 kbar and the younger ages reflecting decompression-related effects (Xu et al., 2010; Zeng et al., 2012; Su et al., 2012; Guilmette et al., 2011). Within the Namche Barwa–Gyala Peri massif, young ages on dikes and migmatites have been reported ranging from ca. 11 Ma to ca. 3 Ma near Namche Barwa peak (Burg et al., 1998; Ding at al., 2001; Booth et al., 2009). At a more northern location around Gyala Peri peak, younger granites and migmatites are much more abundant and give ages as young as 0.9 Ma (see following). For these rocks Booth et al. (2009) reported *P-T* estimates and accessory mineral ages that can be combined to give long-term mean exhumation rates of 5 mm/yr or more over at least the past 5 m.y. (Fig. 4).

Cosmogenic isotope studies yield thousand-year-scale erosion rate estimates of nearly 4 mm/yr for small basins near but not within the Namche Barwa massif (Finnegan et al., 2008). Thermochronological provenance studies of detrital zircon fission-track ages give an estimate for recent incision or erosion rates of 10 mm/yr for the massif (Stewart et al., 2008; Enkelmann et al., 2011). These data and rates are consistent with thermochronological data reported from near and within the Namche Barwa antiform, including young K-Ar dates summarized in Burg et al. (1998), several young biotite ages reported by Xu et al. (2012), and in particular the fission-track data reported by Seward and Burg (2008). Seward and Burg (2008) reported zircon fission-track ages as young as 0.2 Ma and apatite fission-track ages as young as 0.4 Ma from within the metamorphic massif. Such young ages suggest very rapid exhumation rates (see following discussion).

Outside the Namche Barwa antiform, relatively few geochronological and petrological data are available for basement rocks in southeasternmost Tibet. Guo et al. (2012) reported that Nyingchi Complex orthogneisses originally emplaced ca. 85 Ma were later metamorphosed between 65 and 46 Ma and that these rocks also show evidence for anatexis of metasediments as recent as ca. 40 Ma. Quidelleur et al. (1997) reported $^{40}Ar/^{39}Ar$ results for biotite and K-feldspar data that recorded thermal perturbations related to motion along the Rengbu-Zedong backthrust, well to the west of the antiform, between ca. 15 and 19 Ma, as well as more rapid, regional southern Lhasa block cooling starting ca. 10 Ma. Well to the southeast of the antiform, Lee et al. (2003) measured a few biotite and K-feldspar samples from rocks along the Jiali fault and obtained ages between 8 and 12 Ma. Duvall et al. (2012) reported a range in apatite U-Th/He age of 1.2–14 Ma for 19 detrital apatites from a small watershed to the east-northeast of the antiform. Ding et al. (2001) and Xu et al. (2012) reported several mica and amphibole $^{40}Ar/^{39}Ar$ mineral ages from west of the metamorphic massif that are generally in the range 10–20 Ma.

Topography and Landscape Evolution

The topography and drainage networks of southeastern Tibet reflect the transitions seen in geology, tectonic style, and especially crustal strain. Across the region, the high-elevation low-relief terrain and internal drainage of the archetypical Tibetan Plateau give way toward the southeast to increasingly rugged gorges associated with rivers that, particularly in the east, are pulled into close alignment by the strike-slip faults in the Three Rivers region (Hallet and Molnar, 2001; Fig. 1). Study of incision into the Tibetan topographic margin farther to the east and northeast suggest that accelerated incision took place starting ca. 8–10 Ma (Clark et al., 2005; Ouimet et al., 2010). Across the region, mean elevation decreases as local relief increases, exceeding 7 km near Namche Barwa in the lower Yarlung Tsangpo gorge.

There remains considerable uncertainty about the overall timing and sequence of Tibetan surface uplift. Earlier ideas that at least the southern margin of Tibet was uplifted ca. 8–10 Ma (e.g., Molnar et al., 1993; An et al., 2001) have been challenged by data showing that parts of the Lhasa block have been near current elevations since the mid-Cenozoic (e.g., DeCelles et al., 2007; Rowley and Currie, 2006). Radiogenic isotope data from granites can be interpreted to suggest that the southern Tibetan crust was thin and not elevated until more recently (DePaolo et al., 2008), but the southern and eastern parts of the Lhasa block underwent considerable late collisional contractional deformation along the Gangdese and Renbu-Zedong thrusts (Yin et al., 1994, 1999; Quidelleur et al., 1997). Copeland et al. (1987) and Richter et al. (1991) presented data showing that a significant pulse of exhumation in southern Tibet began ca. 18 Ma, a pulse large enough that it must have been accompanied or preceded by substantial surface uplift. Significant portions of the Lhasa block, while dissected by large rivers like the Tsangpo and Nyang, display a relatively low relief topography at higher elevations of 4–5 km. This topographic surface could either be a relict landscape of the sort studied by Clark et al. (2005) or a younger landscape that reflects an active process such as the glacial buzzsaw of Brozović et al. (1997). It is possible that the topography in southeastern Tibet is a collage shaped by a range of processes over an extended time.

In contrast to the more subdued and likely older landscapes in much of southeastern Tibet, the relief within the Namche Barwa massif is extreme where the Yarlung Tsangpo River exits the Tibetan Plateau in the deep gorge that it cuts across the massif. Drainages are tortuous within the massif (Koons et al., 2013) where the Yarlung Tsangpo makes a 180° turn toward the foreland that includes many offset reaches suggestive of structural control (Fig. 5). There are numerous steep rapids along the river as well as Rainbow Falls, which accounts for a >30 m drop in the river (Baker, 2004) across what is probably a recent or active structure, given the high stream power in the area (Finnegan et al., 2008). Within the massif, the Yarlung Tsangpo flows along an immense knickzone, dropping ~2000 m in elevation in what is often referred to as the Big Bend gorge; over one 60 km reach the contorted river drops ~1100 m across an east-west distance of only 11 km. Rivers that flow into the knickzone (Yigrong Tsangpo, Po Tsangpo, Rong Chu, and tributaries; Figs. 2 and 3) together define a complex, convergent flow pattern. In this area, river power is highest just where local relief reaches a maximum,

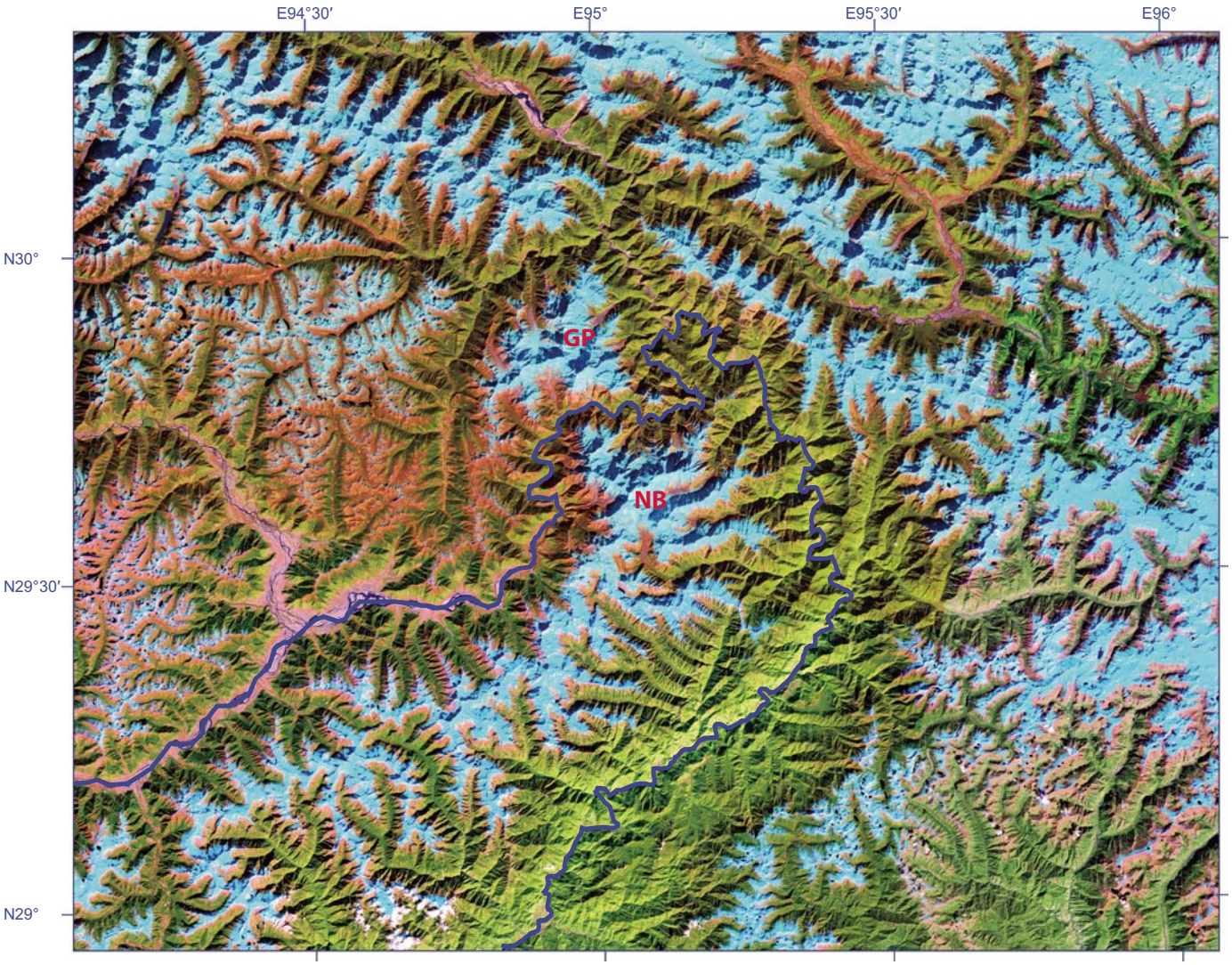

Figure 5. Image mosaic constructed from Landsat 7 Thematic Mapper (TM) satellite images for the same area as the geological map of Figures 3 and DR1. Image info: projection Universal Transverse Mercator (UTM) zone 46; resolution 30 m/pixel. The mosaic includes parts of images of TM paths 134–136, rows 39 and 40; image acquisition dates of 23 October 2001 (for path 134); 15 November 2001 (for path 135); 24 December 2001 (image 136–39), and 19 December 1999 (image 136–40). Images processed using ERDAS ER Mapper software. Dark blue line shows course of Yarlung Tsangpo River. GP and NB—Gyala Peri and Namche Barwa peaks.

an indication that high rock uplift rates must have been in play for a considerable time across a stationary knickzone (Finnegan et al., 2008).

Koons (1995) suggested that river capture is likely within indentor corners because of the combination of concentrated erosion that occurs within syntaxes, the strong gradients in elevation, and the redirection of rivers caused by the evolving deformation field that includes strike-slip offsets that are conducive to capture. Several others have suggested that the Tsangpo was relatively recently captured by the Brahmaputra system, with the Big Bend knickzone and the complex nearby drainages remaining as remnants of the capture (e.g., Seeber and Gornitz, 1983; Brookfield, 1998; Zeitler et al., 2001a; Clark et al., 2004). Alternative or additional scenarios include capture of the Po Tsangpo into the Yarlung Tsangpo (Burchfiel et al., 2000; Seward and Burg, 2008); this seems plausible given current river flow patterns (Figs. 2, 3, and 5).

Massif Geodynamics

Syntaxes are regions of complex tectonics and dynamics and there are several views as to how the broader Namche Barwa structure developed. Recognizing the antiformal nature of the structure, based on two-dimensional (2-D) finite-element modeling, Burg and Podladchikov (1999) suggested that Namche Barwa is a crustal-scale buckle fold. The 3-D models of collision

and indentation show that foci of vertical strain develop within the complex and evolving strain field near the edges of the collisional zone (e.g., Koons et al., 2013).

How such vertical strain specifically comes to be manifested as a feature like Namche Barwa is not clear. Burg et al. (1998) viewed the main forcing at Namche Barwa to be tectonic, with erosion playing a secondary role in response. In Zeitler et al. (2001a, 2001b) and Koons et al. (2002, 2013) it was proposed that the Namche Barwa–Gyala Peri massif was an example of a tectonic aneurysm like the Nanga Parbat–Haramosh massif in the western Himalaya. Such a feature involves coupling between surface and tectonic processes such that advective steepening of the shallow geotherm by focused, rapid, and significant erosion will weaken the normally strong upper crust, leading to a focusing of strain, which in turn enhances or supports the weakening process while promoting development of the topographic relief that can permit continued rapid exhumation. Finnegan et al. (2008) reported observations consistent with such coupling and argued that it was unlikely that the metamorphic and surface-process anomalies at Namche Barwa would just happen to coincide with an antiformal fold. Positive feedbacks are difficult to demonstrate and the matter is not settled; we discuss this issue in more detail in the following.

OBSERVATIONS AND RESULTS

The sections that follow discuss observations from structural geology, seismicity, metamorphic geochronology, and thermochronology. In addition to the tables and figures associated with these observations, the Data Repository (see footnote 1)[1] includes a number of data files in Keyhole Markup Language (KML) format, which permits easy comparisons of geology, topography, structures, seismicity, and cooling ages.

Structural Geology

Figure 3 presents a synthesis of our structural observations along with data from previously published maps and data (Burg et al., 1998; Geng et al., 2003). Figure DR1 (see footnote 1) is the same map but at larger scale and containing more detail of individual structural measurements. Most of our data are from the western and northern portions of the antiform and massif, as our several attempts to access some eastern portions were prevented by both impassable terrain and access restrictions.

[1]GSA Data Repository Item 2014215, Figure DR1: Detailed geological map of massif; Figure DR2: Cartoon showing proposed origin of Namche Barwa structures; File DR1: Mineral cooling ages (kmz); File DR2: Earthquake epicenters (kmz); File DR3: Geologic map, DEMs, and TM image (kmz); File DR4: Cooling ages and location; Table DR1: U-Pb analytical data; Table DR2: U-Pb age compilation; Table DR3: Cooling-age sample information; Table DR4: U-Th/He apatite analytical data; Table DR5: U-Th/He zircon analytical data; Table DR6: $^{40}Ar/^{39}Ar$ biotite analytical data; Table DR7: $^{40}Ar/^{39}Ar$ K-feldspar step-heating and inversion data; and Table DR8: Thermal modeling parameters, is available at www.geosociety.org/pubs/ft2014.htm, or on request from editing@geosociety.org or Documents Secretary, GSA, P.O. Box 9140, Boulder, CO 80301-9140, USA.

Northwestern Margin of the Antiform Adjacent to the Yarlung Tsangpo (Milin-Lusha)

Ductile sense of shear indicators within the highly strained Tethyan Himalayan metasediments along the Tsangpo between Milin and Lusha (Fig. 3) show both thrust sense and normal sense, associated with generally north- to northwest-plunging stretching lineation orientations (Fig. 6, stereonets 8–9). Local south-dipping foliations and sense-of-shear indicators in these units are reoriented by secondary folding. We interpret this as evidence for Himalayan imbrication and underthrusting of the Tethyan shelf strata of India, followed by extension of this stack by distributed extensional strain related to the South Tibetan detachment system. We attribute the difference between the expression of the South Tibetan detachment system structures here, compared with the better studied part in the central Himalaya (Burchfiel et al., 1992; Edwards et al., 1999), to exposure along the northwest margin of the massif of more deeply exhumed, originally more northern parts of the South Tibetan detachment system. During extension these operated largely or entirely under ductile conditions, and only recently were exhumed to the brittle level by the younger rise of the Namche Barwa antiform. While parts of these Tethyan metasedimentary schists and gneisses are highly strained, with significant simple shear, other parts are not so intensely foliated, and may be largely the products of pure shear strain; shear-sense indicators are not particularly common in them.

This part of the antiform contains a prominent normal-sense shear zone (Shioka shear zone) between largely retrograde granulite quartzofeldspathic gneisses of Indian crust origin, and overlying Tethyan Himalaya-origin amphibolite facies metasedimentary rocks [Figs. 3, 6 (stereonet 7), and 7 (section C)]. Because we found no obviously suitable igneous material for dating this normal-sense shear zone, we remain uncertain whether it may be equivalent to the South Tibetan detachment system known to occur at this relative structural position from ~400 km west of here, or whether it may represent an older shear zone from the emplacement of the granulites into the mid-crust, possibly by buoyant return from attempted subduction of the leading edge of Indian continental crust in the early stages of the India-Asia collision. The stretching lineation orientation in this shear zone, combined with superimposed secondary folding, leads to the low and variable plunge directions (Fig. 6, stereonet 7). The overall extension direction is highly oblique to the present outcrop belt of this shear zone, and it is not entirely clear that it necessarily represents the same extensional event found in some of the shear indicators in the Tethyan metasedimentary unit.

A belt of largely retrograded granulites is structurally above and in contact with a unit of amphibolite facies psammite and/or pelite metasediments near the Himalayan crest. We interpret this contact and the local mylonites along it as a significant thrust structure; no datable rocks were found cutting it, and it could be equivalent to some component of the Main Central thrust of the Himalaya, or it could be a much earlier Himalayan structure, perhaps also related to early exhumation of the granulites.

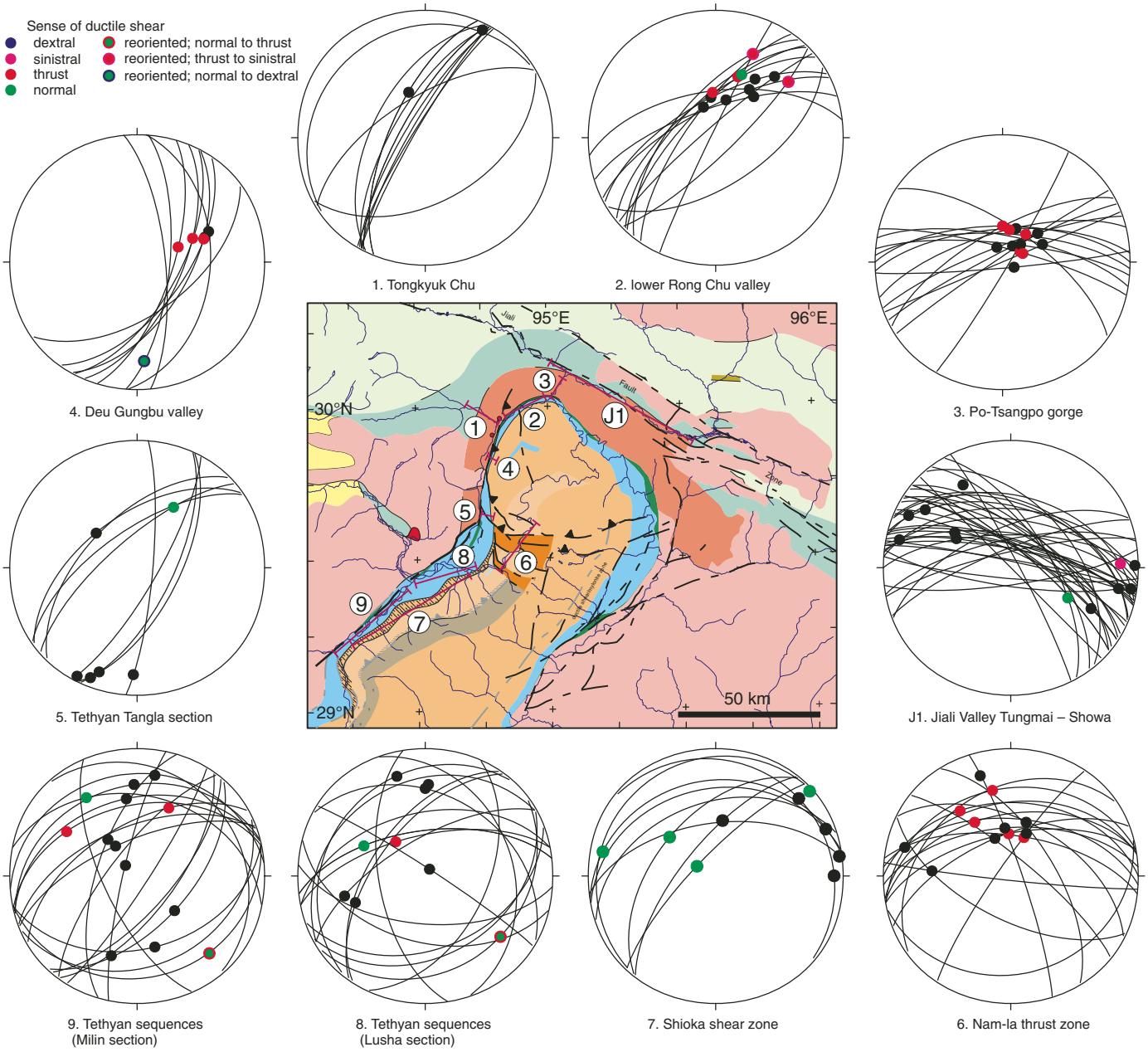

Figure 6. Orientations of ductile foliation, lineation, and shear-sense determinations in different localities of the Namche Barwa structure identified by the numbered markers and lines in the map in the center of the figure. Shear sense shown by the colored lineation spots in the stereonets is relative to present orientation (red—reverse; green—normal; magenta—left lateral; blue—right lateral; black—not determined). For shear-sense items where reorientation by later strain has inverted or changed the original slip sense, the center color gives the original sense and the outer ring the present apparent sense. Lower hemisphere, equal-angle stereographic projections.

Ductile strain in the Gangdese batholith granitoid rocks near the Nyang River south of Bayi is expressed by local foliated zones (including some pelitic metasediments) that have predominantly thrust sense shear on foliation subparallel with the Tsangpo suture to the southeast. While these zones have not been isotopically dated, these may be Himalaya-age structures related to the early Miocene Gangdese thrust farther west near Lhasa and Zedong (Yin et al., 1994).

Western and Northwestern Margin of the Massif (Lulan–Rong Chu Valley–Po Tsangpo)

Both the thrust- and the normal-sense ductile shear events outlined here can also be recognized along the northward extension of the Tethyan metasedimentary belt and in the adjacent mafic and quartzose gneisses of the attenuated Tsangpo suture as they pass along the western side and around the northern end of the Namche Barwa massif (Fig. 3; Fig. DR1). They remain

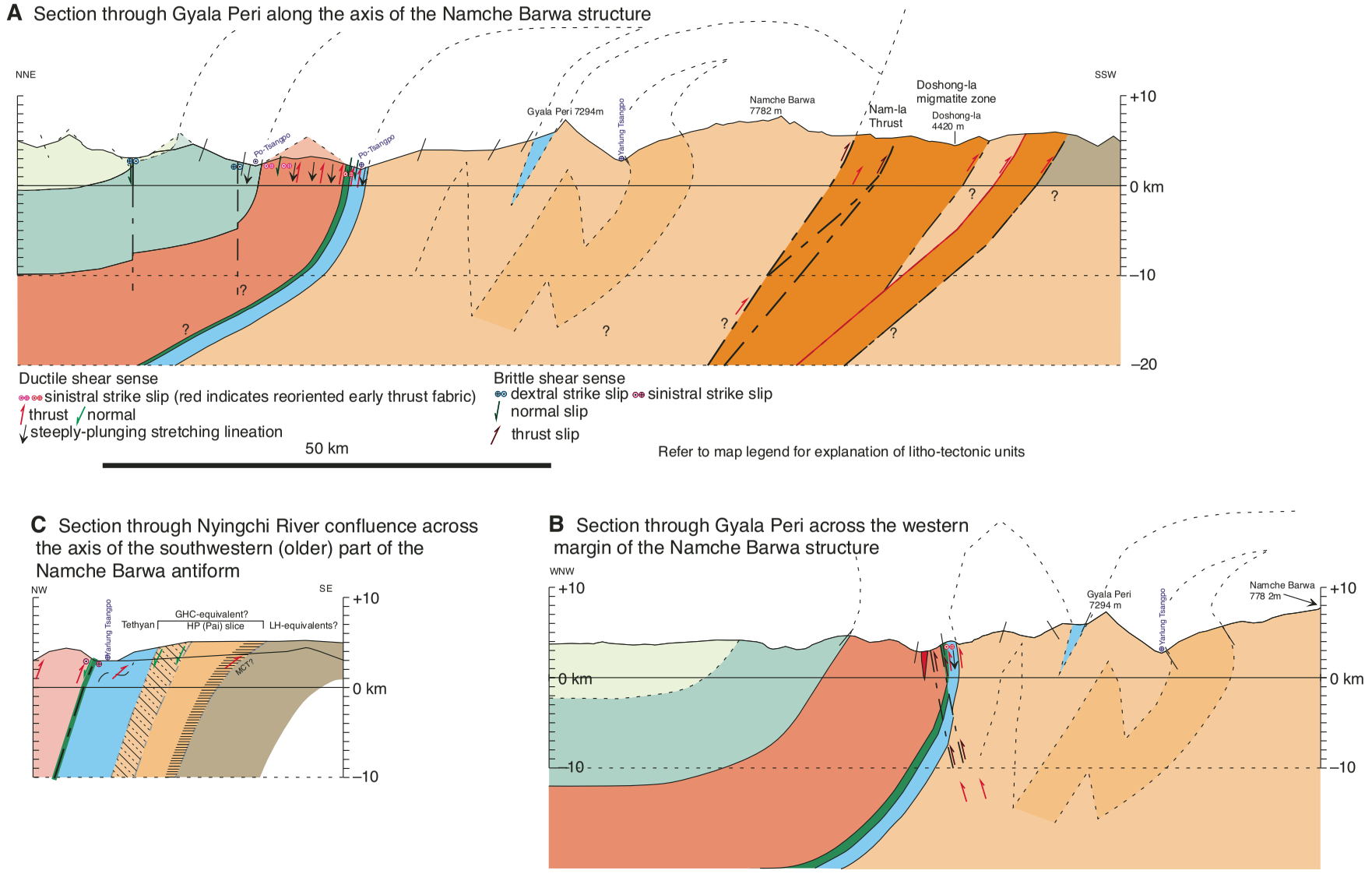

Figure 7. Cross sections of parts of the Namche Barwa antiform and massif; locations of the section lines are shown in Figure 3. No vertical exaggeration. Lithotectonic unit colors are the same as for the geological map of Figure 3. Abbreviations: MCT—Main Central thrust; GHC—Greater Himalayan Crystallines; HP—HP–High pressure; LH—LH–Lesser Himalayan.

associated with a strong stretching lineation that restores to approximately north-south orientation if the crustal-scale fold of the Namche Barwa structure is removed. The containing rock units previously formed a gently north-dipping planar high-strain zone, originally developed as an early location of the Main Himalayan thrust, and subsequently in part reused with extensional motion, probably of the South Tibetan detachment system episode. Along the western and northwestern margin of the massif (Lulan and Rong Chu valley), the stretching lineation from these events is currently subhorizontal to gently plunging and shows apparent strike-slip sense of shear of either left-lateral or right-lateral sense (e.g., Fig. 6, stereonets 2, 4, and 5); we think it should not be interpreted to indicate actual ductile strike-slip displacement because the relative structural chronology and the map relationships show that this lineation and associated shear-sense indicators must predate the large-scale folding effects of the Namche Barwa massif.

The rocks of the northern margin of the Namche Barwa antiformal structure, exposed along the lower Rong Chu and up the Po Tsangpo to ~2 km south of the Tungmai bridge, contain a gneissic foliation and one variably developed stretching lineation (Fig. 6, stereonets 2 and 3), which similarly can be restored with approximately north-south–oriented lineation in a gently north-dipping planar zone. This section appears not significantly affected by brittle faulting, based on the available outcrops; it appears to be just the steeply plunging northern termination of the crustal-scale antiform of the Namche Barwa massif broadly characterized first by Burg et al. (1997).

Rong Chu Shear and Fault Zone

On the western margin of the massif, along the eastern edge of the Lulan Valley, and north along the eastern wall of the upper Rong Chu valley down to Dongjiu, there is a younger localized zone of ductile strain and faulting. The ductile stretching lineation of this zone plunges steeply on steeply east-dipping foliation (Fig. 6, stereonet 4), and shear-sense indicators show east-side-up thrust sense in the present orientation. The colocated brittle faults, which are abundant in the western part of this zone near the foot of the topographic slope and are well exposed in the Deu Gungbu section, have dominantly east-side-up (thrust sense) slickenlines on steeply east-dipping to subvertical faults, many of these containing much fault gouge (Fig. 7, section B; Fig. 8; Fig. 9, stereonets F1 and F2). The age of initiation of this shear zone is constrained by a U/Pb zircon age of 16 Ma from a foliated granite in the ductile part of this zone (Booth et al., 2004). We link this young ductile and brittle shear and fault zone to the Nam-la thrust zone (Fig. 3).

Nam-la Thrust Zone

The Nam-la thrust zone, first reported by Craw et al. (2005), initiated in dioritic migmatites and mylonites with south-directed shear sense, progressed to S/C mylonites, and then to brittle faulting localized in the northern part of the overall steeply north-dipping thrust zone (Fig. 3; Fig. 7, section A). Ductile foliation dips moderately to steeply, mostly north to northeast, with thrust shear sense in all but one case (Fig. 6, stereonet 6). The dioritic migmatites and these ductile structures are in two zones; the southern one is narrower and entirely ductile, and most of the brittle

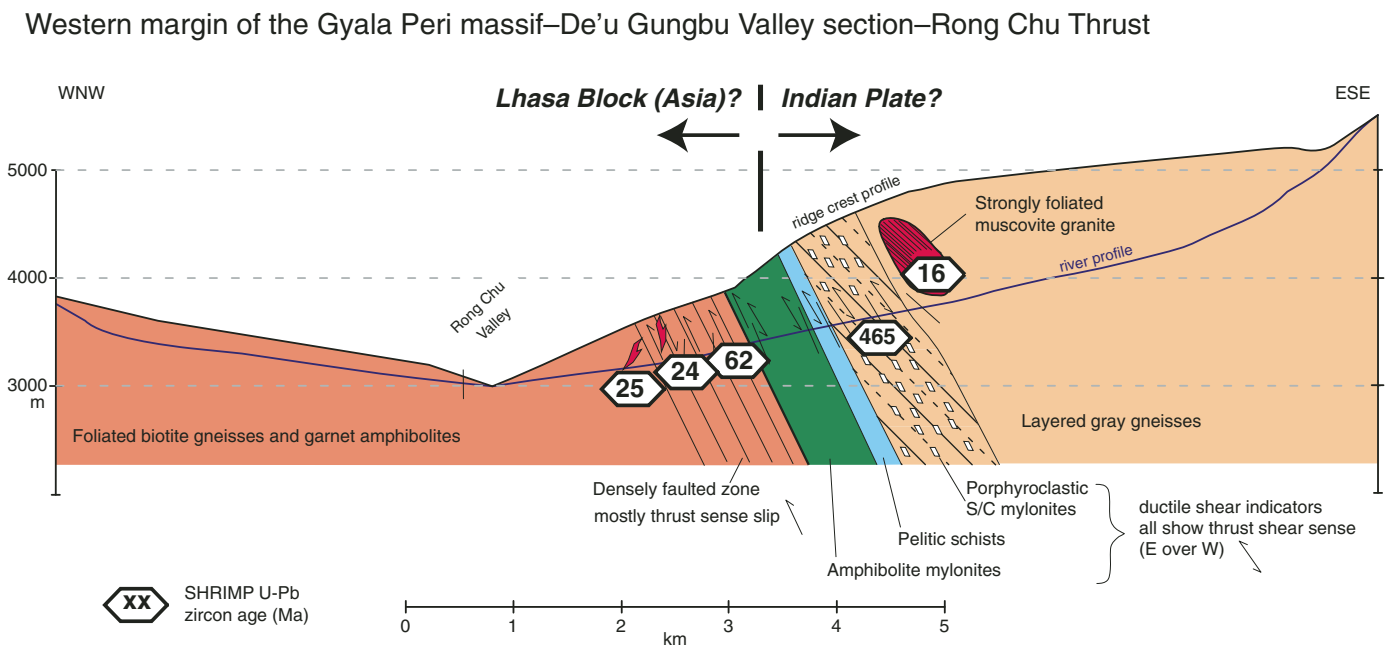

Figure 8. Cross section across the Rong Chu valley and along the Deu Gungbu side valley on the western side of the Gyala Peri massif, showing the position of the Rong Chu thrust fault and ductile shear zone. Section location and lithotectonic unit colors are shown in Figure 3; no vertical exaggeration. Isotopic ages are from Booth et al. (2004); see text for discussion. SHRIMP—sensitive high-resolution ion microprobe.

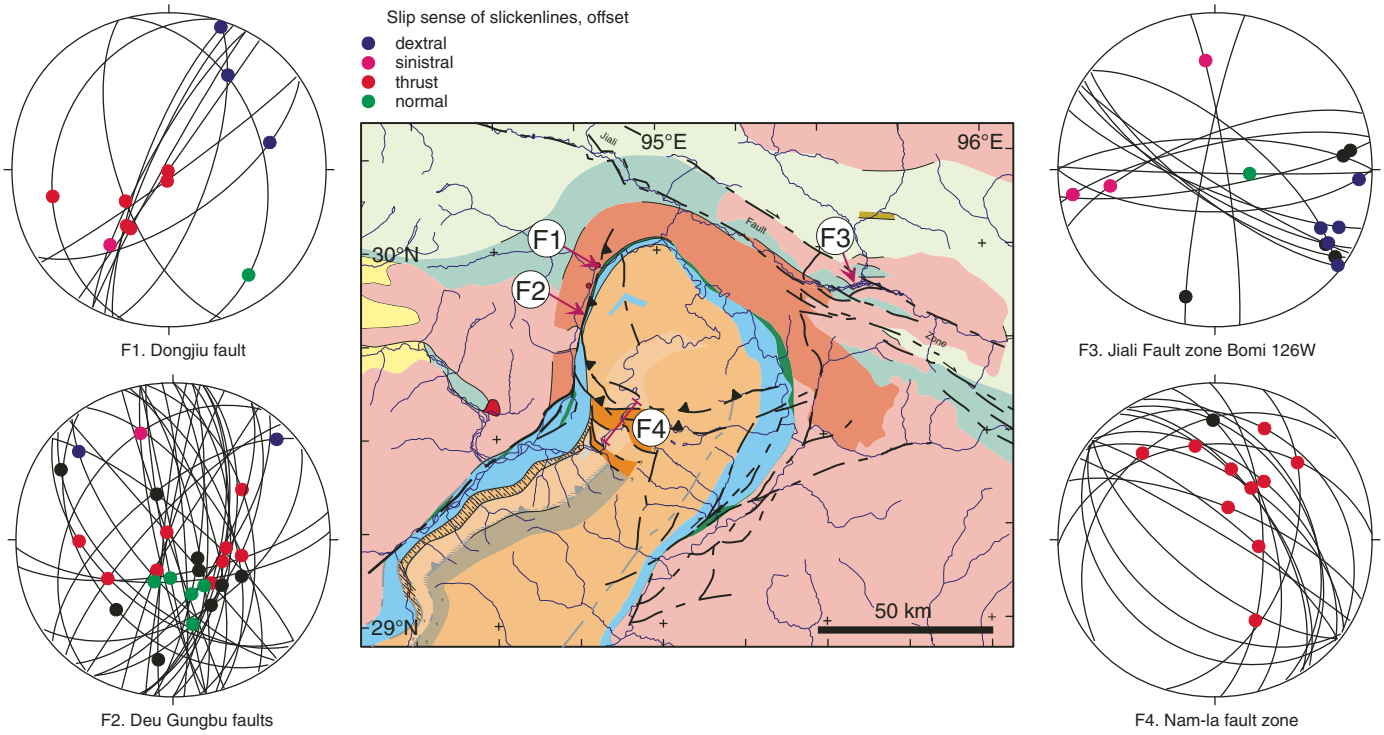

Figure 9. Orientations of brittle structures, including faults, and slip-sense determinations in different localities of the Namche Barwa structure identified by the numbered markers and lines in the map in the center of the figure. Slip sense shown by the colored slickenline spots in the stereonets is relative movement of the upper block (red—reverse; green—normal; magenta—left lateral; blue—right lateral; black—not determined). Lower hemisphere, equal-angle stereographic projections.

faults are localized in the northern half of the wider zone (Fig. 3; Fig. 7, section A). This brittle fault zone contains thrust-sense, broadly north- to northeast-dipping, faults (Fig. 9, stereonet F4), and crosses the Yarlung Tsangpo at the location of the first rapids (the upstream side of the major knickpoint on the river). The quartz dioritic melts of the Doshong-la migmatites appear to be involved with shear structures of the early ductile development of the Nam-la thrust zone and are not involved as melts in later S/C ductile fabrics; they are thus confined in relative terms to the high-temperature early development of this zone. They are also, in the confines of the Nam-la thrust zone, abundant and distinctive compared with the small volumes of more siliceous granitoid melts encountered in most places elsewhere in the massif. As this zone passes into the shear and fault zone along the western margin of the Namche Barwa massif, the migmatites decline in abundance, and they were not found along the western margin. This structure separates the rapidly exhuming Namche Barwa massif core from the antiform to the southwest that contains somewhat older cooling ages (see following).

Jiali Fault Zone in the Yigrong and Po Tsangpo Valley

A few outcrops of the Jiali fault, showing a narrow zone (~10–20 m) of fault gouge, occur near the axis of the Po Tsangpo valley from near Tungmai east-southeast toward Bomi. Clear, but sparing, indicators of brittle right-lateral strike-slip sense were observed in bedrock along this fault valley, although an outcrop of granodiorite studied in a roadcut near the Bode Tsangpo confluence showed common left-lateral slickensides as well (Fig. 9, stereonet F3). We were unable to determine a total slip on the Jiali fault in this area from bedrock markers; it might be possible to do this using the medium-low metamorphic grade boundary in the Lhasa block metasediments near Yigrong Lake (Fig. 3), but our observations were not sufficiently widespread and do not constrain adequately the position and attitude of this boundary near the fault (the appearance of no offset in Fig. 3 should not be taken to suggest that this is the case). If the Bode-Tsangpo valley north of the fault near Bomi is the offset head of the drainage that continues in the Po Tsangpo gorge from Tungmai, then the total offset so defined would be ~60 km; such an offset is consistent in magnitude with that estimated by Armijo et al. (1989) farther west along the Jiali fault.

Along the Yigrong and Po Tsangpo valleys ductile structures in Lhasa block basement gneisses and overlying amphibolite-grade metasediments in most places continue the steep foliation seen in the Po Tsangpo gorge south of the Tungmai bridge. However, near that bridge and a few locations elsewhere, most near Tungmai, a moderate to weakly developed stretching lineation is gently to moderately plunging (Fig. 6, stereonet J1), giving apparent strike-slip displacement in the present orientation. Convincing associated shear-sense indicators were not found except in one example near the bridge that showed left-lateral shear

sense. Pegmatitic granitoid dikes dated by zircon U/Pb analysis as 21 Ma (Booth et al., 2004) crosscut this subhorizontal lineation and the foliation. Because the steeply dipping foliation of the gneisses of the Po Tsangpo gorge section has, without much doubt, been reoriented from a subhorizontal attitude by the rise of the Namche Barwa massif and antiform, we suggest that it is probable that this pre–21 Ma ductile lineation reflects local mid-crustal deformation in the Lhasa block crust, but is not related to the Jiali fault zone, a much younger feature (Armijo et al., 1989). Near the Tungmai bridge and elsewhere we found no evidence for higher ductile strain such as might be indicative of a detachment fault or differences in type and geometry of ductile foliation and lineation across the contact between granitoid gneisses of the Lhasa block basement and adjacent metasedimentary marbles and schists (as shown by Ding et al., 2001). These metasedimentary rocks are also cut by the undeformed 21–25 Ma granites.

Brittle Faulting Elsewhere on the Boundaries of the Namche Barwa Antiform and Massif Northeastern and Southeastern Boundary

Foliation surfaces with normal-sense north-down-slickensides were noted in outcrops near the Rong Chu–Po Tsangpo confluence and in some other outcrops along the Rong Chu valley as far as Dongjiu. This sense of displacement would accommodate rise of the massif, and this location is along strike from the zone of intense shallow seismicity (see following). Geng et al. (2006) reported brittle faulting ~1 km downstream from the Rong Chu–Po Tsangpo confluence. Because we were not able to go along the Po Tsangpo toward the main Yarlung Tsangpo confluence, we have no surface information about the occurrence of brittle faults in bedrock in that section to correspond with our seismic results (see following). It is curious that Thematic Mapper satellite imagery (Fig. 5) shows some prominent lineaments in the southeastern boundary zone of the Namche Barwa antiform (the source for the faults shown in Fig. 3), some of which show small apparent right-lateral offsets of strongly incised streams, but similar features are not prominent along the northeastern margin of the Namche Barwa massif, where the seismic results show a linear swarm of earthquakes. Given the faults observed in the Deu Gungbu section on the western side of the massif, it seems likely that the probable faults observed on the satellite images on the southeast side of the antiform also have a significant antiform-side-up component of displacement.

Northwestern Boundary

Topographic features suggestive of recent faulting in and subparallel with the east-northeast–trending Yarlung Tsangpo valley occur in the area approximately between Lusha and Milin, although the mild and discontinuous nature of these geomorphic features suggests that the significance of this faulting is small. Slickensides in the granitoid rocks of the Gangdese batholith near these features and farther north near Nyinchi hint that a component of left-lateral strike slip could be involved. There is a prominent straight lineament (probably fault controlled) seen on satellite imagery southwest of Milin that projects northeast directly into and along the course of the Yarlung Tsangpo near Milin. Outcrops of Tethyan metasedimentary rocks showing extensive brittle fracturing and pervasive retrograde low-temperature alteration occur on the south bank of the Yarlung Tsangpo valley opposite the Nyang River confluence, but these features are covered by river terrace gravels and it is unclear whether they are related to active faulting. The structural geometric relationships of the Tethyan Himalayan metasediments relative to the gneisses of the Shioka shear zone from near Milin northeast to near Lusha and Nuxia hint that there may be a northwest-down (probably normal) fault between the two lithotectonic units. This fault relationship is required by outcrop and topography in the north-south–trending side valley southwest of Milin (Fig. 3). However, along the main Yarlung Tsangpo valley such a fault is only a possibility, and one has not been included in this area on the map and cross section because it is not absolutely required by structural geometry. Also, while no exposure of the contact was found along this valley, outcrops nearby showed no atypical fracture or fault abundance, and no geomorphic feature was observed suggesting an active young fault at this position.

Ductile Shear Zone in the Southeastern Antiform

Thematic Mapper satellite images (Fig. 5) show a distinctive zone of parallel microlineated terrain in the southeastern part of the Namche Barwa antiform, within the area mapped as sub-Tethyan granitoid gneisses (rocks of the core of the antiform). Geng et al. (2006) reported an extensive zone of mylonites corresponding to this feature. A few samples were collected in this zone by colleagues at the Chengdu Institute, before our project began, in the valley leading down from Doshong-la to the Yarlung Tsangpo at Medog. From inspection of thin sections, these are mylonitic granitoid and quartzose metasedimentary gneisses. We think, based on these data, that there is likely to be a wide, significant mylonitic shear zone at the southeastern side of the Namche Barwa antiform (shown in Fig. 3). Notes taken in the field by Liu Yuping (2006, personal commun.) show that the gneisses have a subhorizontal stretching lineation and that the foliation dips moderately steeply southeast. The sense of shear is not known. Given what we found at the northwestern side of the antiform in this position, we think this is most likely to be the equivalent of the Shioka shear zone described in the preceding, separating gneisses below from Tethyan metasediments above and with originally top-to-the-north normal sense shear, reoriented here on the southeast limb of the Namche Barwa antiform, although it might be in part or largely of older, early Himalayan thrust origin.

Overall Faulting and/or Shear Zone Contribution to the Large-Scale Structure

Of the brittle faults we infer or have mapped, including the one we found on the western margin of the massif, none completely excises the traceable map units of the mafic and/or ophiolitic Yarlung Tsangpo suture and the adjacent Tethyan Himalayan metasedimentary schists and gneisses, and are therefore likely to have only moderate total thrust displacements (e.g., Fig. 7, section B). We agree with the conclusion of Burg et al. (1997,

1998) that the antiformal structure must have been the major contributor to the rise of the rocks in the Namche Barwa antiform. While there is a significant ductile and brittle thrust zone in the Nam-la–Rong Chu structure, the geometry of the northern end of the Namche Barwa antiform and massif shows that it has substantial structural relief induced by large-scale folding. From the width of the structure, and the metamorphic conditions associated with the Doshong-la migmatites in the early stages of the Nam-la thrust zone (Booth et al., 2004, 2009), a minimum depth for a detachment surface for this fold and thrust zone is ~25 km. The rocks of the massif have undergone significant and pervasive ductile strain of undetermined amounts during its development, and there is consequently no significant constraint provided for the maximum depth of detachment from the structural and map data. Our observations reveal no evidence of large, significant strike-slip faults on the margins of the massif or the antiform, although there may be modest components of such displacement accompanying the dominant thrust faulting. Earlier ductile fabrics with currently subhorizontal stretching lineation in places on the margins of the massif and the antiform are reoriented by the antiformal structure from initially thrust- and normal-sense shear on broadly north-dipping early Himalayan ductile shear zones.

Seismicity

As part of the larger Geodynamics of Indentor Corners project (http://www.ees.lehigh.edu/groups/corners/index.shtml), a regional temporary array (Fig. 1) of 50 broadband and 20 short-period seismometers recorded local, regional, and teleseismic events for a 16 month period (Eastern Syntaxis Seismic Experiment; Sol et al., 2007). Embedded within the array, the short-period sensors were deployed at denser station spacing around the western and northern margins of the metamorphic massif. Access to the interior of the massif and eastern margin was not possible. Here we report hypocenter locations for events within and close to the massif and antiform, in particular a remarkable dense swarm of seismicity that occurs at the northern edge of the Namche Barwa massif where the Yarlung Tsangpo makes its 180° bend in the Big Bend gorge.

Technical Details

Initial earthquake locations were determined using the Antelope software package (Boulder Real Time Technologies, Inc., 2008) with an automated trigging algorithm to pick both P-wave and S-wave arrivals. Preliminary locations were determined using a 1-D velocity model by associating a minimum of four detections to a 3-D traveltime grid. Initial locations were reviewed by visually inspecting waveforms, adjusting picks as needed, and relocating events in a 1-D, three-layer lithospheric velocity model appropriate for Tibet. Events were then relocated using tomoDD, a 3-D tomography code based on double-difference techniques (Waldhauser and Ellsworth, 2000; Zhang and Thurber, 2003). Events were first relocated in a regional velocity grid with 25 km node spacing. Using the locations from the 3-D regional velocity model as a starting point, local events were subsequently relocated in a 3-D velocity model using a 5 km node spacing centered within the massif. In total, 1254 events with magnitudes ranging from M_L 5.5 to <1.0 were found to occur in and around the Namche Barwa massif and antiform (Fig. 10).

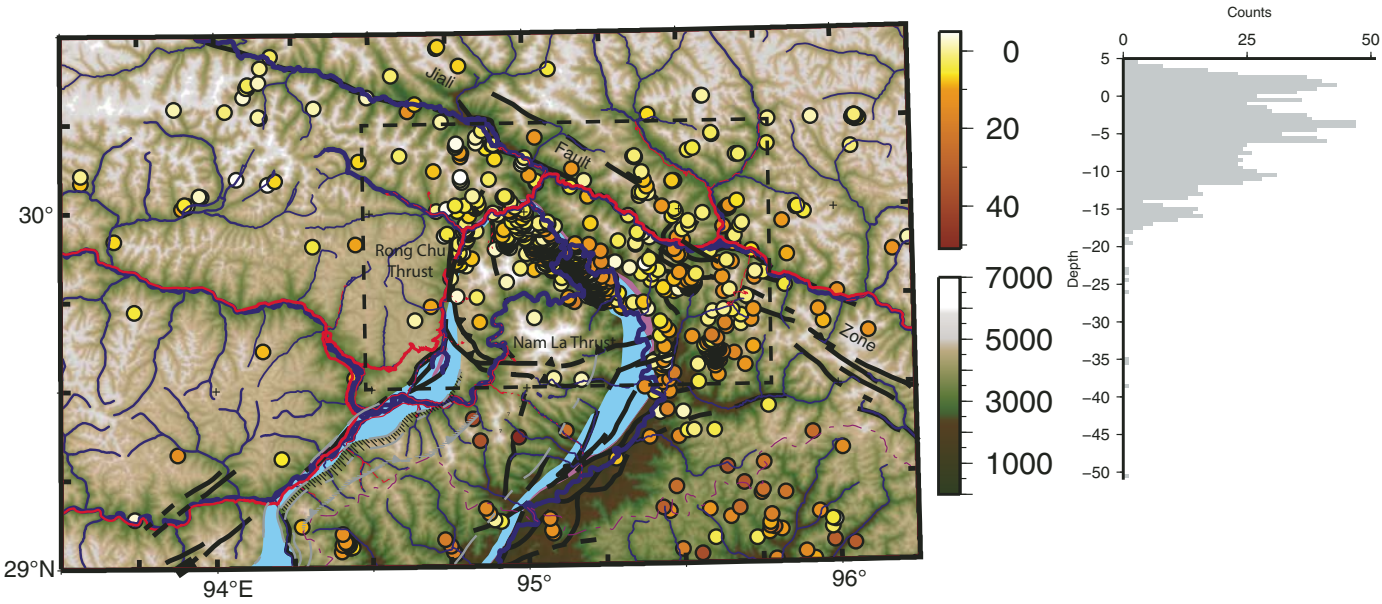

Figure 10. Seismicity in the study region recorded by the Eastern Syntaxis Seismic Experiment (Sol et al., 2007) located using hypoDD software (http://www.ldeo.columbia.edu/~felixw/hypoDD.html) (1254 events in a 16 month window). Epicenters in map view are color coded by depth (upper scale bar in km below sea level, bsl). Lower scale bar shows topographic elevations in meters. Structures, Tethyan metasediments, and suture zone rocks as in Figure 3. Histogram shows depth distribution of events plotted using 500 m bins. Dashed box is area shown in Figure 11.

Observations

Seismicity is limited to the upper 20 km of the crust (Fig. 10). The majority of events (79%) locate above 10 km depth (below sea level, bsl) with peaks at depth distributions of ~0 km (sea level) and 5 km depth (bsl). A quarter of the events (23%) have hypocentral depths above sea level. Only eight of 1254 events yielded hypocenters below 20 km depth (bsl). Focal mechanisms and moment tensor solutions are complex and show a blend of strike slip, normal faulting, and thrusting. Discussions of focal mechanism and moment tensor studies are beyond the scope here, and will be presented elsewhere.

A linear band of seismicity occurs along the mapped trace of the Rong Chu thrust on the west side of the massif. The events outline an active, steeply dipping fault with depth (Fig. 11). Most of the events locate above 5 km depth (bsl); a few events occur as deep as 8 km depth (bsl). Seismicity terminates to the north coincident with the northernmost mapped surface exposure of the thrust. Seismicity also terminates to the south where the Rong Chu thrust begins to turn to the southeast. The Nam-la thrust within the massif is virtually aseismic.

Events are broadly distributed within the region mapped as the Jiali fault zone (Fig. 10). While events do not sharply define a linear active fault trace, more events locate along the southern boundary of the fault zone where it partially coincides with the course of the Yigrong Tsangpo west of Tungmai. A small cluster of events is visible in the vicinity of Yigrong Lake, the site of a massive landslide and subsequent outburst flood in 2000 (Evans and Delaney, 2011). East of Tungmai and south of the Po Tsangpo, a M_w 5.0 event and associated aftershocks occurred at 11 km depth (bsl) on a southern splay of the Jiali fault during the recording window (Fig. 10). The largest event recorded during the deployment (M_w 5.5) occurred east of the massif at 18 km depth (bsl). Aftershocks illuminate a steeply dipping fault plane. Both this event and the M_w 5.0 event on the southern splay of the Jiali fault occurred within the Lhasa block basement north and east of the Namche Barwa–Gyala Peri massif.

The northeastern edge of the Namche Barwa–Gyala Peri massif is marked by a remarkable nest of seismicity. More than half of the 1254 events shown in Figure 10 occurred within this nest. The majority of these events are located along the northeast flank of a ridge that is within the 180° Big Bend of the Yarlung Tsangpo (Fig. 12) along a section of the river that constitutes a major portion of the Namche Barwa knickzone. Earthquake hypocenters define a nearly vertical zone of brittle deformation over a wide depth range beneath the ridge, from very shallow near-surface events to depths of 16 km bsl (Fig. 11; see also Fig. 19). Hypocenters cluster around two depth distributions, one just below sea level, and one from 7 to 10.5 km depth (bsl). While seismicity beneath the ridge occurred throughout the recording window, ~100 events are associated with an earthquake swarm that occurred over a two-day period. Seismicity terminates abruptly to the southeast where a drainage has developed off the northeast flank of the Namche Barwa massif. The nest of seismicity continues northwest of the ridge, crossing the Yarlung Tsangpo, and into the northeast margin of the Namche Barwa massif on the southwest side of the Po Tsangpo. The lower depth limit of seismicity shallows to the northwest. A few events occur within 5–10 km depth (bsl), but the majority of events occur above 5 km (bsl) (Fig. 11).

A small cluster of shallow seismicity (limited to above 5 km [bsl]) occurs directly beneath the higher topography to the northwest of Gyala Peri peak.

Relationship of Seismicity to Geology and Structures

Within and around the Namche Barwa massif, seismicity is limited in depth to above 10 km depth (bsl); the majority of events occur above 5 km depth (bsl), implying a relatively shallow brittle to plastic transition consistent with high geothermal gradients. The notable exceptions to this are events within the Lhasa block and events associated with the seismically active ridge on the northeast margin of the Namche Barwa massif, where seismicity extends to 15–16 km depth (bsl). Concentrated zones of seismicity seem to correlate with narrow bands of steeply dipping medium- to high-grade Tethyan Himalayan metasediments and amphibolite mylonites associated with exhumed suture zone rocks. Even the small cluster of seismicity beneath the high topography of the Gyala Peri massif seems to occur in the vicinity of a basement fold incorporating Himalayan metasediments. There is little seismicity where the bands of Tethyan metasediments are broad (and less steeply dipping?). The Nam-La thrust appears to be virtually aseismic, from which we infer (1) it is no longer an active structure, (2) it is locked and accumulating strain, or (3) it is creeping aseismically due to an elevated geothermal gradient.

To some extent concentrated zones of seismicity also seem to correlate with rivers, especially parts of the Rong Chu, Yigrong, and Po Tsangpo within the Lhasa block adjacent to the massif, and the Yarlung Tsangpo on the northeast margin of the massif. The remarkable clustering of seismicity on the northeast margin of the massif corresponds to the area of maximum stream power (Fig. 12; Finnegan et al., 2008; Larsen and Montgomery, 2012).

While our array only recorded data for a 16 month window, our observations are broadly consistent with longer term observations from regional networks (Liu Yuping, 2006, personal commun.). The dense station spacing of the temporary array provides a level of detail not possible from existing network data, detail that sheds light on both geodynamic processes and potential geologic hazards.

Metamorphic Geochronology

We report new zircon U-Pb ion-probe data from eight samples from north of Gyala Peri peak and seven samples from west of Namche Barwa peak. These complement zircon U-Pb data previously reported for the region by Ding et al. (2001), Booth et al. (2004), Guo et al. (2012), Su et al. (2012), Xu et al. (2010, 2012), Zeng et al. (2012), and Zhang et al. (2012). Samples from Namche Barwa were taken from outcrop, but all except one of those taken from Gyala Peri were collected as float from two locations on the Layo glacier (Fig. 2), owing to limited field time

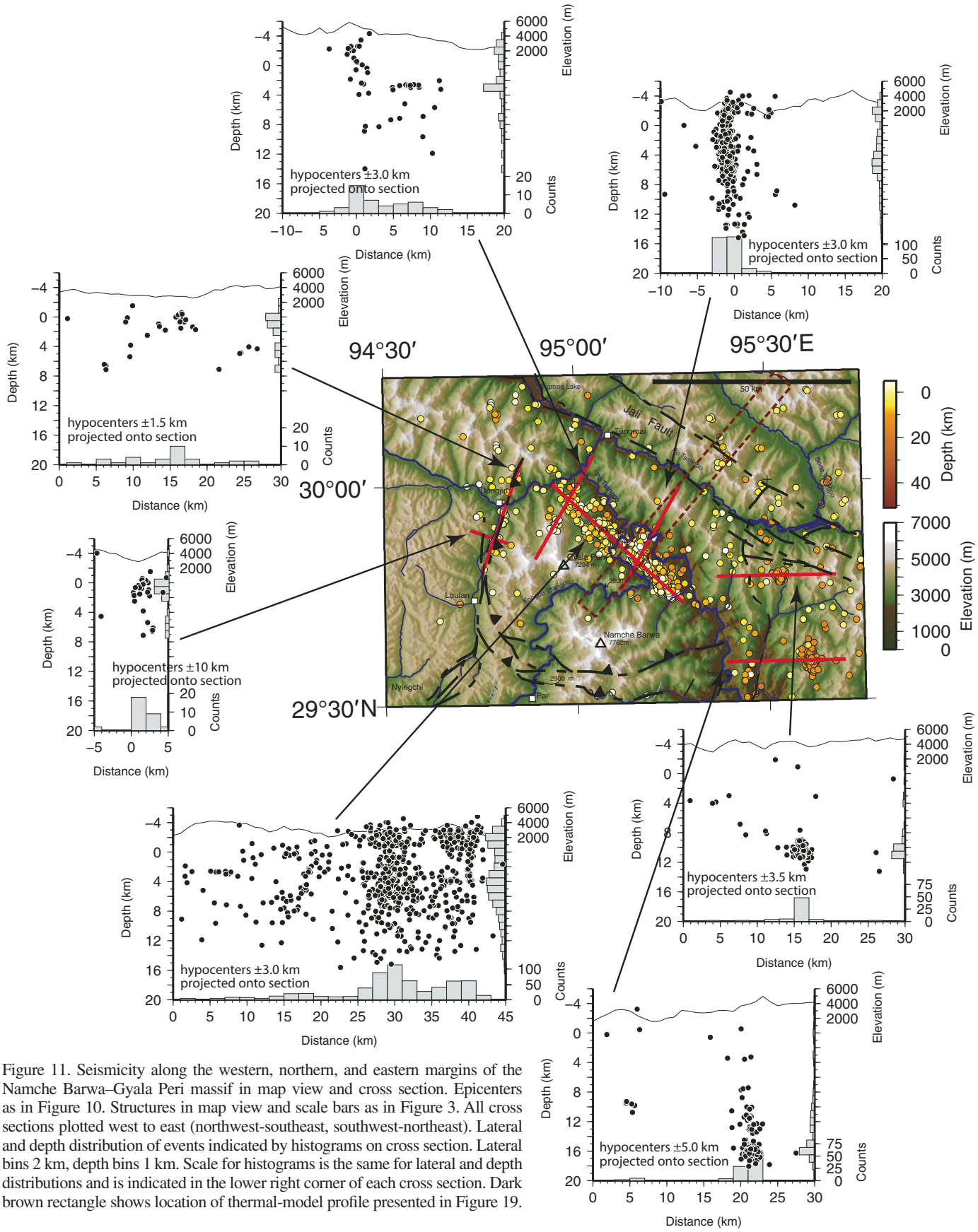

Figure 11. Seismicity along the western, northern, and eastern margins of the Namche Barwa–Gyala Peri massif in map view and cross section. Epicenters as in Figure 10. Structures in map view and scale bars as in Figure 3. All cross sections plotted west to east (northwest-southeast, southwest-northeast). Lateral and depth distribution of events indicated by histograms on cross section. Lateral bins 2 km, depth bins 1 km. Scale for histograms is the same for lateral and depth distributions and is indicated in the lower right corner of each cross section. Dark brown rectangle shows location of thermal-model profile presented in Figure 19.

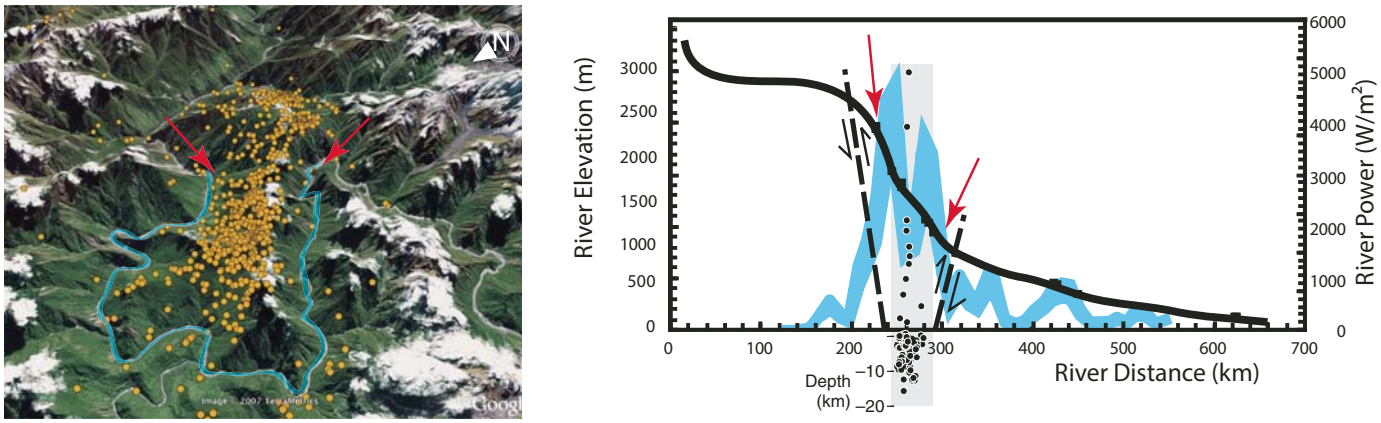

Figure 12. Oblique view to the southeast of the seismically active ridge and Yarlung Tsangpo Big Bend on the northern edge of the Namche Barwa–Gyala Peri massif (left) (source: Northern Margin Namche Barwa Massif, Google Earth, 2007). Distance across massif, between arrows, is 6 km. The ridge is in the Big Bend of the Yarlung Tsangpo. Long profile and mean river power (after Finnegan et al., 2008) with hypocenters beneath the ridge projected onto the long profile between red arrows (right). Note scale difference between events above and below sea level. Events plotting above the elevation of the long profile are a function of local relief. Events cluster on the northeast flank of the ridge and colocate with a major portion of the Big Bend knickzone. Zone of maximum river power (right) is highlighted in oblique view (left) in blue.

and difficult weather and terrain. Despite the obvious drawback of losing location information and outcrop context, sampling glacial float in this difficult terrain provides a more comprehensive picture of the bedrock age relationships present in the watershed. The possible source area for the float samples is limited to the ~90 km^2 of the Layo catchment on the north flank of Gyala Peri peak (Fig. 2). The samples were from a range of igneous and basement units showing varying degrees of anatexis and migmatization; Table 1 and Figure 13 provide sample information and summary U-Pb results; complete analytical data and methods can be found in supplemental Table DR1 (see footnote 1). Although we examined zircon cores and grain interiors, our main focus was on those rims and overgrowths that recorded the most recent overprint, so our data should not be viewed as a representative sampling of all components in all zircons.

Combining our new data with the many recently published results (Table DR2), we separated samples into those obtained from basement gneisses from the Namche Barwa massif, and those from either the Tethyan cover or presumed Lhasa block and Nyingchi Complex rocks from outside the interior of the massif. Depicting our data using cumulative probability distributions, Figure 13 clearly shows that zircon spot analyses from the Namche Barwa massif and in particular from our Gyala Peri samples define a discrete set of subpopulations 10 Ma or younger. We see little or no evidence of Gangdese batholith ages (ca. 30–150 Ma) in samples from the massif, either as xenocrysts or primary grains, nor do we see evidence of any overgrowths giving ages in the interval 50–150 Ma, suggesting that the precursors to the young melts are likely local basement rocks. In contrast, samples from the Tethyan cover and Lhasa block–Nyingchi Complex return

TABLE 1. SUMMARY OF U-Pb DATA

Sample	Elevation (m)	Longitude (E)	Latitude (N)	$^{206}Pb/^{238}U$ zircon ages: main components (Ma)*	Rock type
GP-10-03	3600	94° 53.036′	29° 55.409′	1.0–11, ~1450	leucogranite with possible cordierite (float)
GP-12-03	3600	94° 53.036′	29° 55.409′	1.5–7	granite pegmatite (float)
GP-15-03	3600	94° 53.036′	29° 55.409′	2.3–10, >380	tourmaline-bearing aplite (float)
GP-09-03	3610	94° 53.755′	29° 54.650′	3.0–8, 500–800, ~1500, 1750	granitic gneiss
GP-02-03	3618	94° 53.455′	29° 54.517′	0.8–8, 300–900+, ~1450	granite pegmatite (float)
GP-04-03	3618	94° 53.455′	29° 54.517′	2.2–5.3, 500–700, ~1500, 1750	massive granite (float)
GP-06-03	3618	94° 53.455′	29° 54.517′	1.7–8, 12, ~300, 1150, ~1500	granite pegmatite (float)
GP-07-03	3618	94° 53.455′	29° 54.517′	5.7–6.7, ~1150	granite pegmatite (float)
b-279	1530	95° 8.803′	29° 53.408′	~400–500, ~700, ~1100	quartzite
b-265	1470	95° 17.850′	29° 46.700′	300–750, ~1000	micaceous quartzite
b-254	3598	95° 12.510′	29° 45.980′	480–530	quartz diorite
b-232	2713	94° 57.594′	29° 45.280′	7, 9, 12, 15, 19, 20–24, ~500	garnet-biotite-plagioclase gneiss
b-261	3250	95° 13.576′	29° 45.137′	270–550, ~1650–1750	granitic gneiss
b-115	1900	95° 24.825′	29° 33.825′	17–31, ~50, ~1200	leucocratic gneiss
b-35	1059	95° 20.713′	29° 19.197′	49–53	diorite (Gangdese)

Note: Samples are arranged in north to south sequence. GP series samples were analyzed with a focus on young anatectic event; b series samples were analyzed with a focus on protolith ages.

*Analytical data are in Table DR1; > indicates older than; ~ indicates ca.

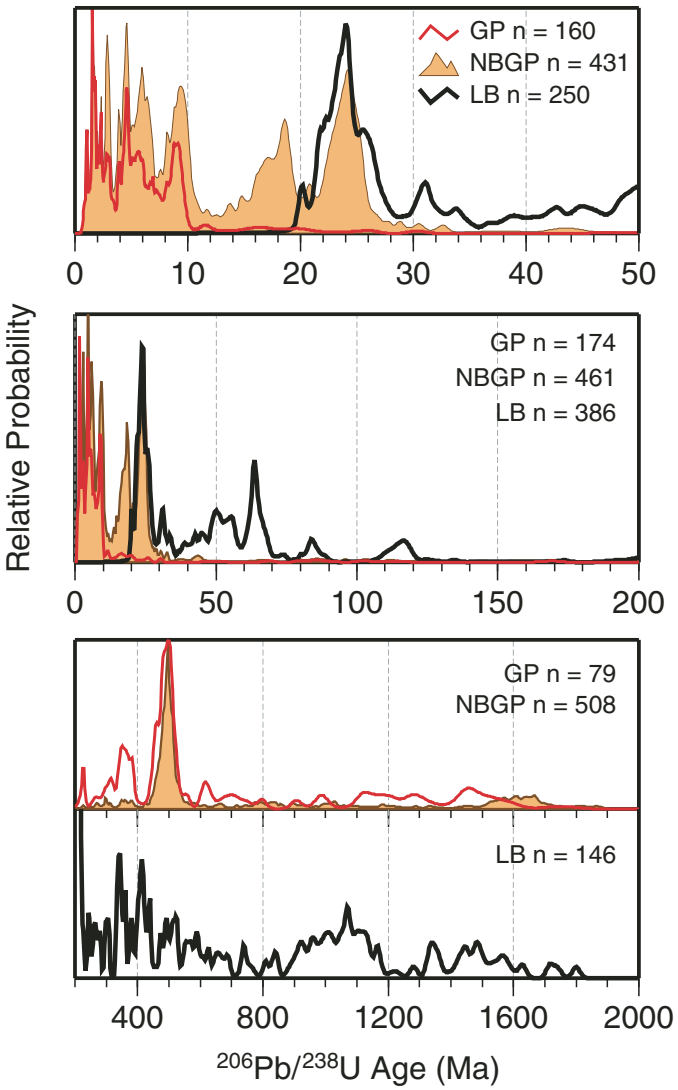

Figure 13. Zircon $^{206}Pb/^{238}U$ dating results for the Namche Barwa (NB; GP—Gyala Peri massif) massif and surrounding Lhasa block (LB) shown as cumulative probability-density age spectra. Data are from this paper (Tables DR1, DR2; see footnote 1), Ding et al. (2001), Guo et al. (2012), Su et al. (2012), Xu et al. (2010, 2012), Zeng et al. (2012), and Zhang et al. (2012). Spectra were rescaled to the maximum value in each data set; peak height differences between data sets are not significant. Note also that relative abundances reflect sampling distribution (many samples come from a relatively small area near Namche Barwa peak, southeast of the Yarlung Tsangpo) and also analyst emphasis on zircon cores, rims, or other textures. Red—data from this paper and Booth et al. (2004) for the Gyala Peri massif; filled orange—data from this paper and numerous references, for entire Namche Barwa massif including Gyala Peri; black—data from immediate surroundings of Namche Barwa structure, including Nyingchi Complex rocks of the Lhasa block and Namche Barwa Tethyan cover.

ages no younger than ca. 20 Ma. Both groupings of samples share a strong signal ca. 20–25 Ma, although this signal might be a coincidence because it is based on ages from both crosscutting pegmatites in the Jiali fault zone and high-pressure melts sampled from high-pressure rocks of the interior of the Namche Barwa massif. In terms of abundance the strongest older signal from the massif are the Pan-African ages of ca. 500 Ma. However, it is important to keep in mind that in addition to the analytical bias introduced by the analytical goals of each study, there is also a significant sampling bias at Namche Barwa owing to the difficult and limited access: many of the results reported in the literature come from a small area at the foot of Namche Barwa peak, near the top of the large knickzone. Thus, our samples from Gyala Peri, although nonsystematically analyzed, significantly extend the zircon U-Pb coverage for the Namche Barwa massif. More work at Gyala Peri and other new localities is clearly called for.

In detail, the zircons from the Gyala Peri samples show remarkably complex patterns of growth and resorption (Fig. 14). A number of grains from several samples show evidence for relatively continuous zircon growth. Other grains show broader growth zones of homogeneous age, and a number of grains appear to show multiple episodes of discrete zircon growth, resorption, and then renewed growth. The oldest ages adjacent to zircon cores are close to 10 Ma. The youngest zircon U-Pb ages, from Gyala Peri, are 0.8–1.0 Ma, the same, remarkably, as a U-Th/He zircon age of 0.8 Ma and an Ar-Ar biotite age of 0.9 Ma from bedrock in the Layo valley (see following). Based on the very low Th/U ratios of 0.1 or lower seen in most analyses, we interpret these ages to date zircon growth in response to fluid infiltration and/or partial melting during decompression (e.g., Rubatto, 2002), over the period 10 Ma to the present.

Thermochronology

To identify patterns and rates of exhumation in and around the Namche Barwa antiform and place constraints on tectonic and landscape evolution in southeastern Tibet, we applied thermochronological methods to a number of samples. We report results from U-Th/He dating of apatite and zircon (69 and 74 dates, respectively), as well as $^{40}Ar/^{39}Ar$ dating of biotite (75 dates) and K-feldspar (1 sample). Table 2 provides sample locations and a summary of apatite, zircon, and biotite results (a provisional subset of these data were displayed without details by Stewart et al., 2008; Finnegan et al., 2008). Table DR3 provides information about samples, Tables DR4–DR6 provide analytical data and details for the mineral ages, and Table DR7 gives the K-feldspar step-heating results and inversion parameters. KML versions of these and related data from this paper are available from the GSA Data Repository (see footnote 1) to permit easy interactive viewing of age relationships between samples and relative to regional topography.

Samples

Our bedrock samples were collected either by our team or members of a difficult expedition to the interior of the Namche Barwa massif mounted by the Chengdu Institute of Geology and

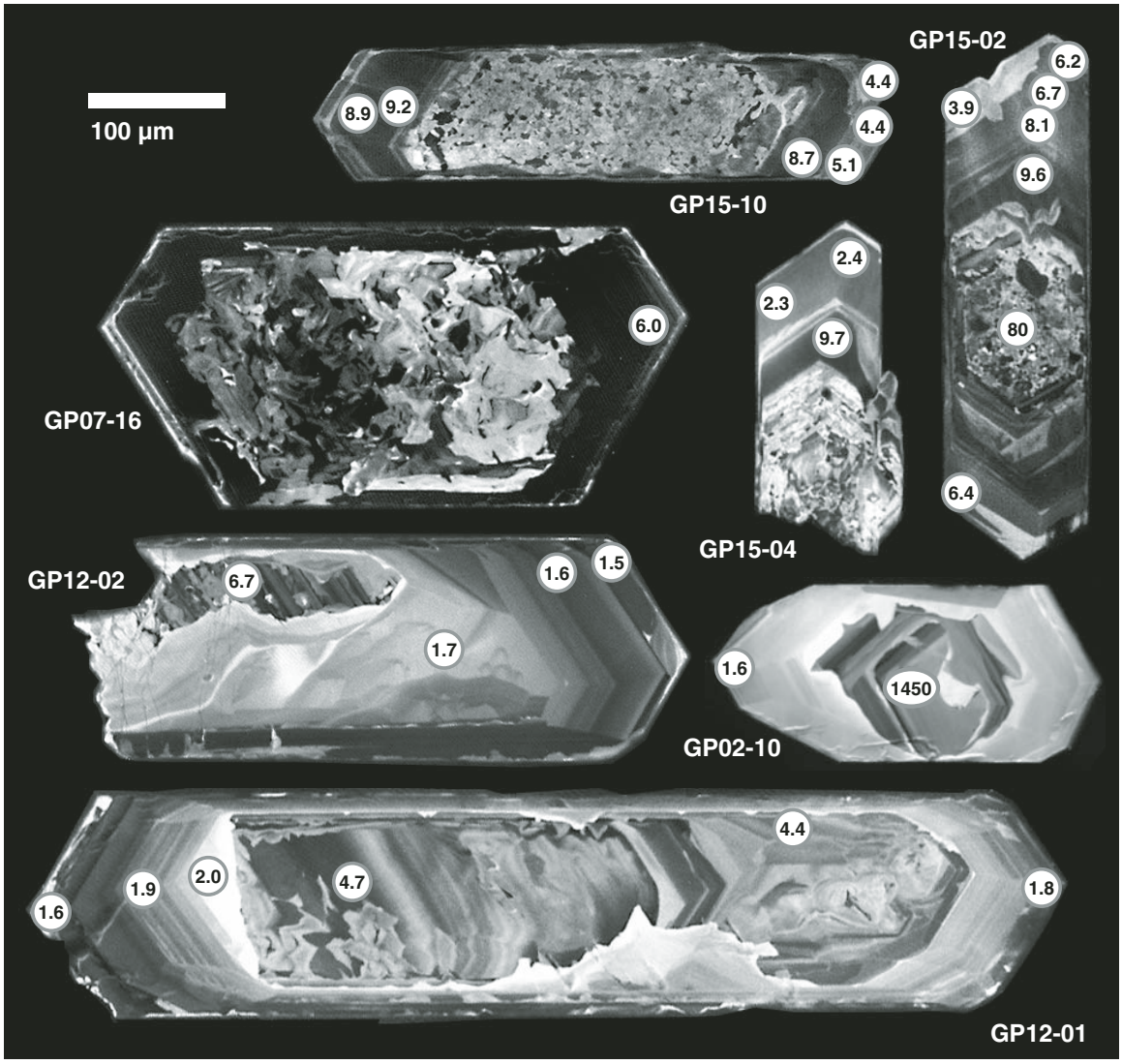

Figure 14. Cathodoluminescence images of zircons from anatectic rocks sampled in the Gyala Peri portion of the Namche Barwa massif. Images show ion probe $^{206}Pb/^{238}U$ age relationships in these zircons, as well as complex reaction and overgrowth textures. Darker areas are generally higher in U and usually very low in Th/U ratio. Data are from Table DR1 (see footnote 1). The age relationships and textures suggest periods of continuous zircon growth as well as discrete episodes, possibly following resorption of older material, all over a protracted period.

Mineral Resources. Note that the interior portions of the deep Yarlung Tsangpo gorge and the eastern portions of the Namche Barwa massif are one of the wildest places remaining on Earth, and are nearly inaccessible due to high rainfall, extremely steep slopes, and dense vegetation, so our sample density is understandably far lower there. Samples were located using hand-held GPS units, which proved adequate despite the steep terrain and high relief. Our reported sample elevations are primarily derived from a barometric altimeter built into the GPS unit, and checked against 1:100,000 Soviet topographic maps and DEMs derived from the Shuttle Radar Topography Mission (SRTM) data set. We estimate that most of the elevations have a precision of 30 m or better relative to one another. Information about sample location and rock type is given in Table DR3.

Methods

We used standard methods for sample preparation and U-Th/He analysis of apatite and zircon, and $^{40}Ar/^{39}Ar$ analysis of biotite and K-feldspar. For the multigrain, multialiquot U-Th/He analyses, we report pooled ages (Vermeesch, 2008) with an uncertainty derived from analytical errors only. For $^{40}Ar/^{39}Ar$ biotite and our few muscovite ages, we employed a mix of step-heating and total fusion analysis. Given that biotite age spectra are not particularly informative about thermal history, we summarized our data as follows. We report the inverse isochron age and uncertainty for well-behaved samples having low MSWD (mean square of weighted deviates) values of <2.5 and for slightly discordant samples that have MSWD between 2.5 and 10. For highly discordant samples where MSWD is >10

TABLE 2. SUMMARY OF MINERAL AGES

Sample	Elevation (m)	Longitude (E)	Latitude (N)	Apatite U-Th/He *n**	Apatite U-Th/He Age ± 2σ (Ma)		Zircon U-Th/He *n**	Zircon U-Th/He Age ± 2σ (Ma)†		Biotite $^{40}Ar/^{39}Ar$ Age ± 2σ (Ma)§		MSWD
CL-03-05	3761	96° 09.385′	30° 47.396′				2	32.9	2.3			
CL-04-05	3635	95° 35.777′	30° 46.977′				4	81.1	4.7			
CL-06-05	4208	94° 58.913′	30° 46.188′				5	46.7	2.7			
BM-06-05	4359	95° 45.040′	30° 21.042′	8	10.5	0.3	6	35.0	1.8			
BM-05-05	4194	95° 44.970′	30° 20.916′	3*	8.24	0.48						
BM-04-05	4059	95° 44.920′	30° 20.837′	7*	7.66	0.24						
BM-02-05	3762	95° 44.942′	30° 20.340′	6	8.53	0.26						
BM-03-05	3922	95° 44.940′	30° 20.340′	3*	8.05	0.46						
BM-07-05	3498	95° 44.890′	30° 20.010′	6	7.56	0.36						
NBK-41-23	3207	95° 46.199′	30° 14.447′	7	8.03	0.26						
BM-01-05	3054	95° 45.997′	30° 11.113′				4	10.4	0.5			
BT-34-02	2241	94° 56.643′	30° 10.181′				9	2.05	0.07			
BL-03-03	3432	93° 37.472′	30° 07.979′				2	13.1	0.7			
BT-35-02	2094	95° 01.734′	30° 07.675′							10.61	0.27	2.8
BT-08-03	2062	95° 03.558′	30° 05.628′							15.12	0.15	>100
BT-18-01	2109	95° 03.575′	30° 05.619′				4	0.35	0.01			
BT-05-03	2070	95° 02.964′	30° 04.301′							43.05	1.50	>100
BT-32-02	2200	95° 08.611′	30° 04.088′							14.86	0.18	58.7
BT-02-03	2019	95° 02.219′	30° 03.853′							3.75	0.17	TF
BT-01-03	2027	95° 01.935′	30° 03.431′							4.70	0.07	13.5
BT-09-03	2051	95° 01.715′	30° 02.659′							3.22	0.03	41.0
BT-01-02	1995	95° 00.656′	30° 02.330′							1.68	0.17	0.9
NBK-68-26	3068	94° 37.890′	30° 01.638′				2*	4.08	0.20			
BT-03-02	2069	94° 59.546′	30° 00.872′				3	0.56	0.02			
BT-24-02	2720	95° 18.119′	30° 00.053′				2	0.67	0.03	12.87	1.05	58.7
BT-05-02	2351	94° 54.298′	29° 59.999′							1.57	0.04	0.8
NB02-35	2720	94° 43.225′	29° 59.762′				2	1.73	0.08			
BT-14-03	2827	94° 40.084′	29° 59.725′							15.94	0.18	1.3
BT-36-02	3457	93° 06.526′	29° 58.383′	4	11.6	0.6						
BT-07-02	2485	94° 48.697′	29° 57.253′	6	1.68	0.06	4	1.47	0.04	11.77	0.20	0.9
BT-23-02	2600	95° 23.072′	29° 57.244′	12	0.64	0.02	2	1.46	0.09	13.73	0.25	0.1
b-289	1990	95° 5.345′	29° 56.751′				6	0.89	0.04	0.23	0.14	TF
NB-60-26	2634	95° 23.180′	29° 56.695′	11*	6.28	0.22						
BT-13-03	2624	94° 48.772′	29° 56.509′							20.39	0.65	TF
BT-16-01	2555	95° 24.002′	29° 56.259′							14.07	0.29	1.8
BT-12-03	2686	94° 48.912′	29° 55.895′							16.05	0.52	TF
BT-31-02	2702	95° 23.528′	29° 55.769′				2	2.89	0.10			
BT-29-02	2750	95° 23.520′	29° 55.756′				2	1.64	0.07			
BT-25-02	2952	95° 23.004′	29° 55.476′	4	0.74	0.04						
NB-61-26	2653	95° 25.174′	29° 55.457′	22	2.13	0.06						
GP-14-03	3600	94° 53.036′	29° 55.409′				2	0.83	0.03			
GP-09-03	3610	94° 53.755′	29° 54.650′				2	0.71	0.04	0.94	0.03	1.2
NB-59-26	2731	95° 37.001′	29° 54.353′	19	7.35	0.22	4	5.3	0.16			
NB-63-26	2637	95° 29.493′	29° 53.491′	20	3.25	0.1	4	2.26	0.09			
b-279	1530	95° 8.803′	29° 53.408′				6	0.22	0.01			
b-278	1530	95° 8.803′	29° 53.408′							0.44	0.54	TF
BT-22E-02	2736	95° 33.275′	29° 53.344′	12	0.41	0.02				15.83	0.25	1.3
BC-01-05	2695	95° 34.111′	29° 53.325′	15*	1.35	0.04	2	7.42	0.52			
NB-55-26	2774	95° 46.079′	29° 51.233′	23	2.01	0.06						
BT-17-02	3180	94° 45.988′	29° 50.206′				4	1.92	0.06	16.44	0.24	2.4
BT-15-02	3242	94° 46.184′	29° 50.144′							37.99	0.56	2.2
BT-12-02	3287	94° 46.290′	29° 50.086′				2	4.66	0.16	47.18	0.49	25.4
BT-20-02	3567	94° 47.200′	29° 49.656′				5	1.25	0.04	2.19	0.08	0.3
BT-19-02	3695	94° 47.549′	29° 49.416′							1.63	0.12	0.3w
b-188	3290	95° 24.300′	29° 48.850′				2	2.08	0.09	43.44	0.43	>100
BL-02-03	3995	94° 25.349′	29° 48.663′	7	6.36	0.26						
BR-01-05	4527	94° 24.862′	29° 48.649′	3*	8.52	0.44						
NB-58-26	2852	95° 50.075′	29° 48.613′	15*	2.98	0.1						
BM-02-02	3646	95° 41.857′	29° 48.556′				3	8.94	0.33	22.45	0.29	14.5
NB02-120	4080	94° 25.272′	29° 48.070′	3	10.1	0.6	2	13.9	0.3			
NB-56-26	2880	95° 46.069′	29° 47.099′	25	6.76	0.18						
BC-03-02	2968	95° 54.943′	29° 47.018′				2	12	1.4	44.08	1.47	>100
BT-12-01	3267	94° 44.794′	29° 46.914′							16.38	0.34	0.6
b-265	1470	95° 17.850′	29° 46.700′				5	0.56	0.03			
BM-05-02	4321	95° 41.297′	29° 46.135′	12	5.71	0.16						
b-254	3598	95° 12.510′	29° 45.980′				6	0.5	0.03	1.02	0.05	0.2
BM-03-02	4286	95° 41.111′	29° 45.886′				2	10.2	0.4			

(*Continued*)

TABLE 2. SUMMARY OF MINERAL AGES (*Continued*)

Sample	Elevation (m)	Longitude (E)	Latitude (N)	Apatite U-Th/He *n**	Apatite U-Th/He Age ± 2σ (Ma)		Zircon U-Th/He *n**	Zircon U-Th/He Age ± 2σ (Ma)†		Biotite $^{40}Ar/^{39}Ar$ Age ± 2σ (Ma)§		MSWD
BT-20-01	3110	94° 00.346′	29° 45.676′	4	18.1	0.8						
b-247	2748	95° 09.506′	29° 45.487′				8	0.72	0.02	3.43	0.09	3.1
b-232	2713	94° 57.594′	29° 45.280′				2	0.27	0.01	1.66	0.05	1.1
b-261	3250	95° 13.576′	29° 45.137′							1.75	0.04	2.2
BT-20E-02	3090	94° 11.051′	29° 45.132′	6*	9.07	0.28	2*	13.2	0.4	42.35	1.29	TF
NBK-83b-25	4157	94° 47.502′	29° 44.916′				7	1.28	0.04	2.83	0.12	TF
b-237	2767	95° 03.909′	29° 44.542′				6	0.38	0.01	1.77	0.06	0.5
NB-57-26	3076	96° 02.303′	29° 44.204′	22	4.55	0.12						
NB02-159	3380	94° 43.096′	29° 43.905′				2	5.31	0.16			
BR-03-05	3515	94° 23.775′	29° 43.339′	6	5.63	0.18						
BT-37-02	4146	92° 02.374′	29° 43.004′				1	39.3	1.5			
BS-01-05	3087	96° 01.196′	29° 42.545′	13*	2.8	0.08						
BL-01-03	3224	94° 23.322′	29° 41.407′	5	7.12	0.3	4	9.92	0.34			
BR-04-05	3154	94° 22.878′	29° 41.364′	11	8.78	0.24						
BC-03-05	4434	96° 43.685′	29° 40.722′	6	52.6	1.7	3	52.9	2.8			
IG-4	2818	94° 55.253′	29° 40.461′							1.92	0.21	TF
BT-03-05	4677	94° 36.077′	29° 38.741′	6	8.45	0.36	4	9.18	0.32			
IG-6b-01	2984	94° 55.607′	29° 37.914′				6	1.15	0.04			
BT-09-01	4179	94° 42.637′	29° 37.905′	4	3.95	0.2	2	5.63	0.26	17.14	0.21	6.5
BT-01-05	4667	94° 35.711′	29° 37.681′	6	7.59	0.32						
b-141	1990	95° 24.035′	29° 37.343′				4	0.57	0.06	25.58	0.28	30.3
BC-02-02	3440	96° 21.902′	29° 36.865′				2	25.9	1.1	107.90	0.53	23.1
BT-08-02	3811	94° 43.049′	29° 36.635′	4	8	0.36	2	4.45	0.17			
b-143	4100	95° 36.376′	29° 36.100′							17.80	0.29	0.5
IG-11-01	4309	94° 59.436′	29° 34.827′							2.12	0.07	1.7
BT-04-01	3028	94° 27.821′	29° 34.734′							18.50	0.38	1.4
IG-14b-01	3222	94° 54.488′	29° 34′							2.45	0.07	46.1
BT-02-05	3911	94° 34.529′	29° 33.979′	6	5.62	0.2	4	8.56	0.29			
BT-04-05	3523	94° 33.922′	29° 33.958′	6	5.6	0.24						
b-115	1900	95° 24.825′	29° 33.825′				7	1.06	0.04			
IG-15a-01	3113	94° 53.558′	29° 32.385′				2	1.33	0.04	2.45	0.06	0.4
BL-09-03	2954	94° 25.781′	29° 31.625′	6	8.64	0.36	1*	9.39	0.57	18.75	0.22	8.0
b-376	1021	95° 27.252′	29° 31.514′							15.57	0.24	2.6
BL-18-03	2988	94° 27.034′	29° 31.220′							18.09	0.46	2.3
BL-06-03	3877	94° 15.590′	29° 30.256′	2*	6.88	0.38	2	9.94	0.42			
BL-05-03	4258	94° 13.300′	29° 30.219′	6	7.41	0.34	3*	8.51	0.34	22.63	0.23	70.1
BL-07-03	3738	94° 16.511′	29° 30.193′	6	6.2	0.26	2	9.01	0.47			
NB-69-26	3759	94° 23.392′	29° 29.543′	15	7.86	0.24						
NB-70-26	3660	94° 23.270′	29° 29.540′	18	8.56	0.24						
BL-08-03	3285	94° 18.984′	29° 29.471′				1	8.49	0.5			
NB-71-26	3548	94° 23.165′	29° 29.456′	17	6.91	0.18						
NB-72-26	3453	94° 23.145′	29° 29.403′	17	7.51	0.22						
BT-21E-02	2940	94° 33.897′	29° 29.342′	4	4.66	0.22	2	5.49	0.27	20.92	0.72	TF
NB-73-26	3368	94° 23.100′	29° 29.297′	18	6.51	0.18						
NBK-36-23	2940	94° 49.846′	29° 29.291′	6	1.79	0.06						
NB-75-26	3198	94° 23.009′	29° 29.263′	22	7.37	0.24						
NB-74-26	3276	94° 23.003′	29° 29.262′	11	6.25	0.18						
IG-16-01	4227	94° 56.796′	29° 29.250′				4	1.48	0.06			
NBK-95-25	2938	94° 45.865′	29° 29.119′							4.40	0.12	2.9
IG-19-01	3057	94° 49.971′	29° 28.844′				2	2.48	0.09	4.12	0.10	0.2
b-39	3380	94° 58.752′	29° 28.511′							4.46	0.24	TF
BL-11-03	2977	94° 32.031′	29° 28.296′	6	5.78	0.18				12.76	3.02	TF
NBK-86-25	3137	94° 43.664′	29° 28.262′							3.64	0.09	1.4
IG-20b-01	3097	94° 45.763′	29° 28.099′				2	2.76	0.11			
BT-01-01	2931	94° 38.958′	29° 28.024′				5*	3.52	0.15	4.91	0.11	0.5
NBK-92-95	2937	94° 48.507′	29° 27.770′							3.1	0.08	0.6
BL-15-03	3024	94° 28.642′	29° 27.674′							18.25	0.18	>100
NB02-102	2960	94° 25.596′	29° 27.519′				2	6.92	0.39			
BL-13-03	2951	94° 30.201′	29° 27.279′							6.12	0.19	TF
b-45	905	95° 25.161′	29° 27.230′							35.85	1.01	5.3
NBK-15-23	3001	94° 41.488′	29° 26.358′							8.32	0.17	2.3
NB02-100	2940	94° 26.931′	29° 26.108′							24.03	0.50	>100
GS149	3250	94° 37.661′	29° 23.930′							5.39	0.08	0.3
NB-41-26	3777	94° 15.275′	29° 22.407′	24	6.88	0.24						
NB-40-26	3703	94° 15.769′	29° 22.288′	18	5.91	0.18	4	6.34	0.23			
NB-39-26	3632	94° 16.257′	29° 21.972′	9	5.8	0.18						
NB-38-26	3607	94° 16.499′	29° 21.910′	14	5.48	0.16						

(*Continued*)

TABLE 2. SUMMARY OF MINERAL AGES (*Continued*)

Sample	Elevation (m)	Longitude (E)	Latitude (N)	Apatite U-Th/He *n**	Apatite U-Th/He Age ± 2σ (Ma)		Zircon U-Th/He *n**	Zircon U-Th/He Age ± 2σ (Ma)†		Biotite $^{40}Ar/^{39}Ar$ Age ± 2σ (Ma)§		MSWD
NB-37-26	3547	94° 16.979′	29° 21.834′	3*	5.41	0.24						
NB-36-26	3295	94° 18.438′	29° 21.621′	20	5.77	0.16						
NB-35-26	3251	94° 18.779′	29° 21.516′	6*	6.19	0.26						
NBK-13-23	2964	94° 24.882′	29° 20.334′	9	4.22	0.14	4	5.67	0.22			
NBK-14-23	2964	94° 24.882′	29° 20.334′							14.19	0.23	20.9
NB-16-26	2974	94° 20.042′	29° 19.500′	4*	5.11	0.22						
b-35	1059	95° 20.713′	29° 19.197′				4	12.1	1.4			
NB-22-26	3016	94° 27.864′	29° 18.611′	15	3.7	0.12						
b-77	990	95° 10.590′	29° 18.540′							20.82	0.69	4.5
NB-26-26	3274	94° 29.007′	29° 17.776′	17	3.8	0.12						
b-138	3760	94° 31.880′	29° 15.215′							5.89	0.10	0.6
NBK-55-25	3980	94° 33.078′	29° 14.972′							5.85	0.18	0.8
NB-24-26	3629	94° 31.585′	29° 14.804′				4	5.96	0.25			
NBK-16-23	2974	94° 15.728′	29° 14.509′							8.97	0.49	4.8
NB-19-26	3100	94° 17.442′	29° 13.399′	17	5.31	0.16	4	5.96	0.24			
NBK-32-25	3363	94° 19.811′	29° 11.723′							8.35	0.24	4.0
NB-05-26	2978	94° 06.167′	29° 11.702′	39	6.94	0.24				89.76	2.7	TF
NB-01-26	2941	94° 11.024′	29° 11.384′	11*	8.11	0.48				9.26	0.37	TF
NB-07-26	3020	94° 03.274′	29° 11.376′	20	12.5	0.5				57.16	1.76	TF
NB-08-26	3068	93° 56.667′	29° 10.804′	29	7.16	0.26	4	8.78	0.34			
NBK-03-23	3223	94° 12.679′	29° 10.288′							9.57	0.198	1.9
NB-13-26	3173	94° 14.878′	29° 07.229′	4*	5.17	0.32	4	5.75	0.26	10.93	0.33	TF
NB-12-26	3132	94° 13.177′	29° 05.206′				3*	6.36	0.32			
NB-10-26	3102	94° 13.287′	29° 03.579′							9.80	0.32	TF
NB-11-26	3163	94° 14.120′	29° 02.699′				2*	6.45	0.33			
SB 13	584	94° 55.336′	29° 03.451′				2	9.74	1.13			
SB 10	482	94° 44.885′	28° 51.295′				2	5.34	0.62			
SB 02	464	95° 05.423′	28° 28.037′				2*	7.71	4.68			
Durango apatite, Fish Canyon zircon				48	32.01	0.26 SE	24	28.2	0.70 SE			
K-feldspar locations												
BT-33-02	2241	94° 56.643′	30° 10.181′									

Note: Samples are arranged in north to south sequence.

**n*—Number of replicates that contributed to pooled age; asterisk indicates that one or more replicates were omitted from pool. SE—standard error.

†Age calculated assuming no contribution from ^{147}Sm.

§Uncertainty includes uncertainty in J-factor.

For biotites with mean square of weighted deviates (MSWD) > 15, the reported age and uncertainty are based on total integrated gas release. If MSWD < 15, age and uncertainty are for inverse isochron. TF—total fusion analysis; w following value indicates that sample is white mica, not biotite.

we report just the total fusion age and multiply the calculated uncertainty by the value of MSWD. For total fusion analyses, we simply report the measured age and analytical uncertainty including the uncertainty in the J-factor.

Results

Context for thermochronological results. Mineral ages are measures of the integrated thermal history of their host rock (Harrison and Zeitler, 2005). Although the relationship between a mineral age and its thermal history can be complex, in a relatively quickly and likely monotonically cooled setting, as in southern Tibet, it can be helpful to start an interpretation of ages by treating them as simple cooling ages. At cooling rates of ~10 °C/m.y. for our typically analyzed grain sizes and compositions, helium diffusion in apatite closes at ~65 °C (Flowers et al., 2009), helium diffusion in zircon closes at ~195 °C (Reiners et al., 2004), and argon diffusion in biotite closes at ~300 °C (Grove and Harrison, 1996). Diffusion of argon in K-feldspars responds to the presence in each grain of multiple length scales for diffusion, with the net result that such samples showing multidiffusion-domain (MDD) behavior close to argon diffusion over a significant range of temperatures, sometimes as much as ~180–300 °C (Harrison et al., 2005). Given the consistent shape of the zircon grains we analyzed, anisotropic diffusion in zircon is not an important concern in our application (Reich et al., 2007; Cherniak et al., 2009), and radiation-damage effects on apatite kinetics will not be important given the young ages of our apatites and their relatively fast cooling rates (Flowers et al., 2009). As is commonly seen in comparing results from the Durango apatite and Fish Canyon zircon standards, our zircon replicate analyses show scatter beyond that expected from analytical errors. We attribute this to the much larger and more complex Th and U zoning seen in zircon compared to apatite (e.g., Fig. 14). Despite this internal scatter, the pooled ages we report show good consistency.

Spatial distribution. Most ages fall between 0.2 and 20 Ma; a few biotite ages are older. Generally, ages young toward the Namche Barwa massif, both regionally across terranes and along the axis of the Namche Barwa antiform toward the north (Figs. 1 and 15A–15C). In the few cases where samples were taken along vertical transects, apatite and zircon U-Th/He ages show

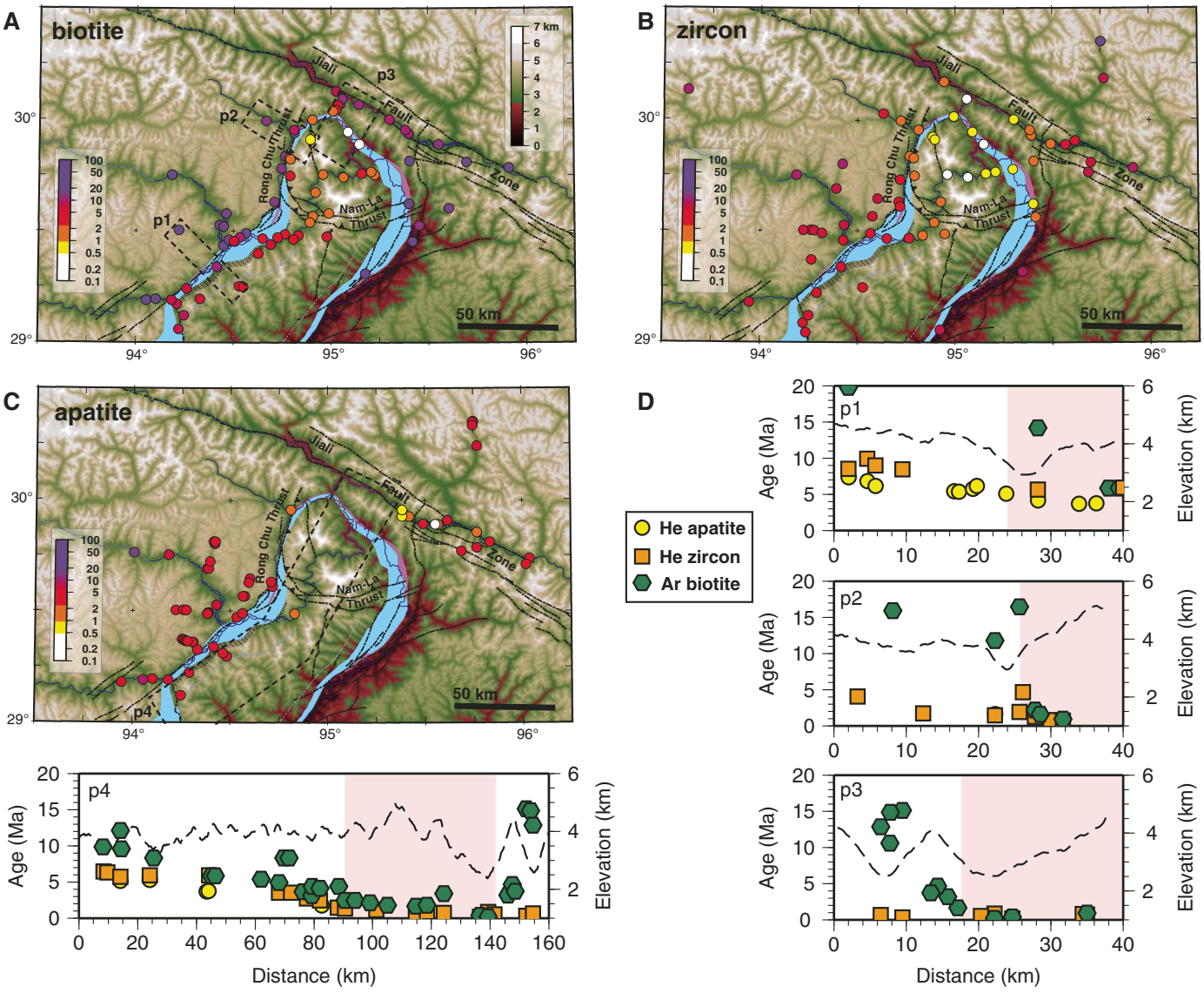

Figure 15. Maps and profiles showing cooling-age results for samples reported in Table 2. (A) $^{40}Ar/^{39}Ar$ biotite ages. (B) Zircon U-Th/He ages. (C) Apatite U-Th/He ages. (D) Cooling ages projected onto profiles p1–p4 (profile locations are shown in A and C). Interior of Namche Barwa massif or antiform shown in pink on profiles. Profiles p1–p3 extend from north and west into structure, whereas profile p4 extends from southwest to northeast along the axis of the structure. Green—biotite ages; orange—zircon ages; yellow—apatite ages. Dashed line shows mean topography in swath. Structural trends and geology are from Figure 3; blue is Tethyan cover sequence and purple is Yarlung Tsangpo suture zone.

no resolvable age-elevation trends outside analytical error (Fig. 16). In detail, apatite and zircon U-Th/He ages usually appear to vary relatively continuously, in contrast to $^{40}Ar/^{39}Ar$ biotite ages, which show sharp breaks along the southwestern, western, and northern margins of the antiform and massif (insufficient data are available from the difficult-to-access eastern portions of the structure, although the results we do have are consistent with this pattern). Our data overlay closely with the fission-track zircon and apatite dates reported by Seward and Burg (2008), consistent with the respective closure temperatures of these dating systems (~100 °C for apatite and ~250^{+} °C for zircon; Reiners and Brandon, 2006). Note that given the extremely young biotite and zircon ages we had measured within the massif, we did not measure apatite ages from this area, choosing instead to concentrate efforts elsewhere.

Biotite $^{40}Ar/^{39}Ar$ ages. The sharp discontinuities in biotite $^{40}Ar/^{39}Ar$ ages around the Namche Barwa massif correspond closely with observed fault zones and terrane boundaries (Figs. 15A, 15D). At one location in a brittle fault zone along the western margin of the massif (samples BT-12–02, BT-15–02) or in the case of sample BT-05–03 near an active hot spring just north of the massif, biotite ages are anomalously high, and we attribute this to incorporation of excess ^{40}Ar carried by shear zone fluids, possibly aided by shearing and recrystallization.

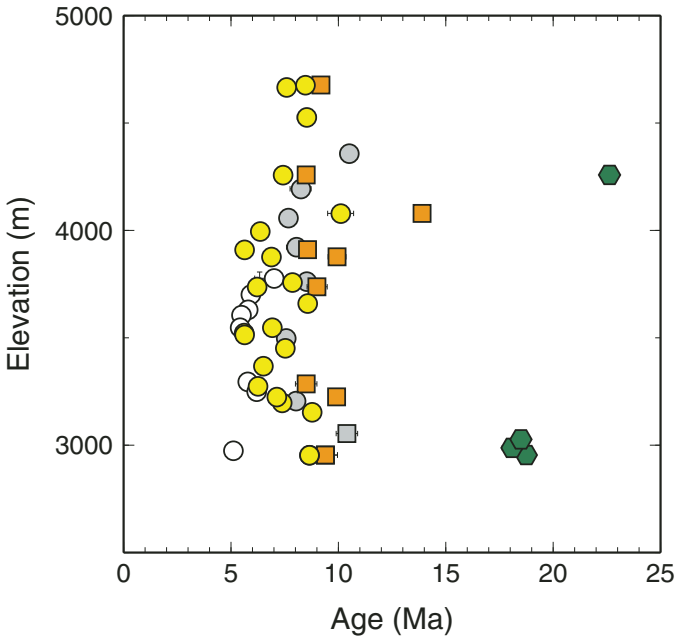

Figure 16. Age-elevation relationships for Lhasa block mineral ages. U-Th/He apatite—circles; U-Th/He zircon—squares; $^{40}Ar/^{39}Ar$ biotite—hexagons. Data from Lower Nyang River—yellow (apatite), orange (zircon), green (biotite). Also shown are data from a section facing the Yarlung Tsangpo, southwest of Bayi town (white) and from near Bomi, to the northeast of the Namche Barwa structure (gray).

Zircon and apatite U-Th/He ages. While overall distributed much like the biotite ages, a notable feature for these lower-temperature thermochronometers is that young ages are not just contained within the boundaries of the active Namche Barwa massif, but also occur outside the massif in immediately adjacent parts of the surrounding Lhasa block (this can also be seen in the fission-track data reported by Seward and Burg, 2008). Figure 15D shows ages projected onto transects across the margins of the massif. Note that apatite and especially zircon U-Th/He ages increase in all directions from the large Namche Barwa knick-zone, both upstream and downstream in the case of the zircon ages (Figs. 15B, 15C).

K-feldspar $^{40}Ar/^{39}Ar$ data. We report one K-feldspar $^{40}Ar/^{39}Ar$ step-heating result from sample BT-33–02. This sample was taken from an undeformed pegmatite near the Jiali shear zone, not far from the northern boundary of the Namche Barwa massif in a region where very young cooling ages are found outside the massif (see Fig. 2 for location). Results for MDD inversions for temperature history (Lovera et al., 1989; Zeitler, 2004; Harrison et al., 2005) are shown in Figures 17A–C and full details are available in Table DR7.

Cooling histories. Figure 18 compares cooling histories for various regions within and around the Namche Barwa antiform and massif. The figure assumes that in each of the selected areas cooling has been monotonic (i.e., there has been no reheating or prolonged residence under isothermal conditions), and the figure does not customize closure temperatures for each specific region and cooling rate, other than to acknowledge the very high cooling rates within the Namche Barwa massif (closure temperature depends modestly on cooling rate; see Harrison and Zeitler, 2005). The variation per order-of-magnitude change is ~25% for apatite U-Th/He and ~10% for U-Th/He zircon and $^{40}Ar/^{39}Ar$ biotite, corresponding to an absolute variation in temperature of ~15 °C for apatite, 25 °C for zircon, and 30 °C for biotite. We discuss these cooling histories in more detail in the context of specific questions, but make three main observations: (1) the very rapid and large-magnitude cooling within the Namche Barwa massif, (2) the rapid pulse of cooling seen between 5 and 10 Ma in both the antiform-proximal Lhasa block and the Namche Barwa antiform, and (3) the extremely sharp quenching seen in rocks just north of the Namche Barwa massif, along the Yigrong Tsangpo and Po Tsangpo valleys.

DISCUSSION OF RESULTS

We first discuss our data in the context of the topographic history of the southeastern Lhasa block and the tectonics and evolution of the Namche Barwa antiform and Namche Barwa massif. This discussion is followed by a synthesis of our observations and their application to landscape and tectonic evolution in southeast Tibet. We conclude with some comments about the broader implications of our work for general studies of orogenic processes and their preservation in the rock record.

Topographic History in the Southeastern Lhasa Block

Exhumation Pulse and Topographic Evolution

The Lhasa block surrounding the Namche Barwa structure to the west, northwest, and northeast underwent at least ~130 °C of rapid cooling over an interval of ~1–3 m.y., starting between ca. 8 and 10 Ma (Fig. 18A). This cooling would correspond to ~3–6 km of erosion at rates >1 mm/yr, assuming a range of shallow crustal geotherms between 20 and 40 °C/km. It is unlikely that higher geotherms were in effect because biotite ages of 15–25 Ma place a limit on the total amount and rate of earlier exhumation and thus thermal advection. Between ca. 20 and 10 Ma, ~100 °C of cooling took place at mean rates of only 10 °C/m.y., consistent with comparatively low exhumation rates of a few tenths of a millimeter per year. These exhumation rates would not have significantly perturbed the local geotherm. The rapid cooling pulse was confined to the easternmost portions of the Lhasa block, because at greater distances from the Namche Barwa antiform cooling ages increase significantly (Figs. 1 and 15) and supracrustal units like the Linzizong volcanics are preserved.

We believe that the evidence for this significant Neogene exhumational cooling pulse in the southeastern Lhasa block is robust. The steep age-elevation trend for both the apatite and in particular the zircon U-Th/He data provides additional evidence for the rapid exhumation pulse. The similarity of apatite ages at high and low elevations could also originate in part from the development of significant paleorelief and cooling through isotherms that had equilibrated to be subparallel to topography.

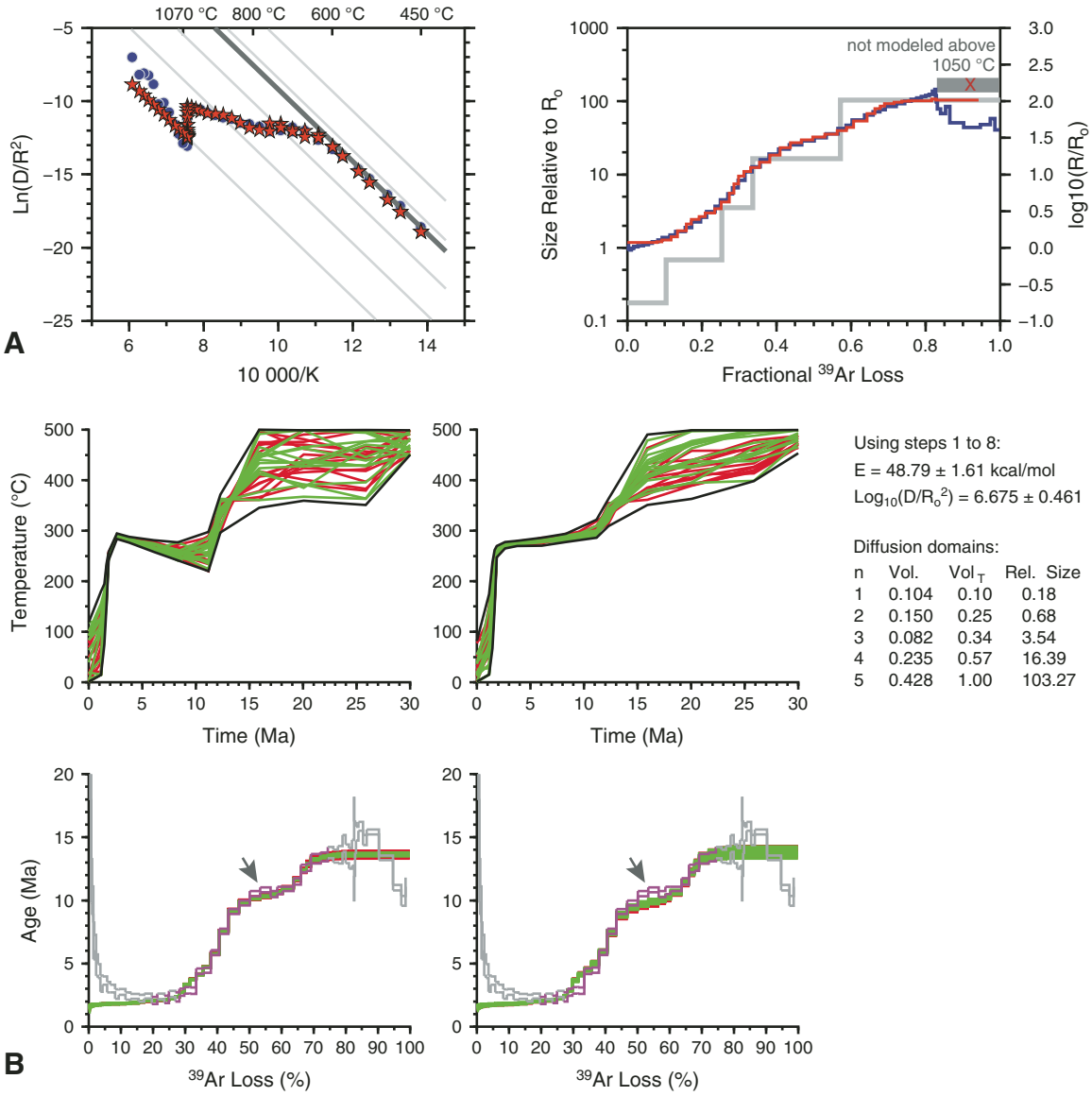

Figure 17. K-feldspar multidomain inversion models for thermal history (Lovera et al.,1989) based on $^{40}Ar/^{39}Ar$ age spectrum for sample BT-33–02. Inversions performed using the Arvert 4.1 controlled-random search code (Harrison et al., 2005; Zeitler, 2004). (A) Arrhenius and log(R/Ro) plots summarizing the diffusion-domain model used in inversion runs (obtained using modified code based on the domain-finding routine autoarr [Lovera et al., 1997]). Blue points and R/Ro spectrum—observed data. Red—model. Gray spectrum shows modeled diffusion-domain spectrum. Table on right gives kinetic and domain results. (B) Inverse model results. On both the temperature-history and age-spectrum plots, the green and red curves show, respectively, the 15 best-fit and 15 worst-fit models to the age spectrum, following model completion. On the thermal-history plots, the dark gray curves show the envelopes for the better fitting data (these envelopes are not solutions). For age spectrum, only the portion shown in violet was modeled. Left: heating at modest rates permitted. Right: only monotonic cooling permitted. Arrows show where in the age spectrum thermal histories that permit reheating lead to a noticeably better fit. For diffusion-domain distribution, Vol. gives volume fraction of domain; Rel. Size gives size relative to $R_o = 1$.

Slowing of Rates and New Local Base Level

Immediately following the rapid cooling pulse, currently exposed rocks in the eastern Lhasa block underwent a marked decrease in cooling rate. U-Th/He dates on apatite are 5–8 Ma, meaning that there has been only ~50 °C of cooling since that time (Fig. 18). Depending on the shallow geotherm, this would amount to 1–2 km of exhumation over this interval, a relatively slow rate given the 2 km of local relief and the transition to glacial climate that took place during this interval. This lowering of exhumation rates supports the suggestion that rock uplift

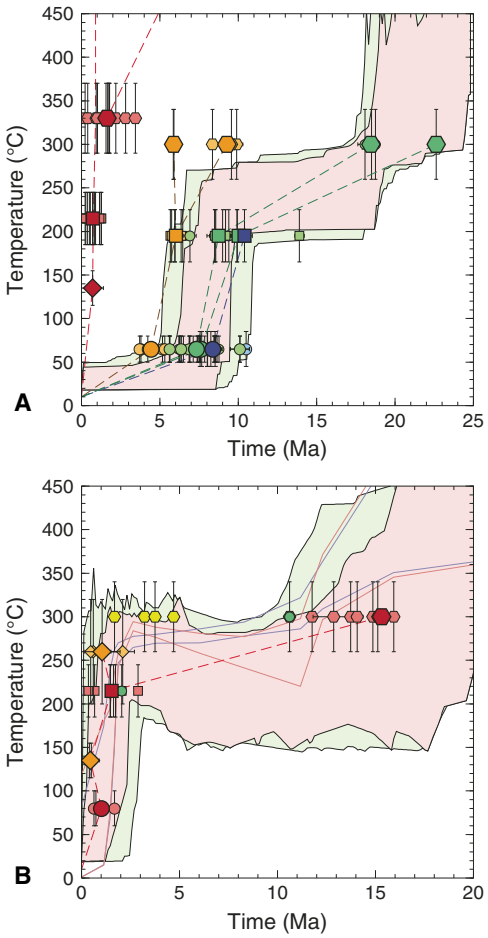

Figure 18. Temperature histories derived from mineral ages. Hexagons, squares, and circles show, respectively, biotite, zircon, and apatite ages; diamonds show fission-track zircon and apatites ages from Seward and Burg (2008). Larger, darker shaded symbols show the mean of the individual data from each region. The shaded regions show the acceptable fits (green) and good fits (pink) from a HeFTy inversion model (Ketcham, 2005), using the U-Th/He data and biotite kinetics summarized by Harrison and Zeitler (2005), adjusted for the spherical geometry used in HeFTy. Data are plotted against the nominal closure temperatures discussed in the text, under the assumption of monotonic cooling; the error bars reflect the uncertainties in kinetics for each system. (A) Data for the Namche Barwa massif (red), Namche Barwa antiform (south and north; orange), eastern Lhasa block along the lower Nyang River (above and below 3815 m, green), and Lhasa block near Bomi (blue). (B) Data for the Lhasa block proximal to the northern end of the Namche Barwa massif, along the Yigrong and Po Tsangpo. Symbols generally as in A, but orange points are fission-track data reported by Seward and Burg (2008), yellow circles are biotite ages from localities immediately adjacent to the Namche Barwa massif (not included in average), and data marked in green are from samples closest to BT-33–02 K-feldspar. Inversion results for this sample (see Fig. 17) are shown as envelopes around the best-fit solutions (red: heating permitted; blue: monotonic cooling only). Note that the K-feldspar inversion is based only on the sample's age spectrum, so the similar thermal histories derived from the mineral-age and multidiffusion-domain inversions are independent.

downstream of the area at the Namche Barwa massif has reset Tibetan base level to a higher local value (Zeitler et al., 2001a; Finnegan et al., 2008). Koons et al. (2013) showed that without stabilization by rock uplift at Namche Barwa, knickpoint propagation would migrate the Namche Barwa knickzone hundreds of kilometers in only 1 m.y.

We do not know river-channel paleoelevations, but currently the Yarlung Tsangpo in Tibet has a base level maintained by the massif at ~3000 m, even though the ultimate base level of the Tsangpo system is only ~150 m when it enters the Brahmaputra. The effect of this altered base level can be seen among other things in the deposition that occurs everywhere upstream from the Namche Barwa massif (Finnegan et al., 2008). If this is the case, then even though the massif is a relatively small feature, it has an important Tibet-wide impact in inhibiting headward cutting along the Yarlung Tsangpo and thus eventual erosional exhumation of the eastern Tibetan Plateau. Had it occurred, such exhumation would have been considerable and sufficient to affect the critical-wedge geodynamics of the eastern Himalaya.

Higher Elevation Surfaces

Many of the higher elevation landscapes in eastern Tibet occur as either preserved strath surfaces in the east, such as those studied by Clark et al. (2005), or farther west in the Lhasa block, accordant summit landscapes with modest degrees of local relief caused by cirque cutting. It is commonly assumed that these are relatively old surfaces, and certainly in the central and western Lhasa block preservation of upper crustal rocks like the Linzizong volcanics and older cooling ages support this assumption. However, in the easternmost parts of the Lhasa block, our cooling-age data show that these landscapes must be young, because they have U-Th/He apatite and zircon ages of much younger than 10–15 Ma and the same thermal histories as found in river valleys. This means that perhaps 5 km of material or more has been removed from these landscapes fairly recently, and all this material has been flushed from the system, requiring a significant and well-integrated drainage network to have existed. Also, while mean elevations in the eastern Lhasa block are slightly lower than at points to the west, the difference is small, meaning that the 4000–5000 m elevations are part of a landscape that is homogeneous in morphology but strongly diachronous in exhumation history. This is an argument that both solid Earth processes at depth and surface processes such as those proposed by Brozović et al. (1997) have maintained these elevations subsequent to the documented 8–10 Ma exhumation pulse.

Tectonics and Evolution of the Namche Barwa Antiform and Namche Barwa–Gyala Peri Massif

Structural and Tectonic Model for Namche Barwa

The scale and geometry of the Namche Barwa antiform probably required a substantial middle or lower-crustal ramp either in the active Main Himalayan thrust or a branch of this during the time of rapid exhumation of the antiform ca. 10–5 Ma

(Fig. DR2). Abandonment, by the main thrust zone undercutting this ramp, or of the entire branch, not later than 5 Ma under the antiform area southwest of the Namche Barwa massif would explain the cessation of rapid exhumation there. When this happened, we infer that the Nam-la thrust became active, or much more active, perhaps initially propagating up from the earlier ramp. It seems less clear whether the subsequent movement on the Nam-la thrust necessarily requires any link to a deep ramp structure, given the probable localization of massif boundaries by thermal weakening linked to rapid exhumation (i.e., the tectonic aneurysm model). The geomorphic expression of the Himalayan Main Boundary thrust changes quite abruptly just west of where the Siang River exits the foothills, with pediment incision of the bordering foothills east of this point. The implication is that the fault is not active (or is much less active) to the east and that its displacement must be transferred elsewhere farther north, and we suggest that some of this displacement has been relayed to the Namche Barwa massif and the Nam-la thrust. If this is the case, localization of tectonic aneurysm structures in the inner parts of the syntaxis could be connected to a mechanism that causes local inactivation of the shallow part of the main thrust detachment surface. Flexural distortions of the downgoing slab by changes in the lateral load (in the Eastern Himalaya, partial breakoff of the Indo-Burman slab) might be one such mechanism.

Namche Barwa Massif: Exhumation History, Longevity, and Exhumation Rates

The Namche Barwa massif has been an active and rapidly exhuming feature for the past 10 m.y. Its higher pressure metamorphic history requires an extended period of Cenozoic exhumation. U-Pb zircon ages from 10 to 1 Ma on decompression-melt phases from Gyala Peri (Fig. 13) and *P-T*-time data reported by Booth et al. (2009; Fig. 4) provide evidence of tens of kilometers of rapid decompression and exhumation over the past 5–10 m.y. Fluid-inclusion evidence for an exhumation-related steepening of the geotherm (Craw et al., 2005) and the very young ages of even higher temperature closure systems like biotite are consistent with such a persistent and long-term unroofing at rates of many kilometers per million years.

The rock exposures that host this assemblage of features, especially the young low-pressure anatexis, are distinctive and to our knowledge are sharply contained within the current boundaries of the massif. There is no age-progressive wake of anatectic rocks visible at the surface, or any adjacent loci of very rapid and extensive exhumation that would leave a clear geological signal. The Yarlung Tsangpo suture or correlative rocks and rocks of the Lhasa block are mapped as surrounding the massif on three sides (Geng et al., 2006; Fig. 3), consistent with persistent unroofing of the Indian crust from beneath the overthrust arc. Thus, despite the evidence for strong structural control of modern drainages near and within the massif, a nonuniform GPS field across the feature, and reports of some strike-slip motion along the massif boundaries, it appears that this feature has been more or less stationary with respect to its surroundings and in particular the rapid stream power associated with the Namche Barwa knickpoint (Finnegan et al., 2008; Koons et al., 2013).

Our young cooling ages are consistent with the rapid exhumation rates suggested by the petrological data, but deriving exhumation rates from thermochronological data can be perilous. Given a thermal history, determination of exhumation rates requires knowledge about transient boundary conditions, initial conditions, and crustal parameters that are often not well known, and for very low temperature systems, the impact of topography on thermal structure becomes important (e.g., Braun, 2002). This situation is particularly difficult in a setting such as southeastern Tibet, where there are clearly very active tectonics, a complex 3-D strain field, and extreme relief. It is beyond the scope of this paper to deploy fully 3-D models such as those developed by Herman et al. (2010), but we can use simple 1-D models to get an estimate of the magnitude of rates that must be in play.

Reiners and Brandon (2006) provided a clear discussion and means of estimating exhumation rates given an assumption that rock uplift and erosion are in steady state. For the Namche Barwa massif, we steer clear of the lowest-temperature systems (apatite U-Th/He and fission track) because of the degree to which 3-D topography and meteoric fluid flow would perturb the shallow thermal structure. From the very center of the metamorphic massif, where Seward and Burg (2008) reported a fission-track zircon age of only 0.2 Ma, we measured a number of zircon U-Th/He ages younger than 1 Ma, averaging ca. 0.5 Ma with ages as low as 0.2 and 0.3 Ma, and we found two $^{40}Ar/^{39}Ar$ biotite ages in the same area as low as 0.2 and 0.4 Ma as well as several other values of 1 Ma or less. With the crustal parameters used by Reiners and Brandon (2006), such mineral ages correspond to steady-state exhumation rates of 7 to >10 mm/yr, integrating over several hundred thousand to a million years. These rates would change slightly using different assumptions about crustal parameters, but the first-order results would not.

This simple estimate compares closely to the 10 mm/yr modern incision or erosion rate reported in Enkelmann et al. (2011) and the 5 mm/yr or more petrologically based estimate of unroofing that integrates over 5 m.y. or more (Booth et al., 2009). Note that this long-term estimate supports the use of a steady-state approach for the cooling-age data because the geotherm would have had time to readjust to rapid advection. At face value it would appear that rock uplift, roughly balanced by erosion, has been underway at rates of 5–10 mm/yr for as many as 10 m.y. within the Namche Barwa massif. This conclusion is also consistent with the exposure of anatectic rocks at Gyala Peri that yield U-Pb zircon rim ages as young as 0.9 Ma: in a region like the massif, marked by very high geothermal gradients, exhumation rates of ~10 mm/yr would be able to expose low-pressure anatectic rocks in such a short time.

One drawback to using a 1-D assumption to estimate exhumation rates is that this ignores both lateral variations in the thermal field and the horizontal component of rock advection, which has been shown to be significant in some settings (e.g., Herman et al., 2010). For the Namche Barwa massif, structural

and seismicity data suggest that the structure is bounded on the west, north, and east by steep structures that have accommodated tens of kilometers of rock uplift. Thus in this context a 1-D assumption to estimate rates is probably adequate. The northeast to southwest increase in cooling ages along the axis of the Namche Barwa massif and antiform (profile p4 in Fig. 15) is similar to the pattern of ages that can develop in the hanging wall above a large crustal thrust (e.g., Herman et al., 2010), but it is not clear for Namche Barwa what structure would be responsible.

Young Cooling Ages External to the Namche Barwa–Gyala Peri Massif

Along the western and northern margins of the Namche Barwa massif, $^{40}Ar/^{39}Ar$ biotite ages increase sharply across the steep brittle fault zone bounding the massif (Fig. 15D), and we interpret this increase to be the result of sharply differential rock uplift and exhumation rates across these fault zones. In contrast, the ages of lower temperature systems do not show this sharp offset. One could try to explain the lower temperature ages as evidence for distributed strain in which Lhasa block rocks were dragged up adjacent to the massif, perhaps as part of incipient outward growth of the structure (e.g., Burg et al., 1998; Seward and Burg, 2008). However, as defined by both bulk-mineral ages and the MDD analysis of sample BT-33–02 K-feldspar, the sharply inflected cooling histories of these massif-proximal samples challenge such a simple interpretation.

Independent inversion of the mineral cooling-age data and the K-feldspar age spectrum both suggest ~10 m.y or more of nearly isothermal conditions, from ca. 15 Ma to 2 Ma; mild reheating is permitted by the models of these data and results in a better fitting inversion for the K-feldspar. This interval was followed by very rapid cooling, ca. 2 Ma, from above 200 °C (Fig. 18B). Such a sharp quenching is nearly impossible to create with merely a pulse of erosion or incision. It is unlikely that the prequenching local geotherm had been steepened by rapid advection because the older biotite ages rule out the isothermal interval as an expression of protracted isothermal decompression. In the presence of normal crustal geotherms, the local relief of ~2 km is far too low to allow simple incision or headward cutting to have set and exposed systems having closure temperatures of 200 °C and more.

An explanation for these data might be found in lateral heat flow from the Namche Barwa massif into what are in effect country rocks. Such flow could raise the geotherm in Lhasa block rocks immediately adjacent to the massif, making it possible for much more modest degrees of incision to set lower temperature cooling-age systems. At the extreme rates and magnitudes of rock uplift within the Namche Barwa massif, high-temperature isotherms will be carried very close to the surface before diffusional heat loss can balance this energy input into the shallow crust. At the steep massif-bounding fault zones, this creates a contact-metamorphic system, in which heat from the advected massif diffuses out into the adjoining half space. Using the 5–10 m.y. petrological and geochronological estimate for the duration of rapid massif advection, along with a typical value for crustal thermal diffusivity of 10^{-6} m^2/s, yields an estimate of 12.5–25 km for the distance scale of lateral heat flow. This is consistent with the width of the zone in which we observed young zircon U-Th/He and fission-track ages from just outside the massif (Fig. 15).

We investigated this lateral-flow issue further using the Pecube finite-element model (Braun, 2003). Given the uncertainties in crustal thermal parameters, long-term fault geometries, and topographic evolution, we ran a simplified set of 2-D models that incorporated a sharp vertical fault across which there was strong differential rock uplift and erosion. Figure 19 summarizes the results and Table DR8 provides model parameters and related information about the modeling. The modeling clearly shows that the 200–300 °C isotherms (the range of relevance to zircon closure) would be significantly elevated close to the massif. In this scenario, rather than requiring 6 km or more of erosion, only a few kilometers of rapid erosion and/or incision into such a thermal structure could explain both the young U-Th/He ages outside of the massif, the sharp inflection in the cooling histories, and immediately adjacent to the northernmost termination of the massif,

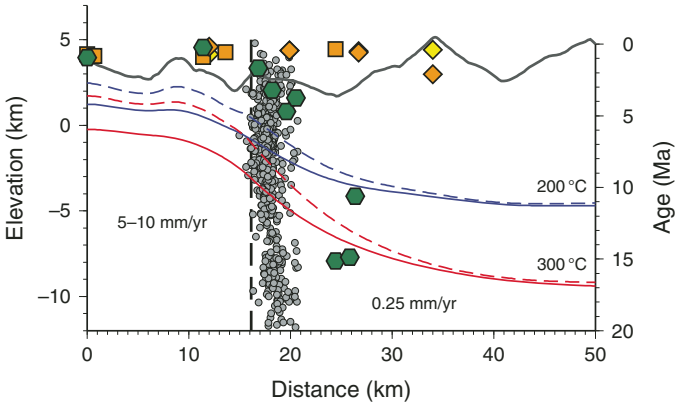

Figure 19. Summary of two-dimensional thermal modeling results for the northern margin of the Namche Barwa massif, using the Pecube model (Braun, 2003). Model parameters are given in Table DR8 (see footnote 1). Topography during model runs was fixed and is a mean for a swath perpendicular to the seismically active zone. The vertical fault in the model was placed at the basement-cover contact, and registered to the hypocenter locations (shown in gray). Each model was first run for 5 m.y. at 0.25 mm/yr exhumation rate to equilibrate isotherms beneath the topography, then rapid exhumation was turned on within the massif (left side of model space in figure). Results from two models are shown that roughly bracket the range of durations and rates estimated for the Namche Barwa massif: 5 mm/yr for a duration of 10 m.y. (solid), and 10 mm/yr for a duration of 5 m.y. (dashed). Local mineral ages are projected into the line of this profile: $^{40}Ar/^{39}Ar$ biotite—green hexagons; fission-track zircon—orange diamonds; U-Th/He zircon—orange squares; fission-track apatite—yellow diamond. Fission-track data are from Seward and Burg (2008). The model shows the scale of the lateral heat flow that is likely caused by the Namche Barwa uplift. It is possible that the starting country-rock geotherm was steeper and isotherms shallower overall, making it even more likely that an incision pulse of several kilometers could expose very young mineral ages at the surface.

the northward-increasing biotite ages that increase from ca. 2 to 15 Ma. It is interesting to note that the best fits to the BT-33–02 K-feldspar age spectrum occur when the inverse model is permitted to use solutions that involve reheating (Fig. 17), and models of just the bulk mineral-age data likewise permit reheating as a possible solution (Fig. 18B).

Based on this thermal modeling, we think that lateral heat flow provides the best explanation for the anomalous massif-proximal ages. Any shear heating within the Jiali fault zone would have to have been large in rate and magnitude and taken place ca. 2 Ma, but there is no independent evidence for such an event, and this process could not explain the younger ages to the west of the Namche Barwa massif near Dongjiu. Differential rock uplift immediately adjacent to the massif could not create the sharp inflection seen in the cooling histories, though such deformation would reinforce the observed pattern and cannot be ruled out.

Proposed Northward Growth of the Namche Barwa Structure

Burg et al. (1998) and Seward and Burg (2008) proposed that the northeast-plunging Namche Barwa antiform has grown and shifted to the northeast through a combination of doming and strike-slip offset, the antiform also narrowing as it was compressed; they cited the young fission-track cooling ages found outside the massif to the north as evidence of incipient northward growth of the plunging structure. It is true that toward the southwest, the Namche Barwa antiform showed a period of very rapid cooling, from perhaps 10 to 5 Ma, and the progressive trend in these lower-temperature thermochronological data might be interpreted as evidence for northward growth. We argue that the cooling-age data are more consistent with an earlier period of broad deformation and exhumation followed by a focusing of deformation and activity to the north, including development of the metamorphic massif and large-scale tectonic aneurysm behavior. The young ages to the north and west of the massif are likely to be a product of lateral flow of heat from the rapidly advected metamorphic massif, not evidence of a northward spread of rock uplift. Given petrological and zircon U-Pb evidence that the Namche Barwa massif has been undergoing rapid decompression for at least 5 m.y. and possibly as long as 10 m.y, its rapid exhumation was in fact coeval with the rapid exhumation farther to the south in the antiform (Fig. 18). However, whereas rapid exhumation in the antiform ceased ca. 5 Ma, it continued in the massif. Thus, in our view the entire Namche Barwa structure (antiform and massif) was active between 5 and 10 Ma, with active strain then focusing into the northern parts of the structure without any actual northward growth. In the Namche Barwa massif the lack of observed older cooling ages that document an early portion of its history is merely a preservation issue: current rocks cannot contain this record and the rocks that did have long since been eroded away. In contrast, farther south in the antiform the cessation of exhumation allowed an earlier cooling-age record to be preserved. Our interpretation of structural data (in the preceding) is that much of the evidence suggestive of strike-slip offset in fact reflects reorientation of thrust-sense indicators by late doming of the massif, such that northward translation of current Namche Barwa exposures is not required to explain the data.

Seismicity and Landsliding

Along the northern boundary of the massif, our structural observations of a steep fault zone across which there is a steep biotite cooling-age transition match well with the intense zone of seismicity that occurs in this region. Using the strong exhumation-rate gradients around the Namche Barwa massif as a test, Larsen and Montgomery (2012) showed how there is a strong correlation between landslide frequency and exhumation rate, such that beyond a slope-stability threshold, increased exhumation rate leads to increased landsliding rather than further slope steepening; the frequent occurrence of outburst floods also plays a role in this system. Larsen and Montgomery (2012) and Roering (2012) noted the feedbacks that could develop between tectonic forcing, climate, and surface processes. It seems likely that the high levels of seismicity and persistent shaking in this area serve as an important source for triggering landslides and an additional feedback between exhumation and strain. This feedback is additionally enhanced along ridge crests where topographic site effects cause gradients in ground acceleration (Meunier et al., 2008). Our data show concentrated zones of seismicity in the region with the youngest cooling ages and thus the inferred highest erosion rates. Such seismicity plays an important role in connecting tectonic rock uplift, landsliding, and exhumation, and the resulting enhanced flow that is part of the aneurysm model. In a region like this, given the link between strain rate and exhumation rate, landsliding triggered by earthquakes is likely equivalent in importance to landsliding triggered by outburst floods.

Synthesis of Observations: Model for Landscape and Tectonic Evolution in Southeastern Tibet

The following sequence of events would explain and link our observations about the tectonics and evolution of southeastern Tibet.

1. Early Himalayan convergent tectonics result in metamorphism that leaves the underthrust Indian crust in a relatively warm orogenic state, a condition that can help foster surface-crustal coupling of the sort predicted by the aneurysm model (Koons et al., 2013).

2. Indentor-corner dynamics nucleate a region of significant vertical strain near the plate corner in southeastern Tibet, across which an ancestral Yarlung Tsangpo flows.

3. Either by the previous mechanism or abetted by a more widespread one, the southeastern Tibetan Plateau is uplifted ca. 10 Ma. In response, major rivers like the ancestral Yarlung Tsangpo rapidly carve back into the margins of this uplift and produce a deeply incised, rapidly eroding high-relief landscape that together with the isostatic response to exhumation, removes perhaps 3–5 km of crust.

4. At 8–10 Ma, coupling begins between the deep incision caused by the ancestral Yarlung Tsangpo and advection of rocks at the Namche Barwa antiform, weakening the crust and beginning to focus strain toward the north, resulting in formation of the Namche Barwa massif. This coupling would have been enhanced by possible capture of the Yarlung Tsangpo across the steep topographic front of the uplifted region. Anatexis begins in response to the decompression associated with the rapid exhumation in the massif.

5. By ca. 5 Ma or earlier, strain has become focused into the seismically active, steeply bounded Namche Barwa–Gyala Peri massif. Rock uplift slows in the southern Namche Barwa antiform, possibly due to abandonment of a mid-crustal ramp. Exhumation is greatly inhibited in portions of the Lhasa block located upstream from the metamorphic massif because rock uplift within the massif couples with rapid incision at the Namche Barwa knickzone, stabilizing the knickzone at a high base level of ~3000 m. Overall relief of ~2 km in the southeasternmost Lhasa block remains as a relict of the earlier rapid regional erosion, but an enigmatic combination of deep and surface processes has conspired to maintain fairly uniform summit elevations, even though cooling ages show this higher elevation landscape to be diachronous.

6. By 1–2 Ma, Lhasa block rocks adjacent to the Namche Barwa massif have been warmed by at least 5 m.y. or more of lateral heat flow. Capture of the Po Tsangpo into the Yarlung Tsangpo occurs, driving the incision event recorded in young low-temperature cooling ages seen near the massif.

BROADER IMPLICATIONS AND CONCLUDING REMARKS

Applicability of the Tectonic Aneurysm Model to the Namche Barwa Massif

At Namche Barwa we observe a number of phenomena that are predicted by the tectonic aneurysm model: areally limited and rapid rock uplift and exhumation, coeval with recent and probably current anatexis, and focusing of strain into the massif. Initial deformation along the Namche Barwa antiform and the presence of the extreme stream power associated with the Namche Barwa knickzone (Finnegan et al., 2008) are added requirements of the aneurysm model that are met in this region. Significantly, the coincidence of stream power and deformation is long lived: geological map patterns, geomorphological metrics, our cooling ages, and the petrological history of the massif all suggest that for 5–10 m.y. the metamorphic massif has been fixed with respect to the large knickzone on the Yarlung Tsangpo (see also Finnegan et al., 2008; Koons et al., 2013).

Regional Geodynamic Implications

Our scenario for southeastern Tibet is marked by interactions that include coupling or links among surface and solid Earth processes that occur over a range of spatial scales. At a more regional scale, strains related to the evolving indentor corner coupled with fluvial networks lead to the focused rock uplift at Namche Barwa. In turn, this feature, though relatively small in areal extent, has a disproportionate impact on both landscape evolution and geodynamics in the eastern Himalaya and Tibet. In particular, we support the argument that by inhibiting headward incision by the Yarlung Tsangpo, the small Namche Barwa structure has shielded the southeastern Tibetan Plateau from excavation, and in turn maintained the current range-plateau critical-wedge geometry present along most of the Himalayan convergence zone. It also has a significant impact on the sedimentary record of easterrn-Himalayan exhumation and on present-day geologic hazards.

Role of Surface Processes in Geodynamics

In earlier publications (e.g., Zeitler et al., 2001a, 2001b; Koons et al., 2002; Finnegan et al., 2008) we advocated for the important role that surface processes could play in the geodynamics of orogens. More generally, surface-tectonic interactions have become a key part of many numerical models that incorporate focused erosion as an important control on particle paths and petrological evolution in orogens (e.g., Beaumont et al., 2001; Koons et al., 2002): the status of erosion has been promoted from that of a more passive response that could at best tie into tectonics via isostatic rebound, to a more active process that can become involved in feedbacks at multiple scales. Both in the way that fluvial exhumation at Namche Barwa seems to have coupled with deformation on a more local scale, and in the way that the Namche Barwa structure has stabilized the Big Bend knickzone and thus altered incision in Tibet by raising base level, it seems clear that erosion plays an important and active role in the geodynamics of southeastern Tibet.

Synorogenic Feedbacks at Namche Barwa

We discussed how, in the tectonic aneurysm model, a key feedback is the one between rock uplift as a manifestation of focused strain and rapid erosion, which serves to weaken the crust through steepening of the shallow crustal geotherm. Additional feedbacks also seem likely to come into play in a setting like Namche Barwa. Korup and Montgomery (2008) proposed that glacial damming in a high-relief setting like southeastern Tibet could stabilize knickpoints and focus exhumation, offering a possible link between tectonics, surface processes, and climate. Frequent outburst flooding, whether induced by damming by glaciers or landslides, could be another significant feedback, because the high discharges during outbursts are effective in increasing landsliding rates (Larsen and Montgomery, 2012) and evacuation of material. Our observation of very high levels of seismicity at the northern margins of the Namche Barwa massif adds another positive feedback: ground shaking by seismicity associated with high strain rates triggers the landslide-dominated exhumation that is in turn an important contributor to the strain focusing.

Geologic Hazards and Potential Risks

While southeastern Tibet is not heavily populated, there are risks to infrastructure and people near the massif and downstream from the knickpoint. Clearly the massif contains a number of seismogenic faults. In addition, the coincidence of the start of knickzone rapids with the brittle faults of the Nam-la thrust zone leads us to suspect that this structure, though aseismic during our observation period, is active and accumulating strain. Landslides, landslide damming, and earthquakes have and could continue to have serious impacts on important transportation routes like the Lhasa-Chengdu national highway. Because the Namche Barwa massif straddles the Yarlung Tsangpo, activity within or near the massif also poses potential risks to populations near the river's downstream continuation. For example, the Yigrong landslide and outburst flood in 2000 not only damaged local roads and bridges, but also damaged the homes of ~50,000 people downstream in India (Yin and Wang, 2005). In addition, over the past decade there has been talk of placing a hydroelectric dam or other structure across the Tsangpo within its Big Bend knickzone to tap some of the ~40,000 GW of power potentially available in the area (Watts, 2010). The frequency of landslides, landslide dams, and the high seismicity along the northern margin of the massif clearly merit careful study and monitoring before any such scheme is considered.

Impact of Namche Barwa on Foreland Sedimentation

A number of geochemical and detrital-dating studies have concluded that a significant fraction of Brahmaputra sediment is derived from the Namche Barwa area; as much as 60%–70% of the sediment load in the Yarlung Tsangpo–Siang River as it enters the Brahmaputra appears to be derived from Namche Barwa (e.g., Singh and France-Lanord, 2002; Stewart et al., 2008; Enkelmann et al., 2011). Our bedrock cooling-age data support this inference about modern sediment sourcing, but also suggest, together with petrological observations, that this localized sourcing has probably been true for the entire lifetime of the Namche Barwa massif, i.e., for as long as 10 m.y. As such, not only do studies of modern geochemical evolution need to account for the extremely localized sourcing of much of the sediment arriving in the foreland, but also any examination of the longer term molasse record needs to factor in this potential bias.

River Capture and Incision

As noted herein, many have commented on the possibility that river capture has been important in the landscape evolution in eastern and southeastern Tibet. River capture of major rivers millions of years in the past is difficult if not impossible to document in a region where there have been many kilometers of exhumation that would erase geomorphic evidence and across which an evolving and complex 3-D strain field could rearrange drainage patterns. However, the active tectonics and huge differential elevations at the margins of the Tibetan Plateau provide perhaps the best possible setting for fostering stream capture.

Our data for the Yarlung Tsangpo cannot provide any direct support for or against capture. In the tectonic aneurysm model that we favor, the necessary large and rapidly incised river valley could be provided by either an antecedent stream that runs astride a deforming region of crust, or by the arrival and development of such a valley via capture. In either case erosion could become rheologically coupled with deformation (Koons et al., 2002, 2013). The timing of events associated with the Namche Barwa–Gyala Peri massif broadly align with capture scenarios for the Yarlung Tsangpo that have been previously proposed (prior to 4 Ma, Clark et al., 2004; 4.4 Ma, Cina et al., 2009). He and Chen (2006) studied the molecular phylogeny of *Schizothorax* fishes and proposed capture of the Yarlung Tsangpo into the Brahmaputra at 6.8–7.3 Ma, using the Clark et al. (2004) proposals for drainage evolution as a framework. This timing matches many elements of our data and our proposed landscape evolution scenario well. Note that the magnitude and duration of the coupling associated with aneurysm development (Koons et al., 2013) mean that more transient landscape evolution of the type proposed by Zhang et al. (2012) is unlikely to leave petrological and geochronological records of the type seen at Namche Barwa.

Whatever the pre-capture course for a paleo–Yarlung Tsangpo might have been, it is possible that there has been a more recent capture of the current Yigrong Tsangpo and Po Tsangpo into the Namche Barwa knickzone. Our main line of evidence would be the nature of the quenched cooling histories of rocks located in these drainages, just north and west of the Namche Barwa massif. Capture of a southeast-flowing Yigrong–Po Tsangpo ancestor, likely aided by local faulting (Seward and Burg, 2008), could have provided the lower base level (3000+ m to <1000 m) that would drive such an incision pulse. Cross-valley profiles of drainages in this area are consistent with such capture-related incision, showing channels at least 2000 m below the mean topography of the surrounding highlands (Fig. 20). In this scenario, the timing of cooling-age quenching would approximate the time of capture, i.e., ca. 1–2 Ma.

Preservation in the Rock Record

We have argued that Namche Barwa massif played a significant role in the evolution of the eastern Himalaya and Tibet through its impacts on phenomena such as synorogenic sediment supply, regional landscape evolution, and regional dynamics. However, the small size of the massif is disproportionate to these impacts, and it is not obvious how much if any of the dynamic behavior of Namche Barwa will actually be discernible from the postorogenic record. Especially if modern anatectic rocks of the massif are being sourced from a mid-crustal ramp, postorogenic erosion could leave basement-rock exposures that at best indicate an anatectic dome, but provide no insight into the surface boundary conditions that helped shape feedbacks and strain focusing. The best, though indirect, evidence for aneurysm-

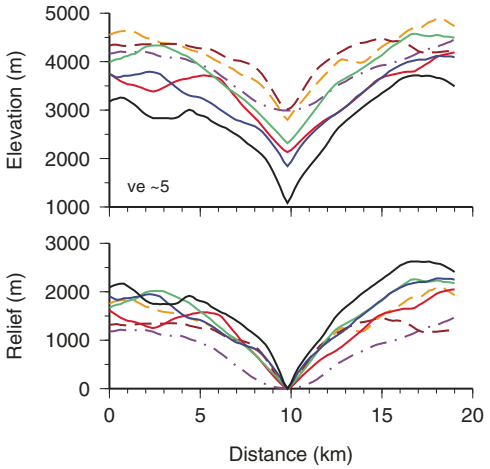

Figure 20. Mean valley cross-profiles and relief. Locations of swath profiles are shown in Figure 2. Black—p1 (lower Yarlung Tsangpo at base of knickzone); blue—p2 (lower Po Tsangpo near Yarlung Tsangpo confluence); green—p3 (upper Po Tsangpo to "Parlung" (see text) reach between Tungmai and Bomi); red—p4 (Yigrong Tsangpo); brown—p5 (Dongjiu River); orange—p6 (Rong Chu, near confluence with Dongjiu River); purple—p7 (lower Nyang Chu). Profiles shown with dashed lines are for locations either above the elevation of the Big Bend knickzone, or just at its margin. Swaths are 10–20 km wide as dictated by local geography; p3 is 40 km. For each swath, ~50–100 component profiles were taken at a constant azimuth perpendicular to the overall river trend; profiles were then aligned on the river channel. Elevations were taken from the Shuttle Radar Topography Mission 90 m digital elevation model, version 4.1 (Jarvis et al., 2008). While it is difficult to quantify topography in a region with such tortuous river channels (Figs. 2 and 5), within the Big Bend the relief of 2+ km in valleys graded directly to the Yarlung Tsangpo knickzone is consistent with a pulse of incision related to stream capture of the Po Tsangpo into the Yarlung Tsangpo.

style dynamics would probably be in synorogenic sediments. In thinking about orogenic evolution, the geology of the Namche Barwa region suggests that it will be important to keep in mind that quite localized and ephemeral structures and processes can have regional-scale impacts on geodynamics.

Future Work

The Namche Barwa massif, particularly the region near Gyala Peri peak, would appear to be an ideal laboratory in which to better understand metamorphic and anatectic processes in orogeny because, like at Nanga Parbat (Zeitler et al., 2001b), different observational reference frames can be integrated: fixed-frame geophysical observations could be combined with moving-frame data from petrology and geomorphological studies, and all these could be carried out with high resolution in space and time given the limited size of the feature and the young or active timing of various processes. Regionally, the cooling-age data we have collected suggest that the southeastern Lhasa block is also ideally poised for studies of landscape and relief evolution that have taken and are taking place in the face of significant gradients in exhumation and rock uplift. Moreover, such work could be fruitfully coupled with studies of deeper lithospheric processes and structures, given the evidence for lateral variations in Moho depth and heterogeneity in the presence of lower crustal eclogite. The sediment fill in the Yarlung Tsangpo River valley upstream of the knickpoint likely holds an interesting record worth examining. The documented occurrence of very high exhumation rates and seismicity, along with frequent landsliding and outburst flooding, argues that additional study and monitoring of the Namche Barwa massif and surrounding areas would be beneficial, given that such active processes are in play near a major river flowing across international borders into a highly populated region.

ACKNOWLEDGMENTS

This work was supported by a grant from the U.S National Science Foundation Continental Dynamics Program (EAR-0003462, Zeitler and Meltzer; EAR-0003673, Kidd). Support for the seismic deployment was provided by IRIS-PASSCAL (Incorporated Research Institutions for Seismology Program for Array Seismic Studies of the Continental Lithosphere). Indispensable logistical support and advice was provided by the Chengdu Institute for Mineral Resources (CIGMR), particularly Liu Yuping, Ding Jun, Zhang Xuanyang, Zhang Jianlong, and Tang Wen Qing. CIGMR also made available important samples from the interior of the Namche Barwa region; we thank Geng Quanru and the team that carried out this difficult traverse. Peter Reiners and Stefan Nicolescu provided U and Th determinations for our U-Th/He work. We acknowledge all the members of the large indentor-corners project for their efforts and contributions, in particular Molly Malloy, Michael Kutney, Bruce Idleman, Brian Zurek, Stephane Sol, Noah Finnegan, Peter Koons, and Bernard Hallet for their considerable effort, skillful assistance, and interesting discussions. Many of the figures in this paper were drafted with the help of GMT (Generic Mapping Tools; Wessel and Smith, 1991). We thank Michael Taylor, Marin Clark, and especially Jean-Philippe Avouac for their reviews.

REFERENCES CITED

An, Z., Kutzbach, J.E., Prell, W.L., and Porter, S.C., 2001, Evolution of the Asian monsoons and phased uplift of the Himalayan-Tibetan plateau since late Miocene times: Nature, v. 411, p. 62–66, doi:10.1038/35075035.

Armijo, R., Tapponnier, P., and Tonglin, H., 1989, Late Cenozoic right-lateral strike-slip faulting in southern Tibet: Journal of Geophysical Research, v. 94, p. 2787–2838, doi:10.1029/JB094iB03p02787.

Avouac, J.P., and Burov, E.B., 1996, Erosion as a driving mechanism of intracontinental mountain growth: Journal of Geophysical Research, v. 101, p. 17747–17769, doi:10.1029/96JB01344.

Baker, I., 2004, The Heart of the World: A Journey to the Last Secret Place: New York, Penguin, 511 p.

Beaumont, C., Jamieson, R.A., Nguyen, M.H., and Lee, B., 2001, Himalayan tectonics explained by extrusion of a low-viscosity channel coupled to focused surface denudation: Nature, v. 414, p. 738–742, doi:10.1038/414738a.

Booth, A.L., Zeitler, P.K., Kidd, W.S.F., Wooden, J., Yuping, L., Idleman, B., Hren, M., and Chamberlain, C.P., 2004, U-Pb zircon constraints on the tectonic evolution of southeastern Tibet, Namche Barwa area: American Journal of Science, v. 304, p. 889–929, doi:10.2475/ajs.304.10.889.

Booth, A.L., Chamberlain, C.P., Kidd, W.S.F., and Zeitler, P.K., 2009, Constraints on the metamorphic evolution of the eastern Himalayan syntaxis from geochronologic and petrologic studies of Namche Barwa: Geological Society of America Bulletin, v. 121, p. 385–407, doi:10.1130/B26041.1.

Boulder Real Time Technologies, Inc., 2008, Antelope Version 4.10 release: Boulder, Colorado, Boulder Real Time Technologies, Inc., http://www.brtt.com/release/4.10/.

Braun, J., 2002, Quantifying the effect of recent relief changes on age-elevation relationships: Earth and Planetary Science Letters, v. 200, p. 331–343, doi:10.1016/S0012-821X(02)00638-6.

Braun, J., 2003, Pecube: A new finite element code to solve the heat transport equation in three dimensions in the Earth's crust including the effects of a time-varying, finite amplitude surface topography: Computers & Geosciences, v. 29, p. 787–794, doi:10.1016/S0098-3004(03)00052-9.

Brookfield, M.E., 1998, The evolution of the great river systems of southern Asia during the Cenozoic India-Asia collision: Rivers draining southwards: Geomorphology, v. 22, p. 285–312, doi:10.1016/S0169-555X(97)00082-2.

Brozović, N., Burbank, D.W., and Meigs, A.J., 1997, Climatic limits on landscape development in the northwestern Himalayas: Science, v. 276, no. 5312, p. 571–574, doi:10.1126/science.276.5312.571.

Burchfiel, B.C., Chen, Z., Hodges, K.V., Liu, Y., Royden, L.H., Deng, C., and Xu, J., 1992, The South Tibetan Detachment System, Himalayan Orogen: Extension Contemporaneous with and Parallel to Shortening in a Collisional Mountain Belt: Geological Society of America Special Paper 269, 41 p., doi:10.1130/SPE269.

Burchfiel, B.C., Clark, M.K., Wang, E., Chen, Z., Liu, Y., and Pan, G., 2000, Tectonic framework of the Namche Barwa region, eastern Himalayan syntaxis, SE Tibet: Geological Society of America Abstracts with Programs, v. 32, no. 7, p. A-33.

Burg, J.-P., and Podladchikov, Y., 1999, Lithospheric scale folding: Numerical modeling and application to the Himalayan syntaxes: International Journal of Earth Sciences, v. 88, p. 190–200, doi:10.1007/s005310050259.

Burg, J.-P., Davy, P., Nievergelt, P., Oberli, F., Seward, D., Diao, Z., and Meier, M., 1997, Exhumation during crustal folding in the Namche-Barwa syntaxis: Terra Nova, v. 9, p. 53–56, doi:10.1111/j.1365-3121.1997.tb00001.x.

Burg, J.-P., Nievergelt, P., Oberli, F., Seward, D., Davy, P., Maurin, J.-C., Diao, Z., and Meier, M., 1998, The Namche-Barwa syntaxis: Evidence for exhumation related to compressional crustal folding: Journal of Asian Earth Sciences, v. 16, p. 239–252, doi:10.1016/S0743-9547(98)00002-6.

Cherniak, D.J., Watson, E.B., and Thomas, J.B., 2009, Diffusion of helium in zircon and apatite: Chemical Geology, v. 268, p. 155–166, doi:10.1016/j.chemgeo.2009.08.011.

Chiu, H.Y., Chung, S.L., Wu, F.Y., Liu, D.Y., Liang, Y.H., Lin, Y.J., Iizuka, Y., Xie, L.W., Wang, Y.B., and Chu, M.F., 2009, Zircon U-Pb and Hf isotope constraints from eastern Transhimalayan batholiths on the precollisional magmatic and tectonic evolution in southern Tibet: Tectonophysics, v. 477, p. 3–19, doi:10.1016/j.tecto.2009.02.034.

Chung, S.L., Liu, D.Y., Ji, J.Q., Chu, M.F., Lee, H.Y., Wen, D.J., Lo, C.H., Lee, T.Y., Qian, Q., and Zhang, Q., 2003, Adakites from continental collision zones. Melting of thickened lower crust beneath southern Tibet: Geology, v. 31, p. 1021–1024, doi:10.1130/G19796.1.

Cina, S.E., Yin, A., Grove, M., Dubey, C.S., Shukla, D.P., Lovera, O.M., Kelty, T.K., Gehrels, G.E., and Foster, D.A., 2009, Gangdese arc detritus within the eastern Himalayan Neogene foreland basin: Implications for the Neogene evolution of the Yalu-Brahmaputra River system: Earth and Planetary Science Letters, v. 285, p. 150–162, doi:10.1016/j.epsl.2009.06.005.

Clark, M.K., Schoenbohm, L.M., Royden, L.H., Whipple, K.X., Burchfiel, B.C., Zhang, X., Tang, W., Wang, E., and Chen, L., 2004, Surface uplift, tectonics, and erosion of eastern Tibet from large-scale drainage patterns: Tectonics, v. 23, TC1006, doi:10.1029/2002TC001402.

Clark, M.K., House, M.A., Royden, L.H., Whipple, K.X., Burchfiel, B.C., Zhang, X., and Tang, W., 2005, Late Cenozoic uplift of southeastern Tibet: Geology, v. 33, p. 525–528, doi:10.1130/G21265.1.

Copeland, P., Harrison, T.M., Kidd, W.S.F., Ronghua, X., and Yuquan, Z., 1987, Rapid early Miocene acceleration of uplift in the Gandese Belt, Xizang-southern Tibet, and its bearing on accommodation mechanisms of the India-Asia collision: Earth and Planetary Science Letters, v. 86, p. 240–252, doi:10.1016/0012-821X(87)90224-X.

Cox, K., ed., 2001, Frank Kingdon Ward's riddle of the Tsangpo Gorges: Retracing the epic journey of 1924–25 in south-east Tibet: London, Antique Collector's Club, 320 p.

Craw, D., Koons, P.O., Zeitler, P.K., and Kidd, W.S.F., 2005, Fluid evolution and thermal structure in the rapidly exhuming gneiss complex of Namche Barwa–Gyala Peri, eastern Himalayan syntaxis: Journal of Metamorphic Geology, v. 23, p. 829–845, doi:10.1111/j.1525-1314.2005.00612.x.

DeCelles, P.G., Kapp, P., Ding, L., and Gehrels, G.E., 2007, Late Cretaceous to middle Tertiary basin evolution in the central Tibetan Plateau: Changing environments in response to tectonic partitioning, aridification, and regional elevation gain: Geological Society of America Bulletin, v. 119, p. 654–680, doi:10.1130/B26074.1.

DePaolo, D.J., Weaver, K.L., Mo, X., Zhao, Z., and Harrison, T.M., 2008, Regional isotopic patterns in granitic rocks of southern Tibet and evolution of crustal structure during the Indo-Asian collision: Geochimica et Cosmochimica Acta, v. 72, p. A211.

Ding, L., Zhong, D., Yin, A., Kapp, P.A., and Harrison, T.M., 2001, Cenozoic structural and metamorphic evolution of the eastern Himalayan syntaxis (Namche Barwa): Earth and Planetary Science Letters, v. 192, p. 423–438, doi:10.1016/S0012-821X(01)00463-0.

Duvall, A.R., Clark, M.K., Avdeev, B., Farley, K.A., and Chen, Z., 2012, Widespread late Cenozoic increase in erosion rates across the interior of eastern Tibet constrained by detrital low-temperature thermochronometry: Tectonics, v. 31, TC3014, doi:10.1029/2011TC002969.

Edwards, M., Kidd, W., Pecher, A., Burchfiel, C., and Royden, L., 1999, Southern Tibet detachment system (STDS) at Khula Kangri, eastern Himalaya: A large-area, shallow detachment stretching into Bhutan?: Journal of Geology, v. 107, p. 623–631, doi:10.1086/314366.

Enkelmann, E., Ehlers, T.A., Zeitler, P.K., and Hallet, B., 2011, Denudation of the Namche Barwa antiform, eastern Himalaya: Earth and Planetary Science Letters, v. 307, p. 323–333, doi:10.1016/j.epsl.2011.05.004.

Evans, S.G., and Delaney, K.B., 2011, Characterization of the 2000 Yigong Zangbo River (Tibet) landslide dam and impoundment by remote sensing, *in* Evans, S.G., et al., eds., Natural and artificial rockslide dams: Lecture Notes in Earth Sciences Volume 133: Berlin, Springer, p. 543–559, doi:10.1007/978-3-642-04764-0_22.

Finnegan, N.J., Hallet, B., Montgomery, D.R., Zeitler, P.K., Stone, J.O., Anders, A.M., and Liu Yuping, 2008, Coupling of rock uplift and river incision in the Namche Barwa–Gyala Peri massif, Tibet: Geological Society of America Bulletin, v. 120, p. 142–155, doi:10.1130/B26224.1.

Flowers, R.M., Ketcham, R.A., Shuster, D.L., and Farley, K.A., 2009, Apatite (U-Th)/He thermochronometry using a radiation damage accumulation and annealing model: Geochimica et Cosmochimica Acta, v. 73, p. 2347–2365, doi:10.1016/j.gca.2009.01.015.

Gan, W., Zhang, P., Shen, Z.K., Niu, Z., Wang, M., Wan, Y., Zhou, D., and Cheng, J., 2007, Present-day crustal motion within the Tibetan Plateau inferred from GPS measurements: Journal of Geophysical Research, v. 112, B08416, doi:10.1029/2005JB004120.

Garzanti, E., Vezzoli, G., Andò, S., France-Lanord, C., Singh, S.K., and Foster, G., 2004, Sediment composition and focused erosion in collision orogens: The Brahmaputra case: Earth and Planetary Science Letters, v. 220, p. 157–174, doi:10.1016/S0012-821X(04)00035-4.

Geng, Q., Pan, G., Zheng, L., Chen, Z., Sun, Z., Ou, C., Dong, H., Wang, X., Li, S., Lou, X., and Fu, H., and 14 unnamed others, 2003, Geologic map of Motou area: Chengdu, China, Chengdu Institute of Geology and Mineral Resources, scale 1:250,000.

Geng, Q., Pan, G., Zheng, L., Chen, Z., Fisher, R.D., Sun, Z., Ou, C.-S., Dong, H., Wang, X., Li, S., Lou, X., and Fu, H., 2006, The eastern Himalayan Syntaxis; major tectonic domains, ophiolitic melanges and geologic evolution: Journal of Asian Earth Sciences, v. 27, p. 265–285, doi:10.1016/j.jseaes.2005.03.009.

Grove, M., and Harrison, T.M., 1996, ^{40}Ar diffusion in Fe-rich biotite: American Mineralogist, v. 81, p. 940–951.

Guilmette, C., Indares, A., and Hébert, R., 2011, High-pressure anatectic paragneisses from the Namche Barwa, Eastern Himalayan Syntaxis: Textural evidence for partial melting, phase equilibria modeling and tectonic implications: Lithos, v. 124, p. 66–81, doi:10.1016/j.lithos.2010.09.003.

Guo, L., Zhang, H.-F., Harris, N., Parrish, R., Xu, W.-C., and Shi, Z.-L., 2012, Paleogene crustal anatexis and metamorphism in Lhasa terrane, eastern Himalayan syntaxis: Evidence from U-Pb zircon ages and Hf isotopic compositions of the Nyingchi Complex: Gondwana Research, v. 21, p. 100–111, doi:10.1016/j.gr.2011.03.002.

Hallet, B., and Molnar, P., 2001, Distorted drainage basins as markers of crustal strain east of the Himalayas: Journal of Geophysical Research, v. 106, no. B7, p. 13,697–13,709, doi:10.1029/2000JB900335.

Harrison, T.M., and Zeitler, P.K., 2005, Fundamentals of noble gas thermochronometry, *in* Reiners, P.W., and Ehlers, T.A., eds., Low-temperature thermochronology: Techniques, interpretations, and applications: Mineralogical Society of America Reviews in Mineralogy and Geochemistry Volume 58, p. 123–149, doi:10.2138/rmg.2005.58.5.

Harrison, T.M., Grove, M., Lovera, O.M., and Zeitler, P.K., 2005, Continuous thermal histories from inversion of closure profiles, *in* Reiners, P.W., and Ehlers, T.A., eds., Low-temperature thermochronology: Techniques, interpretations, and applications: Mineralogical Society of America Reviews in Mineralogy and Geochemistry Volume 58, p. 389–409, doi:10.2138/rmg.2005.58.5.

He, D., and Chen, Y., 2006, Biogeography and molecular phylogeny of the genus *Schizothorax* (Teleostei: Cyprinidae) in China inferred from cytochrome *b* sequences: Journal of Biogeography, v. 33, p. 1448–1460, doi:10.1111/j.1365-2699.2006.01510.x.

Herman, F., Copeland, P., Avouac, J.-P., Bollinger, L., Mahéo, G., Le Fort, P., Rai, S., Foster, D., Pêcher, A., Stüwe, K., and Henry, P., 2010, Exhumation, crustal deformation, and thermal structure of the Nepal Himalaya derived from the inversion of thermochronological and thermobarometric data and modeling of the topography: Journal of Geophysical Research, v. 115, B06407, doi:10.1029/2008JB006126.

Hetényi, G., Rodolphe, C., Fabrice, B., Laurent, B., Jérôme, V., John, L.N., and Michel, D., 2007, Density distribution of the India plate beneath the Tibetan plateau: Geophysical and petrological constraints on the kinetics of lower-crustal eclogitization: Earth and Planetary Science Letters, v. 264, p. 226–244, doi:10.1016/j.epsl.2007.09.036.

Jarvis, A., Reuter, H.I., Nelson, A., and Guevara, E., 2008, Hole-filled SRTM for the globe Version 4: CGIAR-CSI SRTM (CGIAR Consortium for Spatial Information Shuttle Radar Topography Mission) 90m Database: http://srtm.csi.cgiar.org.

Ketcham, R.A., 2005, Forward and inverse modeling of low-temperature thermochronometry data, *in* Reiners, P.W., and Ehlers, T.A., eds., Low-temperature thermochronology: Techniques, interpretations, and applications: Mineralogical Society of America Reviews in Mineralogy and Geochemistry Volume 58, p. 275–314, doi:10.2138/rmg.2005.58.11.

Kidd, WS.F., Lim, C., Zeitler, P.K., Enkelmann, E., Booth, A.L., Chamberlain, C.P., Tang, W., Liu, Y., Craw, D., 2006, Structural and tectonic geology of the Namche Barwa–Gyala Peri antiform, southeastern Tibet: Eos (Transactions, American Geophysical Union), v. 87, abs. T23B–0480.

Kind, R., Yuan, X., Saul, J., Nelson, D., Sobolev, S.V., Mechie, J., Zhao, W., Kosarev, G., Ni, J., Achauer, U., and Jiang, M., 2002, Seismic images of crust and upper mantle beneath Tibet: Evidence for Eurasian plate subduction: Science, v. 298, p. 1219–1221, doi:10.1126/science.1078115.

Kingdon-Ward, F., 1926, The riddle of the Tsangpo gorges: London, Edward Arnold & Co., 328 p.

Koons, P.O., 1995, Modelling the topographic evolution of collisional mountain belts: Annual Review of Earth and Planetary Sciences, v. 23, p. 375–408, doi:10.1146/annurev.ea.23.050195.002111.

Koons, P.O., Zeitler, P.K., Chamberlain, C.P., Craw, D., and Meltzer, A.S., 2002, Mechanical links between erosion and metamorphism in Nanga Parbat, Pakistan Himalaya: American Journal of Science, v. 302, p. 749–773, doi:10.2475/ajs.302.9.749.

Koons, P.O., Zeitler, P.K., and Hallet, B., 2013, Tectonic aneurysms and mountain building, *in* Shroder, J., ed., Tectonic geomorphology: Treatise on Geomorphology Volume 5, p. 318–349, doi:10.1016/B978-0-12-374739-6.00094-4

Korup, O., and Montgomery, D.R., 2008, Do glacier dams retard river incision into southeast Tibet?: Nature, v. 455, p. 786–789, doi:10.1038/nature07322.

Larsen, I.J., and Montgomery, D.R., 2012, Landslide erosion coupled to tectonics and river incision: Nature Geoscience, v. 5, p. 468–473, doi:10.1038/ngeo1479.

Lee, H.-Y., Chung, S.-L., Wang, J.-R., Wen, D.-J., Lo, C.-H., Yang, T.F., Zhang, Y., Xie, Y., Lee, T.-Y., Wu, G., and Ji, J., 2003, Miocene Jiali faulting and its implications for Tibetan tectonic evolution: Earth and Planetary Science Letters, v. 205, p. 185–194, doi:10.1016/S0012-821X(02)01040-3.

Li, C., Van der Hilst, R.D., Meltzer, A.S., and England, E.R., 2008, Subduction of the Indian lithosphere beneath the Tibetan Plateau and Burma: Earth and Planetary Science Letters, v. 274, p. 157–168, doi:10.1016/j.epsl.2008.07.016.

Liu, Y., and Zhong, D., 1997, Petrology of high-pressure granulites from the eastern Himalayan syntaxis: Journal of Metamorphic Geology, v. 15, p. 451–466, doi:10.1111/j.1525-1314.1997.00033.x.

Lovera, O.M., Richter, F.M., and Harrison, T.M., 1989, The $^{40}Ar/^{39}Ar$ themochronometry for slowly cooled samples having a distribution of diffusion domain sizes: Journal of Geophysical Research, v. 94, p. 17917–17935, doi:10.1029/JB094iB12p17917.

Lovera, O.M., Grove, M., Harrison, T.M., and Mahon, K.I., 1997, Systematic analysis of K-feldspar $^{40}Ar/^{39}Ar$ step-heating experiments I: Significance of activation energy determinations: Geochimica et Cosmochimica Acta, v. 61, p. 3171–3192, doi:10.1016/S0016-7037(97)00147-6.

Meunier, P., Hovius, N., and Haines, J.A., 2008, Topographic site effects and the location of earthquake induced landslides: Earth and Planetary Science Letters, v. 275, p. 221–232, doi:10.1016/j.epsl.2008.07.020.

Molnar, P., England, P., and Martinod, J., 1993, Mantle dynamics, uplift of the Tibetan Plateau, and the Indian monsoon: Reviews of Geophysics, v. 31, p. 357–396, doi:10.1029/93RG02030.

Montgomery, D.R., Hallet, B., Yuping, L., Finnegan, N., Anders, A., Gillespie, A., and Greenberg, H., 2004, Evidence for Holocene megafloods downs the Tsangpo River gorge, southeastern Tibet: Quaternary Research, v. 62, p. 201–207, doi:10.1016/j.yqres.2004.06.008.

Nábelek, J., Hetényi, G., Vergne, J., Sapkota, S., Kafle, B., Mei Jiang, Heping Su, Chen, J., Bor-Shouh Huang, and the Hi-CLIMB Team, 2009, Underplating in the Himalaya-Tibet collision zone revealed by the Hi-CLIMB Experiment: Science, v. 325, no. 5946, p. 1371, doi:10.1126/science.1167719.

Najman, Y., Appel, E., Boudagher-Fadel, M., Bown, P., Carter, A., Garzanti, E., Godin, L., Han, J., Liebke, U., Oliver, G., Parrish, R., and Vezzoli, G., 2010, Timing of India-Asia collision: Geological, biostratigraphic, and palaeomagnetic constraints: Journal of Geophysical Research, v. 115, B12416, doi:10.1029/2010JB007673, 18 p.

Ouimet, W., Whipple, K., Roden, L., Reiners, P., Hodges, K., and Pringle, M., 2010, Regional incision of the eastern margin of the Tibetan Plateau: Lithosphere, v. 2, p. 50–63, doi:10.1130/L57.1.

Pan, G., Ding, J., Yao, D., Wang, L., Luo, J., Yan, Y., Yong, Y., Zheng, J., Liang, X., Qin, D., Jiang, X., Wang, Q., Li, R., Geng, Q., Liao, Z., Zhu, D., and Yu, R., 2004, Geological map of the Qinghai-Xizang (Tibet) Plateau and adjacent areas: Chengdu, China, Chengdu Cartographic Publishing House, scale 1:1,500,000.

Quidelleur, X., Grove, M., Lovera, O.M., Harrison, T.M., Yin, A., and Ryerson, F.J., 1997, The thermal evolution and slip history of the Renbu Zedong thrust, southeastern Tibet: Journal of Geophysical Research, v. 102, p. 2659–2679, doi:10.1029/96JB02483.

Reich, M., Ewing, R.C., Ehlers, T.A., and Becker, U., 2007, Low-temperature anisotropic diffusion of helium in zircon: Implications for zircon (U–Th)/He thermochronometry: Geochimica et Cosmochimica Acta, v. 71, p. 3119–3130, doi:10.1016/j.gca.2007.03.033.

Reiners, P.W., and Brandon, M.T., 2006, Using thermochronology to understand orogenic erosion: Annual Review of Earth and Planetary Sciences, v. 34, p. 419–466, doi:10.1146/annurev.earth.34.031405.125202.

Reiners, P.W., Spell, T.L., Nicolescu, S., and Zanetti, K.A., 2004, Zircon (U-Th)/He thermochronometry: He diffusion and comparisons with $^{40}Ar/^{39}Ar$ dating: Geochimica et Cosmochimica Acta, v. 68, p. 1857–1887, doi:10.1016/j.gca.2003.10.021.

Richter, F.M., Lovera, O.M., Harrison, T.M., and Copeland, P., 1991, Tibetan tectonics from $^{40}Ar/^{39}Ar$ analysis of a single feldspar sample: Earth and Planetary Science Letters, v. 105, p. 266–278, doi:10.1016/0012-821X(91)90136-6.

Roering, J., 2012, Tectonic geomorphology: Landslides limit mountain relief: Nature Geoscience, v. 5, p. 446-447, doi:10.1038/ngeo1511.

Rowley, D.B., and Currie, B.S., 2006, Palaeo-altimetry of the late Eocene to Miocene Lunpola basin, central Tibet: Nature, v. 439, p. 677–681, doi:10.1038/nature04506.

Rubatto, D., 2002, Zircon trace element geochemistry: Partitioning with garnet and the link between U-Pb ages and metamorphism: Chemical Geology, v. 184, p. 123–138, doi:10.1016/S0009-2541(01)00355-2.

Schulte-Pelkum, V., Monsalve, G., Sheehan, A., Pandey, M.R., Sapkota, S., Bilham, R., and Wu, F., 2005, Imaging the Indian subcontinent beneath the Himalaya: Nature, v. 435, p. 1222–1225, doi:10.1038/nature03678.

Seeber, L., and Gornitz, V., 1983, River profiles along the Himalayan arc as indicators of active tectonics: Tectonophysics, v. 92, p. 335–367, doi:10.1016/0040-1951(83)90201-9.

Seward, D., and Burg, J.P., 2008, Growth of the Namche Barwa Syntaxis and associated evolution of the Tsangpo Gorge: Constraints from structural and thermochronological data: Tectonophysics, v. 451, p. 282–289, doi:10.1016/j.tecto.2007.11.057.

Singh, S.K., and France-Lanord, C., 2002, Tracing the distribution of erosion in the Brahmaputra watershed from isotopic compositions of stream sediments: Earth and Planetary Science Letters, v. 202, p. 645–662, doi:10.1016/S0012-821X(02)00822-1.

Sol, S., Meltzer, A., Bürgmann, R., van der Hilst, R.D., King, R., Chen, Z., Koons, P.O., Lev, E., Liu, Y.P., Zeitler, P.K., Zhang, X., Zhang, J., and Zurek, B., 2007, Geodynamics of the southeastern Tibetan Plateau from seismic anisotropy and geodesy: Geology, v. 35, p. 563–566, doi:10.1130/G23408A.1.

Stewart, R.J., Hallet, B., Zeitler, P.K., Malloy, M.A., Allen, C.M., and Trippett, D., 2008, Brahmaputra sediment flux dominated by highly localized rapid erosion from the easternmost Himalaya: Geology, v. 36, p. 711–714, doi:10.1130/G24890A.1.

Su, W., Zhang, M., Liu, X., Lin, J., Ye, K., and Liu, X., 2012, Exact timing of granulite metamorphism in the Namche-Barwa, eastern Himalayan syntaxis: New constrains from SIMS U-Pb zircon age: International Journal of Earth Sciences, v. 101, p. 239–252, doi:10.1007/s00531-011-0656-0.

Vermeesch, P., 2008, Three new ways to calculate average (U-Th)/He ages: Chemical Geology, v. 249, p. 339–347, doi:10.1016/j.chemgeo.2008.01.027.

Waldhauser, F., and Ellsworth, W.L., 2000, A double-difference earthquake location algorithm; method and application to the northern Hayward fault, California: Seismological Society of America Bulletin, v. 90, p. 1353–1368, doi:10.1785/0120000006.

Watts, J., 2010, Chinese engineers propose world's biggest hydro-electric project in Tibet: *The Guardian*, Monday 24 May 2010 11.00 EDT, http://www.guardian.co.uk/environment/2010/may/24/chinese-hydroengineers-propose-tibet-dam.

Wen, D.R., Liu, D.Y., Chung, S.L., Chu, M.F., Ji, J.Q., Zhang, Q., Song, B., Lee, T.Y., Yeh, M.W., and Lo, C.H., 2008, Zircon SHRIMP U-Pb ages of the Gangdese Batholith and implications for Neotethyan subduction in southern Tibet: Chemical Geology, v. 252, p. 191–201, doi:10.1016/j.chemgeo.2008.03.003.

Wessel, P., and Smith, W.H.F., 1991, Free software helps map and display data: Eos (Transactions, American Geophysical Union), v. 72, p. 441, doi:10.1029/90EO00319.

Xu, W.C., Zhang, H.F., Parrish, R., Harris, N., Guo, L., and Yuan, H.L., 2010, Timing of granulite facies metamorphism in the eastern Himalayan syntaxis and its tectonic implications: Tectonophysics, v. 485, p. 231–244, doi:10.1016/j.tecto.2009.12.023.

Xu, Z., Ji, S., Cai, Z., Zeng, L., Geng, Q., and Cao, H., 2012, Kinematics and dynamics of the Namche Barwa Syntaxis, eastern Himalaya: Constraints from deformation, fabrics and geochronology: Gondwana Research, v. 21, p. 19–36, doi:10.1016/j.gr.2011.06.010.

Yin, A., and Harrison, T.M., 2000, Geologic evolution of the Himalayan-Tibetan orogen: Annual Reviews of Earth and Planetary Sciences, v. 28, p. 211–280, doi:10.1146/annurev.earth.28.1.211.

Yin, A., Harrison, T.M., Ryerson, F.J., Chen, W., Kidd, W.S.F., and Copeland, P., 1994, Tertiary structural evolution of the Gangdese thrust system, southeastern Tibet: Journal of Geophysical Research, v. 99, p. 18175–18201, doi:10.1029/94JB00504.

Yin, A., Harrison, T.M., Murphy, M.A., Grove, M., Nie, S., Ryerson, F.J., Feng, W.X., and Le, C.Z., 1999, Tertiary deformation history of southeastern and southwestern Tibet during the Indo-Asian collision: Geological Society of America Bulletin, v. 111, p. 1644–1664, doi:10.1130/0016-7606(1999)111<1644:TDHOSA>2.3.CO;2.

Yin, Y., and Wang, S., 2005, Landslide hazard and reduction strategy in China, *in* Hungr, O., et al., eds., Landslide risk management: Leiden, A.A. Balkema, p. 423–426.

Zeitler, P.K., 2004, Arvert 4.1. Inversion of $^{40}Ar/^{39}Ar$ age spectra. User's manual: http://www.ees.lehigh.edu/EESdocs/geochron/downloads/arvert/arvert_41_manual.pdf) (version 4.1 update 7 April, 2012).

Zeitler, P.K., Meltzer, A.S., Koons, P.O., Craw, D., Hallet, B., Chamberlain, C.P., Kidd, W.S.F., Park, S., Seeber, L., Bishop, M.L., and Shroder, J., 2001a, Erosion, Himalayan geodynamics, and the geology of metamorphism: GSA Today, v. 11, p. 4–8, doi:10.1130/1052-5173(2001)011<0004:EHGATG>2.0.CO;2.

Zeitler, P.K., Koons, P.O., Bishop, M.L., Chamberlain, C.P., Craw, D., Edwards, M.A., Hamidullah, S., Jan, M.Q., Khan, M.A., Khattak, M.U.K., Kidd, W.S.F., Mackie, R.L., Meltzer, A.S., Park, S.K., Pecher, A., Poage, M.A., Sarker, G., Schneider, D.A., Seeber, L., and Shroder, J., 2001b, Crustal reworking at Nanga Parbat, Pakistan: Evidence for erosional focusing of crustal strain: Tectonics, v. 20, p. 712–728, doi:10.1029/2000TC001243.

Zeng, L., Gao, L.-E., Dong, C., and Tang, S., 2012, High-pressure melting of metapelite and the formation of Ca-rich granitic melts in the Namche Barwa Massif, southern Tibet: Gondwana Research, v. 21, p. 138–151, doi:10.1016/j.gr.2011.07.023.

Zhang, H., and Thurber, C.H., 2003, Double-difference tomography: The method and its application to the Hayward fault, California: Seismological Society of America Bulletin, v. 93, p. 1875, doi:10.1785/0120020190.

Zhang, J., Ji, J., Zhong, D., Ding, L., and He, S., 2004, Structural pattern of eastern Himalayan syntaxis in Namjagbarwa and its formation process: Science in China, ser. D, Earth Sciences, v. 47, no. 2, p. 138–150.

Zhang, J.Y., Yin, A., Liu, W.C., Wu, F.Y., Lin, D., and Grove, M., 2012, Coupled U-Pb dating and Hf isotopic analysis of detrital zircon of modern river sand from the Yalu River (Yarlung Tsangpo) drainage system in southern Tibet: Constraints on the transport processes and evolution of Himalayan rivers: Geological Society of America Bulletin, v. 124, p. 1449–1473, doi:10.1130/B30592.1.

Zhu, B., Kidd, W.S.F., Rowley, D.B., Currie, B.S., and Shafique, N., 2005, Age of initiation of the India-Asia collision in the east-central Himalaya: Journal of Geology, v. 113, p. 265–285, doi:10.1086/428805.

Zhu, D.C., Mo, X.X., Zhao, Z.D., Niu, Y.L., Wang, L.Q., Chu, Q.H., Pan, G.T., Xue, J.F., and Zhou, C.Y., 2010, Presence of Permian extension- and arc-type magmatism in southern Tibet: Paleogeographic implications: Geological Society of America Bulletin, v. 122, p. 979–993, doi:10.1130/B30062.1.

Zhu, D.C., Zhao, Z.D., Niu, Y.L., Mo, X.X., Chung, S.L., Hou, Z.Q., Wang, L.Q., and Wu, F.Y., 2011, The Lhasa terrane: Record of a microcontinent and its histories of drift and growth: Earth and Planetary Science Letters, v. 301, p. 241–255, doi:10.1016/j.epsl.2010.11.005.

Zurek, B.D., 2008, The evolution and modification of continental lithosphere, dynamics of 'indentor corners' and imaging the lithosphere across the eastern syntaxis of Tibet [Ph.D. thesis]: Bethlehem, Pennsylvania, Lehigh University, 258 p.

Manuscript Accepted by the Society 28 February 2014